UNIVERSITY OF CALIFORNIA

Los Angeles

Search for the Chiral Magnetic Effect

from RHIC Beam Energy Scan II data with STAR

A dissertation submitted in partial satisfaction

of the requirements for the degree

Doctor of Philosophy in Physics

by

Zhiwan Xu

2024

ABSTRACT OF THE DISSERTATION


Search for the Chiral Magnetic Effect

from RHIC Beam Energy Scan II data with STAR


by


Zhiwan Xu

Doctor of Philosophy in Physics

University of California, Los Angeles, 2024

Professor Huan Z. Huang, Chair

In high-energy heavy-ion collisions, the Chiral Magnetic Effect (CME) offers a unique window to probe several fundamental properties in quantum chromodynamics (QCD): topological vacuum transitions, chiral symmetry restoration at high temperature, and the properties of a new QCD phase, Quark Gluon Plasma (QGP). Furthermore, it simultaneously probes the strong magnetic field ($\vec{B}$) created by spectator protons in the colliding nuclei at almost the speed of light. The CME describes an electric charge separation of nearly massless quarks, which are at local chirality imbalance, along the $\vec{B}$ direction, manifestly violating local $\mathcal{P}$ and $\mathcal{CP}$ symmetries. This charge separation effect is quantified by the $\Delta\gamma^{112}$ correlator between pairs of final-state charged hadrons and the reaction planes of the collision. However, due to the complex dynamics of the expanding fireball, the major background in CME search comes from the elliptic flow ($v_2$) coupling with physics such as resonance decay, local charge conservation, and local momentum conservation. In order to mitigate the flow background in CME measurement, a novel event shape selection (ESS) approach is developed that manages to classify events based on their emission pattern shapes and determines $\Delta\gamma_{\mathrm{ESS}}^{112}$ at the zero-

flow limit. Furthermore, the spectator protons collected by STAR EPD detector are used to reconstruct the reaction plane correlated with $\vec{B}$ direction, while minimizing nonflow backgrounds. The search for the CME in the RHIC Beam Energy Scan phase II (BES-II) carries great scientific impact. It promises a thorough systematic investigation by the newly developed methods to mitigate all known backgrounds and by utilizing the stronger magnetic field provided by larger collision systems of Au+Au. With significantly higher data quality compared to BES-I and the successful development of a new ESS methodology, we observed a positive charge separation of $3\sigma$ significance in the 20%–50% centrality range of Au+Au collisions at each of the three center-of-mass energies, 11.5, 14.6, and 19.6 GeV. The findings and physics implications will be discussed.

The dissertation of Zhiwan Xu is approved.

Michail Bachtis

Michael Gutperle

Zhongbo Kang

Huan Z. Huang, Committee Chair

University of California, Los Angeles

2024

*To my family.*

TABLE OF CONTENTS

# LIST OF FIGURES

LIST OF TABLES

# ACKNOWLEDGMENTS

# VITA

2014 – 2018  Bachelor of Science in Physics,

Fudan University, Shanghai, China

2018 – 2021  Teaching Assistant,

Department of Physics and Astronomy,

University of California, Los Angeles

2021 – 2024  Graduate Student Researcher, Dissertation Year Fellowship,

Department of Physics and Astronomy,

University of California, Los Angeles

# CHAPTER 1

# Introduction

Quantum Chromodynamics (QCD) describes how the basic blocks of our world, quarks, are bound together by gluons in strong interactions. Gluons can also interact with each other due to their color charges, which may impart quarks with imbalanced chirality, or 'handedness'. This chirogenesis is analogous to baryogenesis in the early universe. The Relativistic Heavy-ion Collider (RHIC) at Brookhaven National Lab has recreated a state of matter of deconfined quarks and gluons, Quark Gluon Plasma (QGP), that once existed microseconds after the Big Bang. These collisions also generate a powerful magnetic field, facilitating the probe of chirogenesis via a novel phenomenon, the Chiral Magnetic Effect (CME). Thus, the discovery of the CME not only unveils fundamental aspects of QCD, but also deepens our understanding of the universe.

## 1.1 Quark Gluon Plasma

Quantum Chromodynamics (QCD), a non-Abelian quantum field theory that describes the strong interactions of quarks and the gauged boson gluons[1], was proposed half a century ago in 1973. It is the $SU(3)$ gauge theory[2][3] encompassed into the Standard Model, $SU(3)_c \times SU(2)_L \times U(1)_Y$, that includes the strong, electromagnetic and weak interactions (the latter two are unified in electroweak theory by [4][5],[6] and [7]). The $SU(3)$ group of QCD has eight generators, associated with eight conserved color charges. The QCD

Lagrangian density is often written as follows [8]:

$$\mathcal{L} = \bar{\psi}(i\slashed{D} - m)\psi - \frac{1}{4}(G^a_{\mu\nu})^2 + \frac{1}{2\xi}(\partial^\mu A^a_\mu)^2 + (\partial^\mu b^a)(D_\mu c)^a. \tag{1.1}$$

where $D_\mu = \partial_\mu - igA^a_\mu t^a$. Gluons sit in the octet adjoint representations of $SU(3)$[9], and the gluon fields, $G^a_{\mu\nu} = \partial_\mu A^a_\nu - \partial_\nu A^a_\mu + gf^{abc}A^a_\mu A^a_\nu$, transform as vectors under the Lorentz group, corresponding to carrying an intrinsic angular momentum, spin-1. Quarks ($\psi$) transform under the fundamental representations of $SU(3)$ [10][11] and antiquarks transform according to the complex conjugate representation, both are spin-1/2 particles. The quantization of the field introduces the latter two terms in QCD Lagrangian, the Faddeev-Popov gauge fixing term, and the ghost term from the Jacobian determinant, which are calculated from the Feynman path internal over the gauge field potential $A^a_\mu$.

The Standard Model consists of six flavors of quarks, and six flavors of leptons, where the flavor charge is interacted through the electroweak force. Three of the six quarks are considered light quarks, up ($u$), down ($d$), and strange ($s$), since their explicit masses from Higgs coupling are lighter than the QCD scale of $\Lambda_{QCD} \sim 200$ MeV. The other three are heavy quarks, charm ($c$), bottom ($b$), and top ($t$).

The most important aspects of QCD are asymptotic freedom[12][13] and confinement at vanishing temperature and finite chemical potential ($\mu_B$), which come from the quantization of the non-Abelian gauge theory. The beta function, $\beta(g) = \frac{\partial g}{\partial \log Q}$, represents the running of a coupling constant $g$, which is negative in QCD so that the coupling decreases logarithmically, also known as color anti-screening. The effective interaction length of the gluon gauge field can be quantified by the Deybe length $r_D$, at which the interaction strength is at maximum. Under perturbative calculation from the first principle, the $r_D$ is proportional to $1/T$ and $1/\mu_B$ (Eq. (2.3.10) and (2.3.16) of [14]). At vanishing $T$ and $\mu_B$, $r_D$ is infinite, which means the interaction will always increase at longer lengths, and quarks are confined to form hadrons. This is where the ordinary matter of our world sits. However, at high temperatures or at large $\mu_B$, the Deybe length becomes finite, so that beyond $r_D$ the gluon interactions decrease, also known as color screening. This predicts the possible new phase of

matter, Quark Gluon Plasma (QGP), where quarks become deconfined, and color charges are liberated.
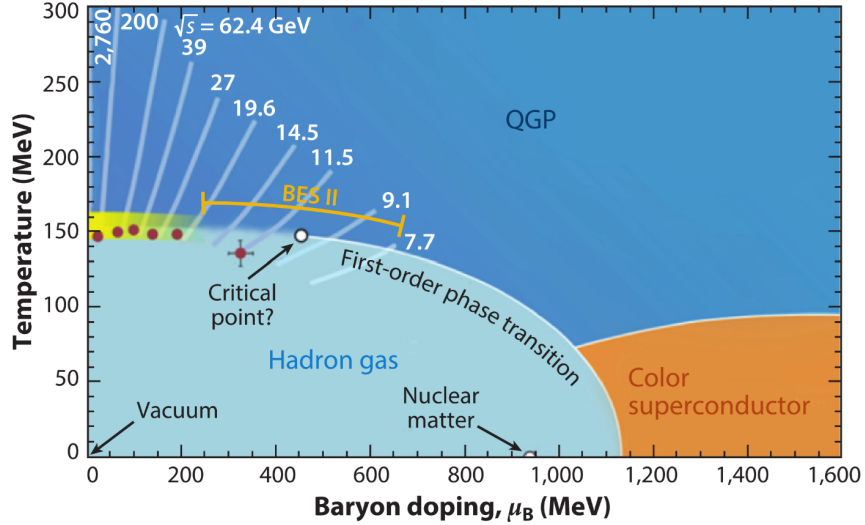


Figure 1.1: The QCD Phase Diagram calculated from the lattice QCD, adopted from [15]

The Quark Gluon Plasma, once existing at $10^{-6}$ $s$ after the Big Bang, can be created in high-energy experiments at extreme temperatures, as shown in the QCD phase diagram in Fig. 1.1. At vanishing $\mu_B$, the transition from hadronic matter to Quark Gluon Plasma is expected at a temperature higher than the crossover temperature, $T_{cross} \approx 150$ MeV from lattice QCD calculation[16]. The $\mu_B$ values, from small to large, correspond to the different heavy-ion experiments, including the Beam Energy Scan (BES) at the Relativistic Heavy Ion Collider (RHIC), and the transition is expected to happen when the energy density is higher than $\varepsilon_c \approx 0.3 - 0.4$ GeV/$c$ [17]. With liberated quarks and gluons, the QGP state embeds many aspects different from ordinary matter. Several experimental signatures of QGP were proposed for high-energy heavy-ion collisions as early as the 1980s and 1990s, such as strangeness enhancement, jet quenching, and sequential melting of quarkonia. (See [17] for review)

One aspect of QGP with deconfined quarks is the chiral symmetry restoration. The chiral symmetry is the fundamental symmetry of QCD Lagrangian with massless quarks.

However, it is broken in the vacuum (ground state) and the hadron state. The QCD vacuum is filled with quark–antiquark pairs, known as the quark condensate $\langle q\bar{q}\rangle$, or the chiral condensate, directly originating from the quantum effect at short distances. To keep Lorentz invariance, the $q\bar{q}$ pair has zero momentum and angular momentum, but it has a non-zero chiral charge. The existence of a quark anti-quark pair causes vacuum polarization. The nonzero vacuum expectation value (VEV) is $\langle \bar{q}_R^a q_L^b \rangle = -\delta^{ab}\sigma$, where $\sigma \sim \Lambda_{QCD}^3$, It brings the effective mass [18] of the quark field and breaks the chiral symmetry of the QCD vacuum.

At high temperatures, the quark condensate density $\langle q\bar{q}\rangle$ dissolves so that the ordering parameter that manifests the expectation value of the chiral condensate disappears. The formation of QGP brings in new degrees of freedom. As a consequence, the effective mass of the fermion component of the hadrons, which is mostly from gluon binding, disappears. Only the quark mass coupling to Higgs is left. The latter is very small compared with QGP temperature $T > 150$ MeV, particularly for light quarks. For example, the explicit masses of $u$ and $d$ quarks are $\sim 4$ MeV/$c^2$. Hence, at QGP temperature, the mass term in QCD Lagrangian density $\mathcal{L}_m = m\bar{\psi}\psi$ could be safely ignored, known as the chiral symmetry restoration (at least partially). Alternatively, such partial restoration of the chiral symmetry can also happen for the nuclear matter at high density, which was recently observed in pionic atoms [19]. This QCD chiral symmetry restoration is different from the electroweak chiral symmetry, which corresponds to the Higgs field interaction and is expected to happen at $10^{16}$ GeV of the grand unification theory scale.

Another aspect of the QGP is its superfluidity as the perfect liquid on Earth. It has the smallest shear viscosity to entropy density ($\eta/s$), currently estimated to be $\sim 0.1$ at critical temperature [20][21]. Therefore, the possible spatial anisotropy in the initial collision geometry can be shared by the quarks' collective motion, and later translated to final-state momentum anisotropy through the pressure gradient. The momentum anisotropy is known as collective flow, quantified by Fourier coefficients $v_n$, and the most prominent one of them is elliptic flow $v_2$. The observed universal scaling of $v_2(p_T)$ by the number of constituent

quarks (NCQ) [22] is considered to be key evidence of the creation of the QGP in relativistic heavy-ion collisions. Such a finding allows the viscous hydrodynamics calculation [23] to understand the rapid evolution of the QGP matter.

## 1.2 QCD vacuum topology

Quark Gluon Plasma offers a unique probe for the QCD vacuum. Due to its non-Abelian nature, the QCD vacuum has a non-trivial topology, which comes from the mapping of the compact 3D space to the sub-group $SU(2)$ of the $SU(3)_c$, $\mathbb{S}_3 \rightarrow SU(2)$. It is characterized by the winding number ($\in \mathbb{Z}$), also known as the Chern-Simons number ($N_{CS}$) [24]. The change of the winding number is the full spacetime integral of the gluon field by

$$\Delta N_{CS} = \int d^4x G^{\mu\nu}\widetilde{G}_{\mu\nu} = \int d^4x \partial_\mu K^\mu, \tag{1.2}$$

where $\widetilde{G}_{a\mu\nu} = \frac{1}{2}\epsilon_{\alpha\beta\mu\nu}G_a^{\alpha\beta}$, and $G^{\mu\nu}\widetilde{G}_{\mu\nu}$ can be written as a total derivative of Chern-Simons current $K^\mu$. By taking the integral over time dimension from $t = -\infty$ to $\infty$, the winding number is $N_{CS} = \int d^3x K^0$, given that the other term $\partial_i K^i$ integrated over the three space dimensions would be zero due to the compactness of $\mathbb{S}_3$. Thus the QCD vacuum has a degeneracy and can be considered as a set of vacua, each characterized by a different $N_{CS}$ number.
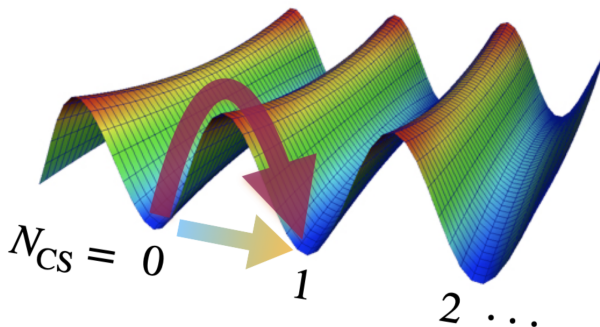


Figure 1.2: The vacuum structure of the QCD is non-trivial. Different topological sectors are separated by $N_{CS}$.

The classical solution of the Eular-Lagrangian equation in Euclidean spacetime with finite action is known as the instanton solution[24], which is associated with an integer winding number. When transferring from Euclidien to Minkovski spacetime, the instanton often refers to the quantum tunneling effect between different valleys, causing a change of the winding number. At non-integer winding numbers, the semi-classical calculation with static fields gives another solution at the saddle point of the potential (by minimizing the potential with fixed $N_{CS}$), associated with half integers, known as sphaleron ($N_{CS} = \pm 1/2, \pm 3/2$ ...). The periodic shape for QCD vacuum is shown in Fig. 1.2, where the barrier height reflects the potential, the tunneling is referred to as instanton, and the crossing over the saddle point represents the sphaleron crossover. Its longitudinal dimension represents the field configuration space.

The QCD vacuum can be seen as the interference of the vacuum states, $\Sigma_n e^{in\theta_{QCD}}|n\rangle$, where $|n\rangle$ is a degenerate state distinguished by a quantum number of $N_{CS}$, and $\theta_{QCD}$ is the phase experimentally restricted by the upper limit $\theta < 3 \times 10^{-10}$ [25]. The phase $\theta$ of our vacuum is influenced by both strong ($\theta_{QCD}$) and electroweak ($\theta_{EW}$) interactions, and the latter is related to the diagonalization of the quark mass matrix. In the following discussion, we will omit the subscript QCD and use $\theta$ to refer to the "$\theta_{QCD}$". Therefore, it is equivalent to introducing an additional term to the QCD Lagrangian,

$$\mathcal{L}_\theta = -\frac{\theta}{32\pi^2} g^2 G_a^{\mu\nu} \widetilde{G}_{\mu\nu a}, \tag{1.3}$$

so that the vacuum can be directly considered as $\Sigma_n |n\rangle$. If $\theta$ is non-zero, this corresponds to the strong $\mathcal{CP}$ violation. In Maxwell-Chern-Simons theory [26], $\theta$ is treated as a pseudo-scalar field $\theta(x, t)$, known as the axion field, so that this additional QCD term can be associated with an effective QED term in Lagrangian.

The QCD vacuum transition may lead to the chirality change of quarks. Due to the axial anomaly in the quantization of QCD Lagrangian, the chiral current ($J_{\mu 5} = \bar{\psi}\gamma_\mu\gamma_5\psi$) is not

conserved, $\partial^\mu J_{\mu 5} \neq 0$, even for massless quarks, which is calculated as

$$\partial^\mu J_{\mu 5} = 2mi\bar{\psi}\gamma_5\psi - \frac{N_f g^2}{16\pi^2}G_a^{\mu\nu}\widetilde{G}_{\mu\nu a}. \tag{1.4}$$

The second term can be written as a total derivative of Chern-Simons current $\partial_\mu K^\mu$. The chiral charge $(Q_5)$ is defined as $Q_5 = \int d^3x J_5^0$, thus, following similar integration above, the change of $N_{CS}$ in QCD vacuum can lead to a change of the chiral charge $Q_5$ [27]. This manifests that topological fluctuation from the gluon field can be transferred to the axial chiral current via chiral anomaly.
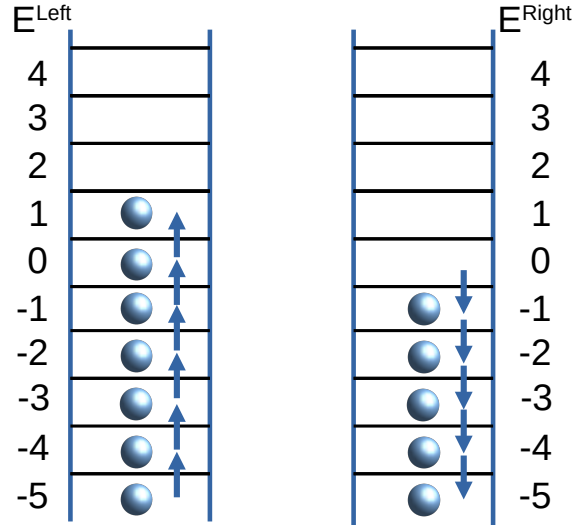


Figure 1.3: Dirac sea of the left and right quarks in the presence of a chiral charge $Q_5$ changing inside a small domain.

Figure 1.3 illustrates such translation for left and right-handed quarks in the Dirac sea. When $\Delta N_{CS}$ is adiabatically changed from zero to one, as shown in this cartoon, it gradually moves all the left-handed particles up, increasing its Dirac sea level $\mu_L$ as seen from a macroscopic view. Meanwhile, all the right-handed particles are moved down, therefore lowering its sea level $\mu_R$. At negative infinite energy, left-handed particles are generated, and right-handed particles disappear without violating the energy loss. This renormalization

7

scheme keeps the total number of particles $(L + R)$ the same, while changing the $(L - R)$ particle number. Hence, a finite chiral chemical potential, $\mu_5 = \mu_R - \mu_L$, is created in a local domain. It is equivalent to creating a left-handed quark-anti-quark pair at the same time. (Recall anti-quark with right-handed chirality has left-handed helicity.) This mechanism can also generate chiral condensate $q\bar{q}$ in QCD vacuum.

The QCD vacuum has a similar topological structure as the electroweak vacuum, from the non-Abelian nature of $SU(2)_L$ gauge field. However, the potential barrier of the latter is thousands of times higher. Coupled with the electroweak gauge field, the Higgs field acquires a vacuum expectation value $v \sim 246$ GeV, much higher than the VEV of QCD, under spontaneous symmetry breaking. From the scale introduced by the Higgs field, the electroweak sphaleron energy is estimated to be approximately 9 TeV. From G. t'Hooft [28][29], the non-zero $\Delta N_{CS}$ value is associated with the change of the vacuum state and a change of the left-handed baryon number $B$ and the lepton number $L$ [30]. Since the $SU(2)_L$ doesn't couple to the right-handed particles, this corresponds to a change in the total number of $B + L$. Therefore, possible quantum tunneling and sphaleron crossover between vacuum sectors could cause the non-conservation of $(B + L)$, which is partially associated with the matter-antimatter asymmetry in the early universe at baryogenesis[31].

Similarly to baryogenesis, the QCD vacuum fluctuation could stimulate the "chirogenesis". At high temperatures, the excitation of gluons allows possible cross over the barrier by sphaleron, leading to the change of chiral charge of quarks in a local domain. In addition to the sphaleron transitions, the topological charge could also be introduced in the initial state [32], known as glasma [33]. The out-of-equilibrium system spontaneously breaks the boost invariance [34] so that the longitudinal glasma tube is formed, with both color $E$ and color $B$ field along the same $z$ direction. This may induce topological charge fluctuation in the pre-equilibrium stage. Theoretical calculation suggests that the QGP could maintain its finite chirality for a considerable time. Thus, experimentally it offers a probe to the vacuum topology structures. In contrast, the electroweak vacuum barrier is too high to be observable

in the current experiment scale. The transfer from chirality imbalance ($\mu_5 \neq 0$) to Maxwell observables will introduce the Chiral Magnetic Effect (CME).

## 1.3  Chiral Magnetic Effect

The Chiral Magnetic Effect (CME) describes the charge separation of fermions (quarks) with chiral imbalance along the external magnetic field [32][26]:

$$\vec{J} = \frac{e^2}{2\pi^2}\mu_5\vec{B}. \tag{1.5}$$

The CME equation for quarks can be derived from the Maxwell-Chern-Simons theory [26] and many other approaches such as the hydrodynamic approaches, energy balance argument, thermodynamic potentials (see discussions in [32]). In Maxwell-Chern-Simons calculation, the QCD $\theta$ coupling to the gluon field $G_a^{\mu\nu}\widetilde{G}_{\mu\nu a}$ would introduce an effective Lagrangian term of QED through axial anomoly, as $\theta$ coupling to the Maxwell $F_a^{\mu\nu}\widetilde{F}_{\mu\nu a}$ [26]. The Euler-Lagrangian equation for the gauge potential would lead to a current proportional to the size of chiral imbalance and magnetic field $\vec{J} \propto \mu_5\vec{B}$, and by comparing the energy balance the coefficients is settled to be $\frac{e^2}{2\pi}$.

As shown in Fig. 1.4, for massless quarks (Dirac fermions), the helicity and chirality eigenstates coincide. A left-handed quark ($\psi_L$) has left helicity and left chirality. Thus its spin and momentum have opposite directions to each other. A right-handed quark ($\psi_R$) has its spin and momentum aligned with each other. Though not included in the cartoon, the anti-particles would be different. For instance, a left-handed antiquark would have right-handed helicity and left-handed chirality. Particularly, a $\bar{u}_L$ would look like a $d_R$ in the cartoon, regardless of their charge difference. For simplicity, anti-particles are not included in this illustration.

When applying an external magnetic field, the spin of positively charged particles tends to align with the magnetic field, such as $u$ quarks, to minimize the energy. The spin for negatively charged particles tends to be anti-aligned with the $B$ field, such as $d$ quarks.

9
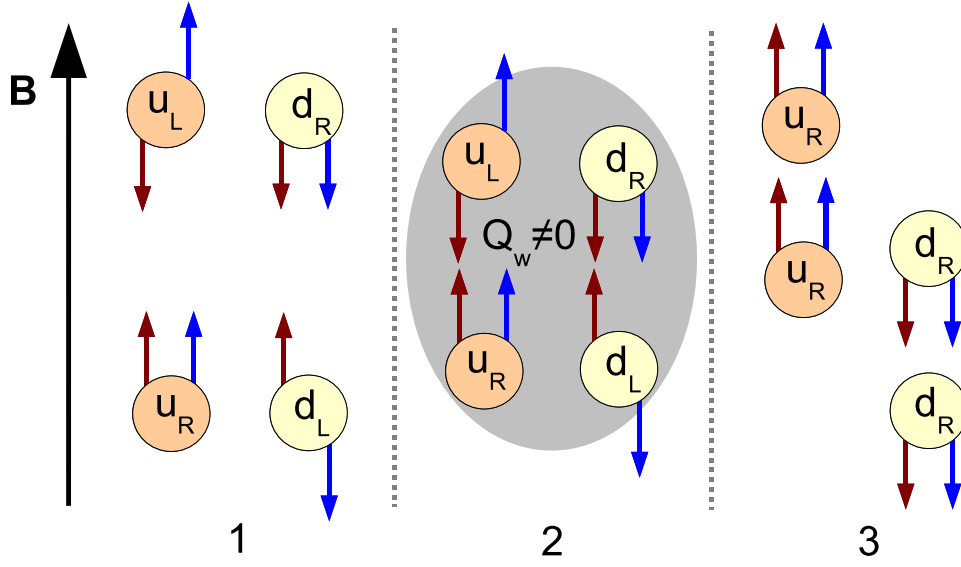
Figure 1.4: The chiral magnetic effect for quarks, with red arrow resembling momentum ($p$) and blue arrow the spin ($s$), cited from [35].

When there is a chirality balance for positive (negative) quarks, the currents of left- and right-handed particles are canceled. However, when thermal fluctuation induces a non-zero chirality potential ($\mu_5 \neq 0$), for instance, the system has $\Delta N_{CS} = -1$, a left-handed particle will be replaced with a right-handed particle, and then a net current from chirality imbalance was observed. Since $d$ and $u$ quarks go to opposite directions, this results in a charge separation along the $B$ field.

The chirality chemical potential $\mu_5$, different from the normal chemical potential, is not a conserved quantity. The existence of non-zero chirality chemical potential in a local domain spontaneously breaks the $\mathcal{P}$ and $\mathcal{CP}$ symmetries. In heavy-ion collisions, after the QCD vacuum topology fluctuation introduces the non-zero $\mu_5$ (considered as a local constant), and considering the electric current $\vec{J}$ is parity odd while the magnetic field $\vec{B}$ is parity even, the equation of the CME (Eq. 1.5) violates local symmetry in $\mathcal{P}$ and $\mathcal{CP}$ translation.

The current generated from chiral anomaly ($\mu_5 \neq 0$) had a big impact in many physics fields. In Table.1.1, we list the comparison of such phenomena in electroweak, high-energy

Table 1.1: Table for current induced by chiral anomaly in different fields of physics, partially cite from [36].

| | Electroweak | High energy QCD | condensed matter |
|---|---|---|---|
| System | The Universe | Quark-Gluon Plasma | Dirac/Weyl semimetals |
| Chirality imbalance source | Topological transitions in hot electroweak vacuum: sphalerons | Topological transitions in hot QCD vacuum: sphalerons | External parallel electric and magnetic field $\vec{E} \cdot \vec{B}$ |
| Carrier | quarks | quarks | Electronic quasiparticles |
| Charge separation / Current | Baryon | Electric | Electric |
| Signature | Baryon asymmetry of our universe, baryogenesis | Azimuthal charge separation in heavy-ion collisions, chirogenesis | Negative magnetoresistance |

QCD, and condensed matter.

The CME phenomenon has been experimentally discovered in condensed-matter experiments in a number of Dirac [37][38] and Weyl [39] semimetals, with $\mu_5$ and $\vec{B}$ precisely controlled. The Weyl point close to the Fermi level allows for distinct chirality (left or right-handed) of quasi-electrons. The Dirac point is when two Weyl points with opposite chirality meet in momentum space and allow both left and right-handed quasiparticles with additional 3D symmetry. In the presence of the parallel magnetic and electric fields, $\vec{E} \cdot \vec{B}$, the chiral anomaly in QED leads to the non-conservation of the particle number with a certain chirality at Weyl point. In the Dirac semimetals, the $\vec{E} \cdot \vec{B}$ pumps the electrons between the Weyl

point with opposite chirality, and creates the chirality imbalance. Therefore, under a parallel magnetic field, fermions would exhibit the CME to cause a negative magnetoresistance. This $U(1)$ chiral anomaly has been experimentally confirmed, with a vast scale research ongoing towards the applications in quantum computing and communication.

The observation of the CME in condensed matter encourages the intense search for the CME in heavy-ion collisions, which would potentially mark the first direct experimental observation of the topological vacuum transition. It offers a unique probe into the nontrivial topology of the vacuum, essential to non-Abelian gauge theory to both QCD and electroweak physics. Although topologically similar, the electroweak vacuum has a much higher energy barrier that prevents current experiments from probing its transitions (believed to be the origin of baryogenesis). Studying the CME in QCD through heavy-ion collisions thus can enhance our understanding of both QCD and the Universe. In addition, it gives rise to the search of other anomaly-induced phenomena such as the chiral vortical effect [40], the chiral magnetic wave [41], which are also closely related to the fluid dynamics of the black hole.

## 1.4 CME in Heavy-Ion Collision
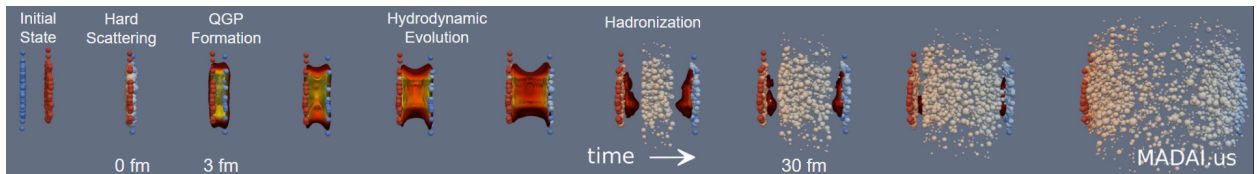


Figure 1.5: The evolution of a Au+Au heavy-ion collisions

In a typical heavy-ion collision, the two ions are accelerated to nearly the speed of light, with a longitudinal Lorentz contraction making the thickness close to 1 fm/$c$, as shown in Fig. 1.5. The pre-equilibrium fireball created at the center of collision is transient, and it soon forms the QGP matter at the initial time roughly estimated to be a few tenths of 1 fm, according to nuclear passage times [17]. After the QGP expands hydrodynamically and cools down fast, the quarks are frozen out first chemically, then kinetically, into the hadrons, and

12

experience spontaneous chiral symmetry breaking. At the Relativistic Heavy-Ion Collider (RHIC) and Large Hadron Collider (LHC), such "Small Bangs" take place a few times per second during the experiment running, which is analogous to the Big Bang that happened in our early Universe.

The Chiral Magnetic Effect in heavy-ion collisions requires three physical conditions to occur simultaneously:

- Chiral symmetry restoration in QGP,

- Vacuum topological transition ($\Delta N_{CS}$),

- A strong magnetic field ($\vec{B}$).

In the previous sections, we reviewed the creation of QGP above the critical energy density, which can be achieved at RHIC and LHC, and chiral symmetry is restored to give rise to massless quarks with a distinct chirality. The hot-QCD matter allows possible vacuum transition from the thermal fluctuation (sphaleron) by gluon excitation in the local domain. The strong magnetic field on the order of $10^{14}$ T is expected from the spectator protons accelerated to almost the speed of light. Therefore, all three conditions are potentially satisfied in the QGP matter in the heavy-ion collisions. However, the simultaneous occurrence of them in a complex relativistic dynamic system is still an open question. Thus, it stimulates experimental searches in a broad range of collision systems and beam energies.

The crucial condition is the fast decaying magnetic field, which is difficult to detect or compute due to the medium effect of QGP. In the vacuum, the peak $B$ field is estimated to be $|eB| \sim \frac{\alpha}{R^2} Zb\gamma \sim m_\pi^2$ at the center of the impact parameter, which decays faster at higher collision energies (in Fig. 1.6(a)). In the QGP matter with a finite conductivity, estimated to be $\sigma_{LQCD} \sim 5.8$ MeV [43], the enhancement of a decaying magnetic field is expected as in Fig. 1.6(b) from in-medium Maxwell's equation calculation [42]. However, since both the QGP initial time and its lifetime are unknown, and are extremely difficult to detect,
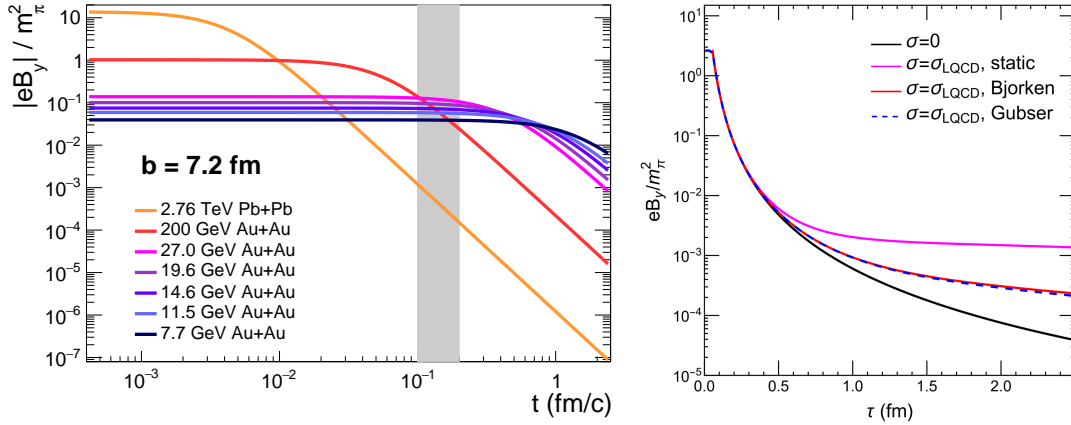
Figure 1.6: (a)The magnetic field in vacuum decays faster at higher energy, where the grey band represents the possible QGP presence. (b) The QGP electric conductivity can sustain the $B$ field in Au+Au at 200 GeV [42].

the integrated $B$ field over the QGP lifetime could not be computed directly. Potentially, it could be enhanced by the longer nuclear passage times at lower energies. Recent STAR data unveiled the magnetic field's imprint on the QGP, with the effect in Au+Au collisions approximately 10 times stronger at the lower energy of 27 GeV than at 200 GeV [44]. This beam-energy dependence heralds an enhanced opportunity to detect the CME during the RHIC Beam Energy Scan (BES). Moreover, the absence of deconfinement and chiral symmetry restoration at sufficiently low beam energy is crucial to the search as it provides valuable data where the CME signature is expected to be absent.

The CME in heavy-ion is illustrated in Fig. 1.7. The spectator protons create a magnetic field perpendicular to the reaction plane. In metastable domains with nonzero $\mu_5$, the CME could prompt an electric charge separation of light quarks along the external magnetic field, $\vec{J} = N_c \Sigma_f (Q_f^2 \frac{e^2}{2\pi^2} \mu_5 \vec{B})$, summing over the colors and flavors. It leads to a specific hadronic emission pattern, asymmetric to the reaction plane ($x$-$z$ plane).

To quantify the CME-induced charge separation and other collective modes, the Fourier expansion is applied to the azimuthal angle ($\varphi$) distribution of final-state charged particles
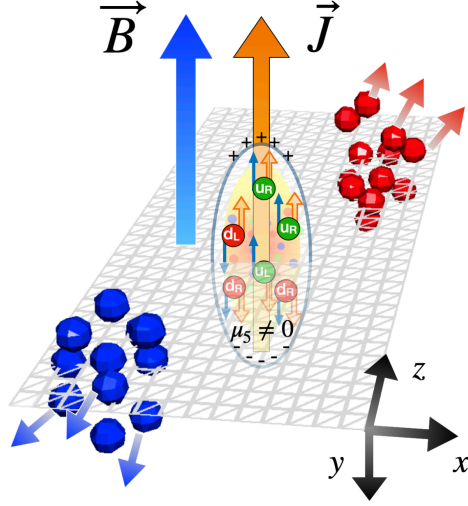
Figure 1.7: Illustration of the CME in heavy-ion collisions.

with respect to the reaction plane $(\Psi_{\mathrm{RP}})$ [45],

$$\frac{dN_{\pm}}{d\varphi} \propto 1 + \sum_{n=1}^{\infty} 2a_n^{\pm} \sin n\Delta\varphi + \sum_{n=1}^{\infty} 2v_n^{\pm} \cos n\Delta\varphi, \tag{1.6}$$

where $\Delta\varphi = \varphi - \Psi_{\mathrm{RP}}$.

Due to the dilution effect, the $a_1^+$ and $a_1^-$ is on the order of one over multiplicity $1/N$, and bear opposite signs due to the charge separation [46]. The hydrodynamic expansion converts the initial overlap geometry into the momentum anisotropy $(v_n)$ of final-state particles[47]. Since the parity is locally violated but globally conserved in QCD, the CME observable targets to measure the fluctuation of $a_1$, which is $\sim 10^{-4}$. Our recent study [48] affirms the similarity in the key components of different CME observables, including the $\gamma^{112}$ correlator [46], the $R_{\Psi_2}(\Delta S)$ correlator [49], and the signed balance functions [50].

In this work, we focus on the most widely used [46]

$$\gamma^{112} \equiv \langle \cos(\varphi_\alpha + \varphi_\beta - 2\Psi_{\mathrm{RP}}) \rangle, \tag{1.7}$$

where $\alpha$ and $\beta$ represent charge sign. The average is taken over particle pairs and then over events. Experiments typically report $\Delta\gamma^{112} \equiv \gamma_{\mathrm{OS}}^{112} - \gamma_{\mathrm{SS}}^{112}$, which cancels the common
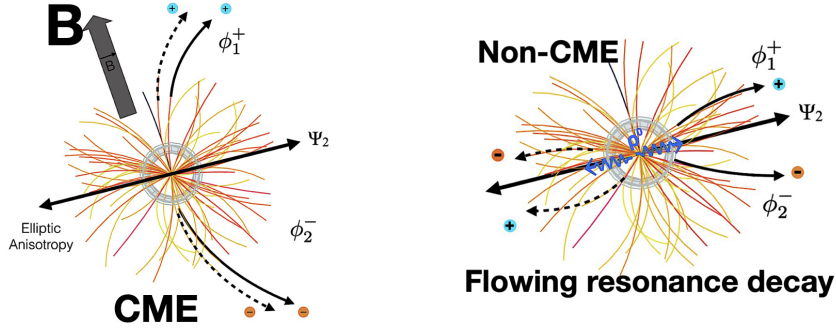
Figure 1.8: Charge separation caused by CME and background physics in heavy-ion collisions.

background for opposite-sign (OS) and same-sign (SS) pairs. Positive $\Delta\gamma^{112}$ values have been observed in Au+Au collisions at the top RHIC energy [51][52][53] and in Pb+Pb at the LHC [54]. However, the data interpretation is impeded by the background physics.

The major background in the CME measurement comes from elliptic flow ($v_2$) coupled with other mechanisms such as resonance decays [46], local charge conservation (LCC) [55][56], and transverse momentum conservation (TMC) [57]. Figure 1.8 compares the CME charge separation and the background charge separation. From recent understanding, the flow background contributes to at least 80–90% in the CME observables at RHIC top energies. At LHC energy, the charge separation seems to be dominated by the background. The CMS experiment reports the same $\Delta\gamma^{112}$ in Pb+Pb and the pure-background system of $p$+Pb at the same multiplicities at $\sqrt{s_{NN}} = 5.02$ TeV [58][59]. At lower energies of RHIC BES-I, STAR introduced $H(\kappa_{bg}) \equiv (\kappa_{bg}v_2\delta - \gamma^{112})/(1+\kappa_{bg}v_2)$ [60], where $\kappa_{bg}$ is a free parameter, and $\delta \equiv \langle\cos(\varphi_\alpha - \varphi_\beta)\rangle$ represents the two-particle correlation coupling to the flow background. With $\kappa_{bg} \approx 2$, the difference $\Delta H \equiv H_{SS} - H_{OS}$ tends to vanish in the 0–60% centrality region of Au+Au collisions at $\sqrt{s_{NN}} = 7.7$ and 200 GeV, and remains positively finite at beam energies in between [60]. This rise-and-fall trend is enticing, but the $\kappa_{bg}$ value is unknown a priori. A detailed examination of the origin of the resonance flowing background will be covered in Sec. 3.1.

Additionally, nonflow correlations [45], unrelated to the RP, could also contribute to $\Delta\gamma^{112}$ from various sources including clusters, resonances, jets, and dijets, among others. Nonflow effects are more pronounced in smaller systems with lower multiplicities, like $p(d)$+Au collisions at $\sqrt{s_{NN}} = 200$ GeV [61]. This effect can be largely suppressed by using the information of spectator protons to construct the $B$ field direction, as spectators leave the system earlier.

A decade's effort has been focused on the attempt to suppress the background in the CME observables. One strategy is to search for the signal difference in two analogous systems or measurements. The RHIC isobar program, one of the DOE high-profile project, targets the systems of $^{96}_{44}$Ru+$^{96}_{44}$Ru and $^{96}_{40}$Zr+$^{96}_{40}$Zr. They are presumed to exhibit distinct CME signals but similar backgrounds [62][63][64]. The details of our work will be discussed in (Sec. 3.4). Our finding is that the STAR isobar data at 200 GeV manifest no predefined CME signatures [65][66], and the background fraction in such small collision systems is much higher than the anticipated 86%. A similar idea includes the comparison of CME fraction in $\Delta\gamma^{112}$ ($f_{\text{CME}}$) by contrasting the observables measured with respect to two types of event planes, the participant and spectator planes [67][68]. However, the $f_{\text{CME}}$ values determined by STAR is consistent with zero at 200 GeV, and dominated by statistical errors at 27 GeV [69][70]. Another study is to check two separate classes of pair invariant mass [71], while the corresponding STAR data at 200 GeV [72] did not see the CME signature. In Sec. 3.1, we will also show that the invariant mass spectrum is significantly impacted by the existence of CME.

A more realistic strategy is to look at the emission pattern to directly suppress the $v_2$-related background. In early times, to control the eccentricity, Event Shape Engineering was proposed (ESE) [73] to classify events based on the event shape and extrapolate $\Delta\gamma^{112}$ linearly to isotropic events with zero $v_2$. The corresponding results reveal no CME signals at the top RHIC energy [74] and the LHC energies [75][76][59]. The main difficulty comes from the long extrapolation of $\Delta\gamma^{112}$ over a wide, unmeasured $v_{2,\text{POI}}$ region because categorizing

the events excludes particles of interest (POI). This introduces substantial statistical and systematic uncertainties [77].

Instead, direct usage of the POI emission pattern is preferred, as it takes into account the emission pattern affected by both eccentricity and fluctuation, which better presents the CME background. However, it is more challenging and requires a thourough examination. Our work was mainly dedicated to the successful development of a new event-shape approach that utilizes POI emission pattern directly. The Event Shape Selection (ESS) [77] aiming for the CME measurement will be discussed in Sec. 3.5. The application to data analyses for the RHIC Beam Energy Scan II is in Chpt. 4. The physics implications on the CME in heavy-ion collisions and the outlook will be discussed in Chpt. 6.

# CHAPTER 2

# RHIC and STAR Experiment

Since its launch in 2000, the Relativistic Heavy Ion Collider (RHIC) at Brookhaven National Laboratory has facilitated advanced nuclear research by accelerating light to heavy nuclei to near-light speeds to produce Quark-Gluon Plasma (QGP), mimicking early universe conditions. With a 3.834 km tunnel, RHIC reaches up to 100 GeV/n beam energy for heavy ions like gold, achieving peak luminosities of $7 \times 10^{32}$ cm$^{-2}$s$^{-1}$ hitherto. The collider's versatility allows frequent shifts in collision species and energies, enhancing the Beam Energy Scan (BES) program's exploration of various QGP states. Quarks and gluons from these collisions form stable particles such as baryons and mesons, detected by the Solenoidal Tracker at RHIC (STAR), contributing to significant findings across multiple experiments.

## 2.1 Relativistic Heavy Ion Collider

The Relativistic Heavy Ion Collider (RHIC) at Brookhaven National Laboratory has supported five major experiments: STAR, PHENIX, PHOBOS, BRAHMS, and PP2PP, since it commenced operations in 2000. RHIC is designed to deliver beam energies up to 100 GeV/n for the heaviest ions, such as gold (Au), with a peak luminosity ($2 \times 10^{26}$ cm$^{-2}$s$^{-1}$ designed) achieved at $5 \times 10^{32}$ cm$^{-2}$s$^{-1}$ at its six interaction points [78]. Currently, two active experiments, the STAR and the sPHENIX (formerly PHENIX) are under RHIC physics run. Its heavy ion operations encompass greater flexibility than other hadron colliders, frequently adjusting species and collision energies, which has led to numerous significant discoveries.

### 2.1.1  The Complex of RHIC
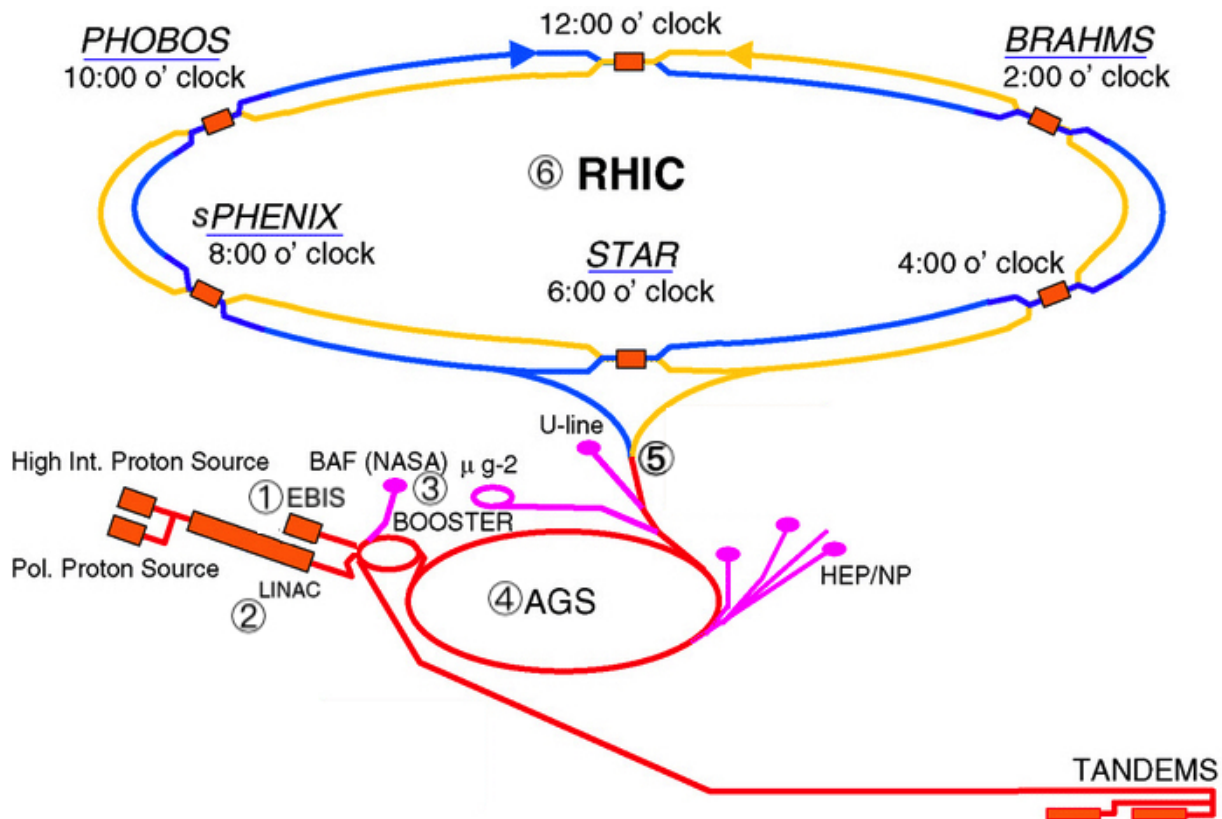


Figure 2.1: RHIC complex map [79]

RHIC is a complex composition of accelerators, interconnected by beam transfer lines to underscore its complex function, shown in Fig. 2.1. The heavy ions begin at the Electron Beam Ion Source (EBIS) accelerator ①. Protons for other experiments are accelerated and supplied at the Linear Accelerator (Linac) ②. Following the initial acceleration, the ions proceed to the compact Booster Synchrotron ③, where their energy is progressively increased with each orbit. Subsequently, the ions enter the Alternating Gradient Synchrotron (AGS) ④, which channels them via a beamline ⑤ into RHIC's dual tunnels. Within the RHIC rings ⑥, radio waves provide a final boost in energy, allowing the ions to circulate for hours.

EBIS was designed to provide energetic ion sources for a variety range of ions from polarized $He_3^{2+}$ to multi-charged ions up to $U_{238}^{38+}$, utilizing external primary ion sources [80].

20

It was developed to replace the Tandem van de Graaff accelerators and has achieved significantly enhanced performance. The EBIS beam is transported through the ETB line to the end of TTB section 29 and injected via the C3 electrostatic inflector. It supports drift tubes operating at voltages above 20 kV and maintains high vacuum standards ($P < 1 \times 10^{-9}$ Torr) in the ionization region. The EBIS electron gun includes a spherical convex cathode within a magnetic field, improving electron emission uniformity and increasing perveance by narrowing the cathode-anode gap. The ion extractor is positioned close to the entrance aperture of the electron collector. The ion optics system integrates a high-voltage accelerating ion lens, adaptor-deflector, accelerating tube, gridded lens, a magnetic solenoid lens, thereby providing initial pre-acceleration of ions to 17 keV/nucleon for the Radio Frequency Quadrupole (RFQ) to ensure precise ion injection. The system is capable of switching any ion optical element in less than 1 ms, which is optimal given that the minimum ionization time is about 8 ms. The gold nuclei leaving the EBIS have a uniform kinetic energy of 2 MeV per nucleon and have an electric charge Q = +32.

The Tandem van de Graaff [81] was the primary ion source for RHIC prior to the EBIS. It is occasionally used during some RHIC runs when EBIS undergoes upgrades. For instance, the Tandem provided Au source in Run-20 of Au+Au at 11.5 GeV of BES-II [82] up to $1.9 \times 10^9$ ions per bunch and four bunches per AGS cycle. Inside the Tandem, electrons are stripped off from ions to reach the desired charge state. The ion beam is transmitted to the Booster through the TTB transport line. For gold beams, the ions exit the Tandem at the kinetic energy of 1 MeV/n and with Q = +12 charge state. Though this configuration provides a high intensity, it does not bear the flexibility and versatility of EBIS.

The Booster synchrotron [83], completed in April 1991 with a 200 m circumference, then accelerates ions to 100 MeV per nucleon. This process involves a single RF system operating on the 6th harmonic of the revolution frequency, which can ramp the magnetic field to 0.65 T in less than 100 ms, providing the necessary accelerating voltage [78]. The ions are organized in both horizontal and vertical betatron spaces by adding linear coupling to the

Booster lattice, which facilitates the formation of six bunches with kinetic energies of 100 MeV/n at extraction. These ions are then further stripped to a charge state of $Q = +77$ using a foil in the Booster-to-AGS (BtA) transfer line, removing all but the K-shell electrons, before being injected into the AGS. The Booster supports bunch merging to enhance the intensities of bunches injected into the AGS, with each cycle from injection to extraction taking 100-250 ms, and allows for multiple cycles per AGS cycle.

The Ion then enters the Alternating Gradient Synchrotron (AGS) [84], commissioned in 1960 and historically one of the world's premier particle accelerators with an 800 m circumference. The AGS employs a technique called alternating gradient focusing, which uses the field gradients of its 240 magnets alternated inward and outward to focus particles simultaneously in both horizontal and vertical planes. Ion beams are accelerated from 100 MeV up to 10 GeV per nucleon. Most ions are fully stripped by the time they exit, while gold ions are at $Q = 77+$. The operational cycle varies from 4 seconds for protons to 6.8 seconds for gold, with each cycle accommodating 2-4 for heavy ions. The Booster facilitates multiple cycles to fill the AGS circumference within 600 ms of the AGS repetition period, during which the bunches are aligned into AGS RF buckets (h = 12) [78]. After the fourth transfer, the beam is debunched, and then merge bunches via 4-to-1 or 3-to-1 bunches [78]. The intensity limit in the AGS was increased from $8 \times 10^9$ to $9.6 \times 10^9$ ions per cycle (4 bunches) in BES-II.

The gold ion will be further stripped to $Q = 79+$ in the AGS to RHIC (AtR) transfer line [85], online in 1995. AtR extending over 770 m are segmented into four regions: U Line, W Line, and the X-Line (for Blue beam), which includes six tunable quadrupole, half-cell post-Lambertson magnet, four vertical kicker magnets to direct the injected bunch, and the Y-Line (for Yellow beam). The final kinetic energies can be achieved up to 8.9 GeV/n for heavy ions, corresponding to a peak AGS magnetic rigidity of 80 Tm. The AtR transfer line employed conventional room temperature magnets from the former CBA project and utilized a magnetic septum and fast kicker system to vertically align the beam with the injection

orbit. The system can fill both rings with ions in about 1 minute [78].

Finally, the ions enter the RHIC collider with 111 filled bunches per ring, leaving 9 for abort gaps, and achieve typical ion densities of $2 \times 10^9$ per bunch. The bunch separation within the ring is 108 ns, correlating with a rise time of 95 ns. The injected beams, entering at 300 kV for gold and other heavy ions, are finely tuned through an adiabatic adjustment of the RF voltage to optimize acceleration and transition energy crossing. Upon reaching the operating kinetic energy, ion bunches transition from the 28.15 MHz acceleration to the 197 MHz storage with main RF cavities. In BES-II, double RF systems are upgraded. A second 9 MHz cavities were engaged in addition to the 28 MHz main RF cavities to increase bucket acceptance from 0.34 to 0.45 ev*s [82]. All ion species are required to shorten the bunch duration. The stored beam can be safely aborted onto an internal dump block within 13 $\mu$s via the abort kicker at the end of the storage cycle. In 2020, the LEReC electron cooling was operational for luminosity improvement in several BES-II low energies.

RHIC's ring magnets, essential for bending and focusing the ion beams, utilize low-field superconducting magnets to optimize costs given the fixed tunnel circumference. These include 288 arc-size and 108 insertion dipoles, alongside 276 arc and 216 insertion quadrupoles, supplemented by additional smaller magnets to refine beam control. The entire magnet complex is maintained below 4.6 K with supercritical helium circulated by a 24.8 kW refrigerator, ensuring a vacuum tighter than $10^{-11}$ Torr in the beam tube to mitigate electron cloud formation and maximize beam stability. The cryostats housing the superconducting magnets maintain an insulating vacuum below $10^{-5}$ Torr to prevent heat load from convection, illustrating RHIC's intricate balance of high-energy physics and engineering precision [78].

### 2.1.2 Beam Energy Scan Phase II

The RHIC Beam Energy Scan (BES) Phase II program was operated in 2018-2021, focusing on Au+Au collisions, to explore the QCD phase diagram with precision measurements of the intermediate-to-high $\mu_B$ region, as in the 2015 long-range plan [86]. The performance

parameters of RHIC in BES-II Au+Au collisions and comparing isobar collisions are summarized in Table. 2.1. The BES-II physics program requires a factor of 4 improvement of the luminosity compared to the BES-I and many RHIC upgrades are integrated during the time.

Table 2.1: Run performance of RHIC for Beam Energy Scan-II [87].

| Run | Species | $\sqrt{s_{NN}}$ | no of bunches | ions/bunch $[10^9]$ | calendar time in physics | total delivered luminosity |
|---|---|---|---|---|---|---|
| Run-18 | $^{96}_{40}$Zr+$^{96}_{40}$Zr | 200 | 111 | 1.0 | 28.5 days | 3.9 $nb^{-1}$ |
| Run-18 | $^{96}_{44}$Ru+$^{96}_{44}$Ru | 200 | 111 | 1.0 | 28.5 days | 4 $nb^{-1}$ |
| Run-18 | $^{197}_{79}$Au+$^{197}_{79}$Au | 27 | 111 | 2.0 | 24 days | 282 $\mu b^{-1}$ |
| Run-19 | $^{197}_{79}$Au+$^{197}_{79}$Au | 19.6 | 111 | 1.85 | 36 days | 151 $\mu b^{-1}$ |
| Run-19 | $^{197}_{79}$Au+$^{197}_{79}$Au | 14.6 | 111 | 1.75 | 60 days | 132 $\mu b^{-1}$ |
| Run-20 | $^{197}_{79}$Au+$^{197}_{79}$Au | 11.5 | 111 | 1.7 | 62 days | 143 $\mu b^{-1}$ |
| Run-20 | $^{197}_{79}$Au+$^{197}_{79}$Au | 9.2 | 111 | 1.1 | 117 days | 176 $\mu b^{-1}$ |
| Run-21 | $^{197}_{79}$Au+$^{197}_{79}$Au | 7.7 | 111 | 1.4 | 12.1 weeks | 152 $\mu b^{-1}$ |
| Run-21 | $^{197}_{79}$Au+$^{197}_{79}$Au | 17.3 | 111 | 1.9 | 11 days | 83 $\mu b^{-1}$ |

## 2.2   The STAR Detector

At RHIC, a warm space of $\pm 9$ m at each crossing point is provided to accommodate experiment detectors, with $\pm 7.12$ m for experimental beam pipes, designed for head-on collisions but allowing up to 1.7 mrad crossing angles. The Solenoidal Tracker at RHIC (STAR) is sitting at IP 6 and has been in operation since 2000. STAR encompasses full azimuthal coverage to study high-energy QCD in different collision systems from light to heavy ions, focusing on Au+Au from 7.7 to top RHIC energies, the polarized $p+p$ up to 510 GeV, and
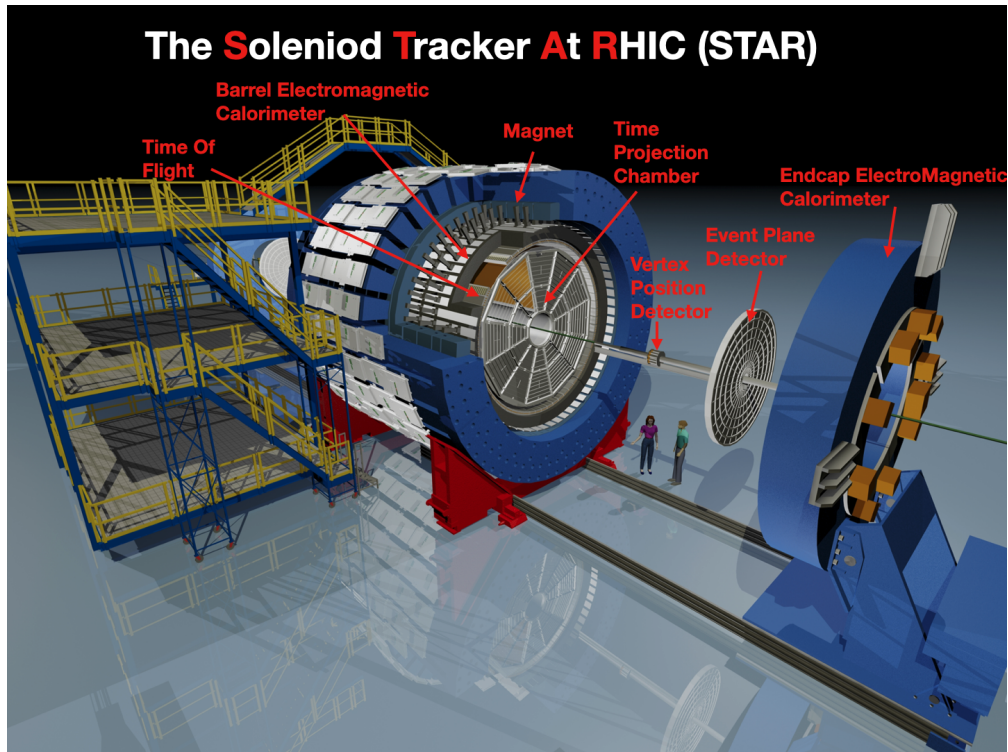
Figure 2.2: Display of STAR detector with BES-II upgrade

other lighter neuclei collisions. A display of the STAR detector is presented in Fig. 2.2, with multiple upgrades since its commissioning. The STAR experiment measures the tracking of charged hadrons via ionization in gas- and silicon-based detectors, and the detection of electrons and photons via calorimetry. The event vertex, track, and particle identification are provided by multiple sub-systems, including the Time Projection Chamber (TPC), known as the heart of STAR, the Time of Flight (TOF) detector, providing comprehensive particle tracking and identification, the Barrel EM Calorimeter and Endcap EM Calorimeter, and the Muon Tracking Detector (MTD) to cover the mid-rapidity region from approximately $-2 < \eta < 2$. In recent years, STAR augmented the Zero Degree Calorimeters - Shower Max Detector (ZDC-SMD), the Vertex Position Detector, the Event Plane Detector (replacing the Beam Beam Counter), Heavy Flavor Tracker (retired), Forward Silicon Tracker in forward and backward rapidities. In addition, the inner TPC (iTPC) and endcap TOF (eTOF) are upgraded in the mid-rapidity region and are crucial to many collision systems. Here we

will briefly introduce the vertex detectors, the TPC and ToF in mid-rapidity, and EPD in forward rapidity that are most relevant to our analysis.

### 2.2.1 Vertex detectors

The ZDCs [88] are located on both sides (east and west) of the interaction point of STAR experiment at the pseudo-rapidity range of $|\eta| > 6$, which is used to steer the beams into collision. The lead-fiber sampling calorimeters utilize Photomultiplier Tubes (PMTs) to detect Cherenkov photons produced in the fibers by charged particles shower. It was designed to measure the energy of beam-fragmentation neutrons, by effectively filtering out virtually all charged particles with the DX magnets. The intrinsic ZDC resolution is better than 150 ps, with an interaction point error of less than 3 cm. A coincidence between the two ZDCs provides a minimum-bias trigger for heavy-ion collisions. It allows RHIC to monitor heavy-ion interaction rates across each detector region during data collection and analyses, typically at 11–13 kHz.

A high-resolution Vertex Position Detector (VPD) [89] is essential for heavy-ion collisions where the multiplicity of produced particles is very high. It is located on both sides of the interaction region, each with 19 PMT/radiator channels and covering a rapidity range of $4.25 < |\eta| < 5.1$. Each channel is constructed from 5.08 cm outer diameter, 0.125 cm thick aluminum cylinders, equipped with fast PMTs attached to 1 cm thick scintillators which view Pb converter plates 1.1 radiation lengths thick. VPD was designed to detect prompt photons from $\pi^0$ decays prevalent at high rapidity in early heavy-ion collisions. Utilizing both modules on the east and west sides can measure the arrival time differences of prompt photons to accurately determine the collision vertex along the beamline. It is very efficient at high rapidity regions in Au+Au collisions and provides the minimum-bias trigger as a measure of the "start time" for other fast-timing detectors. The VPD achieves an offline timing resolution of about 100 ps per channel, leading to a start time precision of tens of picoseconds and a vertex resolution of 1 cm.

### 2.2.2 Mid-rapidity detectors

The STAR Time Projection Chamber (TPC) [90] is the primary detector within a complex suite that provides comprehensive measurement around the collision vertex. It was designed with 4 meters in diameter and 4.2 meters in length, enveloped in a solenoidal magnet exerting a 0.5 T magnetic field. The TPC measures complete tracking information for charged particles across a pseudorapidity range of $\pm 1.8$, particle momenta from 100 MeV/$c$ to 30 GeV/$c$, and identifying particles from 100 MeV/$c$ to greater over 1 GeV/$c$. The typical average transverse momentum per particle in top-energy Au+Au collisions is about 500 MeV/$c$.

TPC is an empty volume of P10 gas (10% methane, 90% argon) at the pressure of 2 mbar above atmospheric pressure. Charged particles traveling through ionize the gas volume, releasing electrons that drift toward the readout end caps under a well-defined, uniform, electric field of 135 V/cm. It allows for precise submillimeter reconstruction of particle paths over drift distances up to 2.1 meters, with a drift velocity of 5.45 cm/ms and a longitudinal diffusion resulting in a time spread of approximately 230 ns (FWHM). The readout modules have 12 sectors, arranged around the central axis with minimal spacing of only 3 mm between each. With the continuous pad coverage in the outer radius subsectors, they enhance the energy deposition ($dE/dx$) resolution to an accuracy of 8% for typical tracks. At typical track multiplicities exceeding 1000 per event, the TPC achieves a vertex resolution of 350 micrometers.

A large-area Time-of-Flight (TOF) detector [91] is developed to enhance particle identification capabilities, particularly addressing limitations in tracking charged hadrons at momenta higher than 1 GeV/$c$ by TPC. The TOF is designed to surround the entire cylindrical surface of approximately 50 m$^2$ based on Multi-gap Resistive Plate Chamber (MRPC) technology, originally developed by CERN's ALICE group. MRPC consists of stacks of resistive 0.54-mm-thick float glass plates separated by uniform 220 $\mu$m gas gaps. Graphite electrodes on the outer surfaces of these plates create strong electric fields across the gaps, to produce
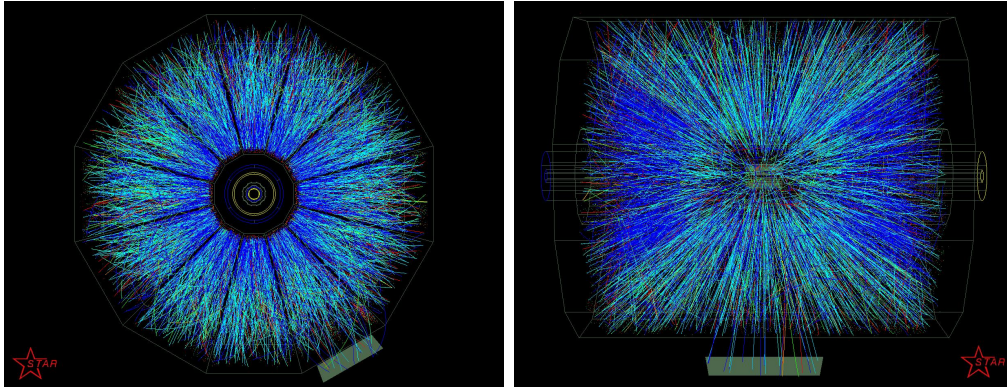
Figure 2.3: First Au+Au Collision Events at RHIC at 100+100 GeV/$c$ per beam recorded by STAR.

Townsend amplification avalanches from primary ionizations of charged particles. On the copper readout pads, signal sums over the avalanches in all of the gas gaps.

The MRPCs at TOF operate in an environment filled with Freon R134a (95%) and isobutane (5%), which allows the rapid amplification of ionization signals. A total timing resolution of 100 ps within the STAR geometry is achieved. With the spatial tracking resolution of the STAR TPC, the integration extends the direct identification range for protons, kaons, and pions up to momenta of approximately 1.7–1.9 GeV/$c$, and for combined proton and kaon identification up to 2.9–3.1 GeV/$c$. By combining the TOF system with $dE/dx$ measurements from the TPC, STAR achieves high-efficiency particle identification across 98% of the hadron spectra and allows for cross-checking particle identification in overlapping momentum regions with TPC.

### 2.2.3 Forward detectors

Installed in 2018, the Event Plane Detector (EPD) [92] is an upgraded detector to replace STAR's original Beam-Beam Counter (BBC). It largely enhances the measurement capabilities of forward-going charged particles in high-energy collisions between heavy nuclei for the pseudorapidity range of $2.14 < |\eta| < 5.09$. At BES-II energies, this coverage spans the spectator region and is thus crucial to our work. EPD is positioned at $z = \pm 3.75$ m from the

interaction point. It provides extensive coverage with the two highly-segmented scintillator disks. Each disk measures a radius of 0.9 m and a central hole of 4.6 cm, and incorporates 1.2 cm-thick scintillators embedded with wavelength-shifting fiber. The east(west) EPD wheel consists of 12 'supersectors', each covering 30 degrees of azimuth and segmented into 31 tiles. These tiles channel light through individual optical fibers to silicon SiPMs, ensuring precise photon detection with minimal crosstalk observed at approximately 5% between adjacent tiles. This configuration improves the resolution of the event plane measured at the forward region by at least two-fold, which effectively translates into a four-fold increase in event statistics.

## 2.3 Dataset collected at STAR

### 2.3.1 Trigger and Vertex

The Trigger System [93] at STAR has undergone significant enhancements over the past 20 years in analytical complexity and operational efficiency. Originally, the system is configured with four levels, and has been refined to meet the advanced readout speed of the Time Projection Chamber (TPC) and the complexity analysis reqruired at Level 0, which synchronizes with the RHIC bunch-crossing clock to select events. Level 1 can abort the data collection process during the TPC's drift time to manage data throughput and prevent data pileup.

The Level 2 trigger, previously used to analyze calorimeter data and control data transfer timing, is now primarily used to compile the trigger data onto the Detector System Module (DSM) and QT boards, without performing additional analysis to effectively serve the data acquisition (DAQ). Subsequently, the Level 3 trigger reconstructs tracks in the TPC, utilizing this data to make the final decision to accept or abort the event.

Data digitization is performed on QT boards and, along with summary data from slower detectors processed on DSM boards, is evaluated by the Trigger Control Unit (TCU) for trig-

ger decisions. These decisions are communicated through the STAR Trigger Pusher (STP) network to Level 2 (L2), and the entire process is coordinated using 14 VME crates. High-level trigger (HLT) decisions are executed separately in L2 to optimize system performance. Collision events that meet all predefined criteria are sent for reconstruction.

In the reconstruction of a triggered event at STAR, the exact three-dimensional collision vertex within the beam pipe is determined [94] by extrapolating the trajectories of TPC tracks back to their origin. It requires using clustering algorithms such as Pile-up Proof Vertexer (PPV) for $p+p$ and Minuit-based Vertex Finder (MinuitVF) [95] for Au+Au events. The timing of the collision, $t_0$, is established by VPD. To overcome pile-up contamination in vertex reconstruction in TPC, vertex ranking based on fast non-tracking detectors e.g. EM calorimeter and Time of Flight detector, are employed to mitigate the effect. Beamline parameters are potentially used as additional constraints to rejecting pile-up events, in addition to the vertex locations in radial or longitudinal axes. The Distance of Closest Approach (DCA), the minimal proximity of the track to the vertex, is also computed and is essential for distinguishing primary particles, which emanate directly from the collision, from secondary particles, which result from decays of other particles.

### 2.3.2 Centrality Determination

In non-central collision, the two nuclei generate various geometric sizes in the overlap region, which affects participant partons and the resulting physics in the final state. Since we cannot directly measure the impact parameter, the distance between the centers of the two colliding ions, the centrality of the collision is estimated from the multiplicity of final-state particles.

At STAR, centrality is determined using the reference multiplicity (RefMult), which counts the total number of primary track particles within $|\eta| < 0.5$. This is compared with simulations from the Monte-Carlo Glauber model to establish centrality for events with a vertex radius $V_r < 2$ cm and a longitudinal vertex $|V_z| < 145$ cm. The initial event selection involves a Quality Assurance (QA) protocol that excludes physically problematic runs. The

bad-run list includes runs deviating from the mean physical quantity by more than five times the local standard deviation, and those identified in run-log assessments as problematic due to reasons such as aborted beams or significant detector malfunctions.

In addition, pile-up events, which result from high-frequency collisions, are identified and excluded using discrepancies between the fast and slow detectors of the TPC and ToF. Subsequent rejections of pile-up are based on outliers in TPC RefMult compared to ToF-matched RefMult. For each Vz interval of 10 cm within $-145 < V_z < 145$ cm, the high-end knee ($h$ in the RefMult distribution is determined using a fitting function with $250 <$ RefMult $< 350$. Corrections are applied based on the $h$ distribution versus $V_z$ and normalized to the most central $V_z$ to account for detector inefficiencies.
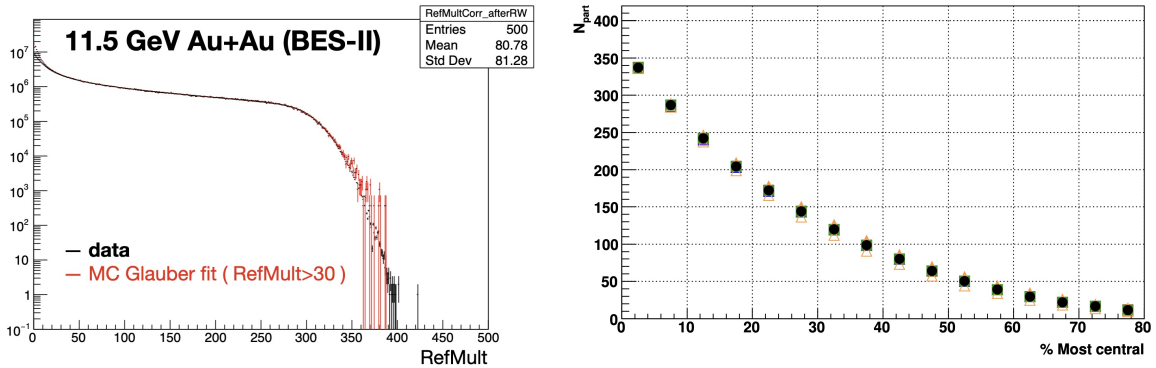


Figure 2.4: (Left)Centrality definition is conducted based on the reference multiplicity distribution of data in comparison to the MC Glauber. (Right) The corresponding number of participating nucleons was obtained at each centrality.

A Monte-Carlo Glauber scan is then conducted to adjust parameters such as the skin depth ($d = 0.535$ fm) and the inelastic NN cross-section. The negative binomial distribution (NBD) scan incorporates a RefMult threshold of 30 and varies theoretical parameters including $n_{pp}$, $k$, $x$, considering detector efficiency, as shown in Fig. 2.4 (left). Centrality is categorized in 5% increments based on the total area under the Glauber curve. Integration from 0-20% relies on data, and from 20-80%, the integration is based on Glauber simulations. Event weights to compensate for the reconstruction inefficiency are calculated using

the ratio of MC to data over the 20–80% centrality range. The number of participating nucleons ($N_{\text{part}}$) is obtained by Glauber calculations and shown in Fig. 2.4(right). The standard centrality definition procedure is applied individually to each of the BES-II energies.

# CHAPTER 3

# Methodology

The background in the CME measurements primarily arises from the collective expansion of the QGP coupled with charge separations such as resonance decays. The collective flow involved in the background receives contributions from both the initial overlap geometry and significant emission pattern fluctuations. One strategy to control background is to measure the signal difference between two similar systems, e.g., in the blind analysis of isobar collisions. The other is to develop a new method capable of directly removing the CME background by capturing the emission pattern, known as the Event Shape Selection. While the use of event planes from spectators suppresses the nonflow backgrounds, I will also discuss the potential longitudinal-decorrelation effect.

## 3.1   The flow background in CME

Let's start by considering the simple case of resonance decay: a single $\rho^0$ meson traveling within the reaction plane ($\Psi_{\rm RP}$) decays quickly into two pions ($\pi^\pm$) in opposite directions in its rest frame. (a) In the first case, the two $\pi^\pm$ are observed at $\pm 45°$ relative to the reaction plane in the lab frame. Here, we obtain a non-zero $\Delta\gamma_{112} = 1$, though the measured elliptic flow, $v_2 = \langle \cos(2\varphi - 2\Psi_{\rm RP}) \rangle$, is zero. (b) In the second case, the decay pions are so highly boosted as to follow the direction of their parent. In this case, both $\Delta\gamma_{112}$ and $v_2$ of the emitted particles are 1. The two pictures represent the "hidden" and "explicit" anisotropy of the emission pattern, respectively, and the first one cannot be controlled directly by the $v_2$ of final-state particles. In both cases, the $\rho^0$ meson (resonance) $v_2$ or $v_2^{\rm res}$ is found to be 1.
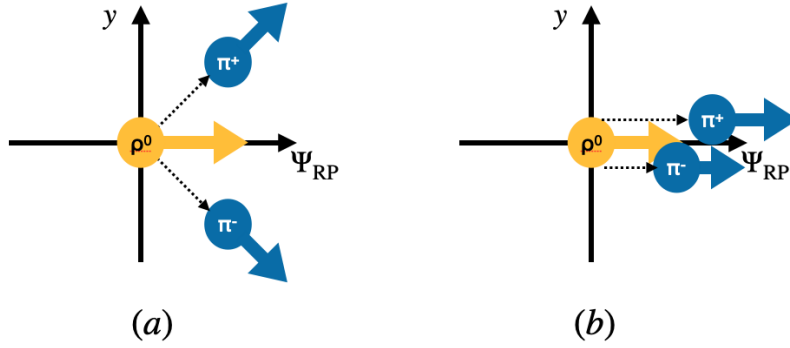
Figure 3.1: Resonance decay background from the hidden (a) or explicit (b) anisotropy.

In collider experiments, resonance meson formed in the QGP are pushed out by the pressure gradients, which on average collimate with the reaction plane. Consequently, the CME background arising from the charge separation mechanism is expected to be related to the resonance $v_2^{\text{res}}$, which shares the same eccentricity origin with the primordial particles such as heavy hadrons. In this section, we need to examine the origin of the flow background in the CME measurement.

Our interest is the widely reported $\Delta\gamma_{112}$ that contains true charge separation signal from CME and the background:

$$\Delta\gamma_{112} \;=\; \gamma_{112}^{\text{OS}} - \gamma_{112}^{\text{SS}} \tag{3.1}$$

$$=\; (a_{1,+}^2 + a_{1,-}^2)/2 - a_{1,+}a_{1,-} + \Delta\gamma_{BG} \tag{3.2}$$

$$=\; 2a_1^2 + \Delta\gamma_{BG}^{\text{flow}} + \Delta\gamma_{BG}^{\text{nonflow}} \tag{3.3}$$

where $2a_1^2 \equiv (a_{1,+}^2 + a_{1,-}^2)/2 - a_{1,+}a_{1,-}$ denotes the CME signal part, and $\Delta\gamma_{BG}$ are background contributions consisting of both flow ($\Delta\gamma_{BG}^{\text{flow}}$) and nonflow effects ($\Delta\gamma_{BG}^{\text{nonflow}}$). The nonflow correlations are unrelated to the reaction plane and originate from various sources such as clusters, resonances, jets, or di-jets. More discussions related to nonflow will be made in future sections.

Here, we will first look at the major source of the CME flow background arising from the

flowing resonances, which undergo decay into particles $\alpha$ and $\beta$ [46]:

$$\Delta\gamma_{BG}^{\text{res}} \propto v_2^{res}\langle\cos(\varphi_\alpha + \varphi_\beta - 2\varphi_{\text{res}})\rangle. \tag{3.4}$$

The background relation in Eq. (3.4) can be validated with a toy model [50] that uses the event generator PYTHIA6 [96] to simulate the decay mechanism of $\rho \to \pi^+ + \pi^-$. This is the major $\pi$ decay channel in the experiment. Each simulation event generates 33 pairs of $\pi^\pm$ from $\rho$ meson decays, matching the multiplicity observed by STAR in 30–40% Au+Au collisions at $\sqrt{s_{NN}} = 200$ GeV within the rapidity range of $|y| < 1$ [97], [98]. The model has inputs of spectrum and elliptic flow for $\rho$ mesons as described in Ref. [50], where the $\rho$-meson spectrum is defined by $\frac{dN_\rho}{dm_T^2} \propto \frac{e^{-(m_T-m_\rho)/T}}{T(m_\rho+T)}$, with $T = 317$ MeV to accurately reproduce the mearsured average of $\langle p_T \rangle$ of 830 MeV/$c$ [98]. We do not have the CME signal here, and will focuses on pions with $0.2 < p_T < 2$ GeV/$c$.
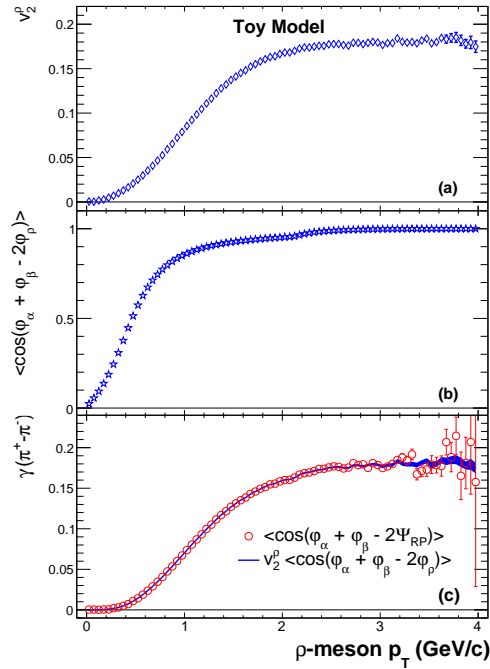


Figure 3.2: Toy model simulations to illustrate the flowing resonance decay background (a) the elliptic flow $v_2$ of $\rho$-mesons, (b) the correlation between a $\rho$-meson and its daughter pions (c) the measured $\gamma_{112}$ correlator for sibling pions. Cited from our work [77].

The first term $\rho$-meson $v_2$ on the right-hand side of the equation is displayed in Fig. 3.2(a),

while Fig. 3.2(b) illustrates the second term, the correlation $\langle\cos(\varphi_\alpha+\varphi_\beta-2\varphi_\rho)\rangle$ between a $\rho$ meson and its daughter pions, attributable solely to decay kinematics. As the transverse momentum ($p_T$) of the $\rho$-meson increases, the daughter pions become more closely aligned with the parent's motion. Fig. 3.2(c) presents the left hand of the equation, the background $\gamma_{112}$ correlator for sibling pions, which aligns closely with the product $v_2^\rho\langle\cos(\varphi_\alpha+\varphi_\beta-2\varphi_\rho)\rangle$. This supports the relationship outlined in Eq. (3.4) and validates the background due to the decay of flowing resonances under no CME input.

Since the picture of flowing resonance can be generalized to similar background mechanisms, such as from elliptic flow coupled with transverse momentum conservation (TMC) and local charge conservation (LCC), which also prompts pair particles' production of opposite sign, this elliptic flow dependence is expected to hold generally. However, experiments can only measure final-state particles, raising the critical question of whether elliptic flow from resonances or particle pairs can directly control the flowing dynamics contributing to the CME observable. In a more general respect, the flow-related background in $\Delta\gamma_{112}$ can be written as a function of elliptic flow ($v_2$),

$$\Delta\gamma_{112}^{\text{flow}} \propto v_2. \tag{3.5}$$

Reducing elliptic flow should effectively suppress this background. Given that $\langle\cos(\varphi_\alpha+\varphi_\beta-2\varphi_\rho)\rangle$ consistently remains positive, it may seem a conceptually easy attempt to directly use resonance $v_2^{\text{res}}$ for controlling the elliptic flow background. However, in experiment, the measurement of resonances by the excess of opposite-sign (OS) over same-sign (SS) particle pairs is found to be significantly influenced by the Chiral Magnetic Effect.

In other words, the relation of Eq. (3.4) fails when there is a CME signal. This can be tested with the Event-By-Event Anomalous Viscous Fluid Dynamics (EBE-AVFD) model [99][100][101], which contains dynamical CME transport for light quarks, and addresses background mechanisms including the flowing resonances, TMC, and LCC. The CME initial conditions can be adjusted by the chirality charge density ($n_5$) over the entropy density ($s$), $n_5/s$, with the electromagnetic fields based on event-specific nucleon configurations from Monte Carlo

Glauber simulations. The CME transport follows the anomalous hydrodynamic equations treated as linear perturbations to the medium flow, managed by the VISH2+1 simulation package [102]. During freeze-out, the model adjusts the LCC to align with experimental observations. After freeze-out, hadrons evolve through the UrQMD simulations [103], which handle resonance decays and their impact on charge-dependent correlations. We simulated events of $9.6 \times 10^7$, $5.9 \times 10^7$, and $7.7 \times 10^7$ for $n_5/s$ values at 0 (pure background), 0.1 (moderate CME signal), and 0.2 (strong CME signal), respectively. The 30–40% Au+Au collisions at $\sqrt{s_{NN}} = 200$ GeV uses same settings and parameters from Ref. [48]. The particles of interest (POI) are $\pi^{\pm}$, restricted to $|y| < 1$ and $0.2 < p_T < 2$ GeV/$c$. The true reaction plane, $\Psi_{\mathrm{RP}} = 0$, is used to avoid nonflow background.
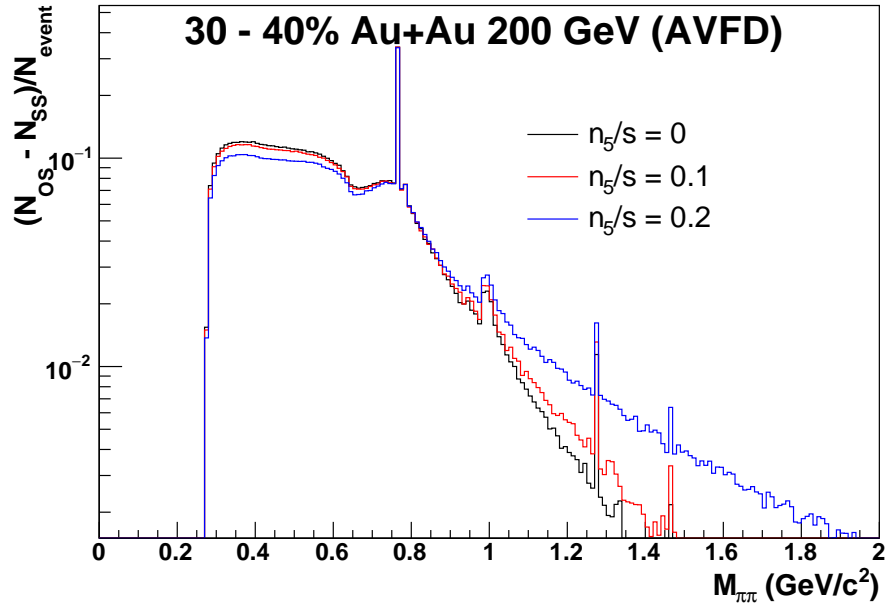


Figure 3.3: EBE-AVFD calculations display the per-event-normalized excess of opposite-sign $\pi$-$\pi$ pairs over same-sign pairs versus invariant mass in 30–40% Au+Au collisions at 200 GeV. In the low-mass region, the sequence from top to bottom corresponds to $n_5/s$ values of 0, 0.1, and 0.2, respectively. This order reverses in the high-mass region. The distinct peaks observed are indicative of resonances like the $\rho$ meson. Cited from our work [77].

The resonance $v_2^{\mathrm{res}}$ is constructed from the invariant mass spectrum per-event, shown in Fig. 3.3, with AVFD simulations at different CME inputs for the normalized excess of OS

over SS pion pairs in 30–40% Au+Au collisions at 200 GeV. Since the invariant mass of the two pions is closely related to their angular separation, the CME, marked by nonzero $n_5/s$ ratios, tends to drive $\pi^+$ and $\pi^-$ in opposite directions, effectively change the opening angle. The CME then increases the observed resonance yield at higher masses, while reducing it at lower masses. As a consequence, the CME modifies the corresponding $v_2$ observable, measured by

$$v_2^{\text{res}} \equiv \frac{N_{\text{OS}}\langle\cos 2\Delta\varphi^{\text{OS}}\rangle - N_{\text{SS}}\langle\cos 2\Delta\varphi^{\text{SS}}\rangle}{N_{\text{OS}} - N_{\text{SS}}}, \tag{3.6}$$

where $\Delta\varphi^{\text{OS(SS)}}$ denotes the azimuthal angle of an OS(SS) particle pair with respect to $\Psi_{\text{R}P}$.

Following a generalized picture of pair production background, we can establish a particle pair $v_2$ that simply adds up two particles momenta for all single particles to mimic the decay/TMC/LCC, defined as

$$v_{2,\text{pair}} \equiv \frac{N_{\text{OS}}\langle\cos 2\Delta\varphi^{\text{OS}}\rangle + N_{\text{SS}}\langle\cos 2\Delta\varphi^{\text{SS}}\rangle}{N_{\text{OS}} + N_{\text{SS}}}. \tag{3.7}$$

With AVFD, we now clearly see how the measurement of elliptic flow for single particle $v_2$, pair $v_2$, and resonance $v_2$ are affected by the CME input $n_5/s$, as in Fig. 3.4. The former two remain roughly constant with respect to the CME, whereas resonance $v_2$ increases significantly with the strength of the CME. By taking the difference in $v_2^{\text{res}}$ between finite CME and pure background, the increase is found linearly proportional to $2a_1^2$, in Fig. 3.4. It implies that the CME can also modify the flowing resonance decay background in the experiment.

The linear relation of resonance $v_2$ that passes through $(0,0)$ can be understood by further mathematical derivation. We assume the true reaction plane $\Psi_{\text{RP}} = 0$ for simplicity. For one kinematic limit, the two particles $\alpha$ and $\beta$ share the same or similar $p_T$, so that $2\varphi^{\text{p}} = \varphi_\alpha + \varphi_\beta$ and $\cos 2\varphi^{\text{p}} = \gamma_{112}$, where $\varphi^{\text{p}}$ is the azimuthal angle of this particle pair. Therefore,

$$v_2^{\text{res}} = \frac{N_{\text{OS}}\langle\cos 2\varphi^{\text{OS}}\rangle - N_{\text{SS}}\langle\cos 2\varphi^{\text{SS}}\rangle}{N_{\text{OS}} - N_{\text{SS}}} \tag{3.8}$$

$$= \frac{N_{\text{OS}} + N_{\text{SS}}}{2(N_{\text{OS}} - N_{\text{SS}})}\Delta\gamma_{112} + \frac{1}{2}(\gamma^{\text{OS}} + \gamma^{\text{SS}}). \tag{3.9}$$
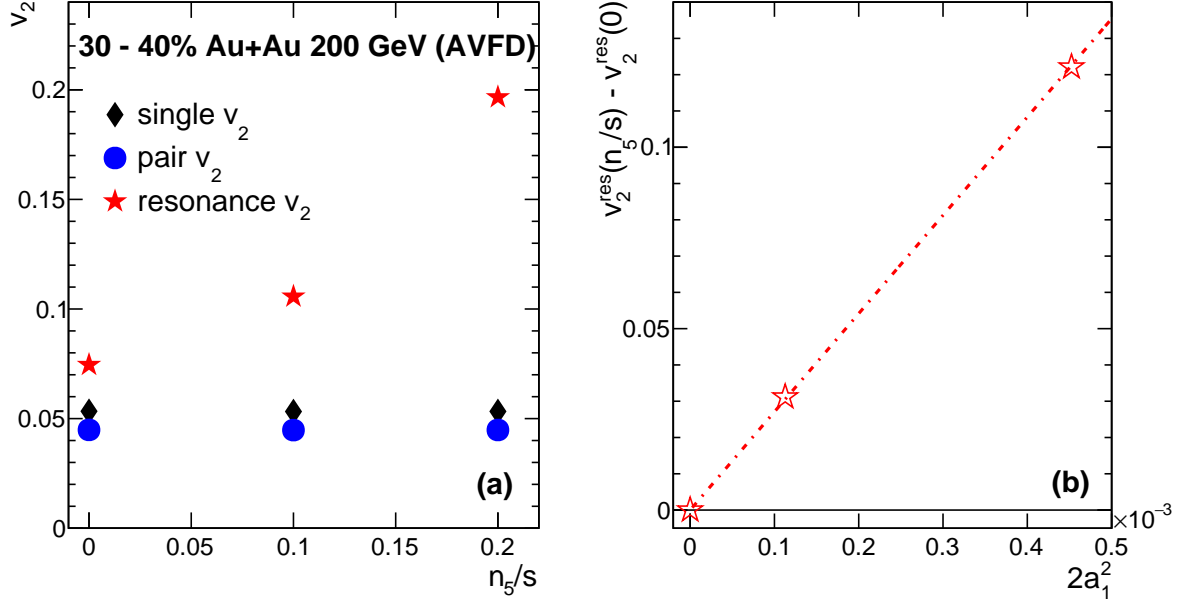
Figure 3.4: (a) EBE-AVFD simulations detail single particle, pair, and resonance elliptic flows ($v_2$) as functions of chirality charge density ($n_5/s$) in 30–40% centrality Au+Au collisions at 200 GeV. (b) Background subtracted resonance $v_2$ as a function of $2a_1^2$ features a linear fit through the origin, indicating that resonance $v_2$ contains a CME signal proportional to $a_1^2$. Cited from our work [77].

$$v_{2,\text{pair}} = \frac{N_{\text{OS}}\langle\cos 2\Delta\varphi^{\text{OS}}\rangle + N_{\text{SS}}\langle\cos 2\Delta\varphi^{\text{SS}}\rangle}{N_{\text{OS}} + N_{\text{SS}}} \tag{3.10}$$

$$= \frac{N_{\text{OS}} - N_{\text{SS}}}{2(N_{\text{OS}} + N_{\text{SS}})}\Delta\gamma_{112} + \frac{1}{2}(\gamma^{\text{OS}} + \gamma^{\text{SS}}). \tag{3.11}$$

For another limit, when $p_{T,\alpha} \gg p_{T,\beta}$, we define a ratio $R \equiv p_{T,\beta}/p_{T,\alpha}$, and thus obtain $\tan\varphi^{\text{p}} = (\sin\varphi_\alpha + R\sin\varphi_\beta)/(\cos\varphi_\alpha + R\cos\varphi_\beta)$. Then, the following trigonometric identity becomes

$$\cos 2\varphi^{\text{p}} = (1 - \tan^2\varphi^{\text{p}})/(1 + \tan^2\varphi^{\text{p}})$$

$$= \frac{\cos 2\varphi_\alpha + R^2\cos 2\varphi_\beta + 2R\cos(\varphi_\alpha + \varphi_\beta)}{1 + R^2 + 2R\cos(\varphi_\alpha - \varphi_\beta)}$$

$$\approx \frac{\cos 2\varphi_\alpha + 2R\cos(\varphi_\alpha + \varphi_\beta)}{1 + 2R\cos(\varphi_\alpha - \varphi_\beta)}. \tag{3.12}$$

Averaging Eq. (3.12) over OS or SS pairs and over events, we have

$$\langle \cos 2\varphi^{\text{OS(SS)}} \rangle \approx (v_2^\pi + 2R\gamma_{112}^{\text{OS(SS)}})/(1 + R\delta^{\text{OS(SS)}})$$

$$\approx v_2^\pi + 2R\gamma^{\text{OS(SS)}} - 2Rv_2^\pi\delta^{\text{OS(SS)}}, \qquad (3.13)$$

where $\delta \equiv \langle \cos(\varphi_\alpha - \varphi_\beta) \rangle$ is the two-particle correlation. We have ignored higher-order terms. Resonance $v_2$ is the elliptic flow for the excess of OS over SS pairs,

$$v_2^{\text{res}} = \frac{N_{\text{OS}}\langle \cos 2\varphi^{\text{OS}} \rangle - N_{\text{SS}}\langle \cos 2\varphi^{\text{SS}} \rangle}{N_{\text{OS}} - N_{\text{SS}}} \qquad (3.14)$$

$$\approx v_2^\pi + \frac{N_{\text{OS}} + N_{\text{SS}}}{(N_{\text{OS}} - N_{\text{SS}})}R(\Delta\gamma_{112} - v_2^\pi\Delta\delta)$$

$$+ R(\gamma^{\text{OS}} + \gamma^{\text{SS}}) - Rv_2^\pi(\delta^{\text{OS}} + \delta^{\text{SS}}), \qquad (3.15)$$

where $\Delta\delta = \delta^{\text{OS}} - \delta^{\text{SS}}$. Regarding the connection to the CME signal, resonance $v_2$ is notably similar to the signed balance functions. Similarly,

$$v_{2,\text{pair}} = \frac{N_{\text{OS}}\langle \cos 2\Delta\varphi^{\text{OS}} \rangle + N_{\text{SS}}\langle \cos 2\Delta\varphi^{\text{SS}} \rangle}{N_{\text{OS}} + N_{\text{SS}}} \qquad (3.16)$$

$$\approx v_2^\pi + \frac{N_{\text{OS}} - N_{\text{SS}}}{(N_{\text{OS}} + N_{\text{SS}})}R(\Delta\gamma_{112} - v_2^\pi\Delta\delta)$$

$$+ R(\gamma^{\text{OS}} + \gamma^{\text{SS}}) - Rv_2^\pi(\delta^{\text{OS}} + \delta^{\text{SS}}), \qquad (3.17)$$

where $\delta \equiv \langle \cos(\varphi_\alpha - \varphi_\beta) \rangle$ is the two-particle correlation.

By looking at the coefficients, the term containing $(N_{\text{OS}} + N_{\text{S}S})/(N_{\text{OS}} - N_{\text{SS}})$ is typically on the order of a few hundred. Then in the first limit, the resonance $v_2$ is dominated by $\Delta\gamma^{112}$ (containing $2a_1^2$) and a momentum conservation background. In the second limit, its second term proportional to $\Delta\gamma$ in Eq. (3.15) is comparable to $v_2^\pi$. This explains why the observed resonance $v_2$ is significantly modified by the existence of the CME, and thus is unsuitable as an elliptic flow variable in the CME background.

In comparison, the pair particle $v_{2,\text{pair}}$ contains a $\Delta\gamma^{112}$ contribution on the order of $(N_{\text{OS}} - N_{\text{S}S})/(N_{\text{OS}} + N_{\text{SS}})$ that is typically a few percent. $v_{2,\text{pair}}$ is thus dominated by the $v_2^\pi$, and remains roughly constant under the CME physics, which may be more suitable to

capture the dynamics of the flowing resonance background. Still, we need to point out that it contains a tiny fraction of the CME, and later we will see the consequence of this in the background subtraction.

Thus, the CME could change the invariant mass spectrum of the pair particles, and alter the observed pair background. Recall that the hidden anisotropy prevents direct use of the elliptic flow in background control, which contains large fluctuations event-by-event on top of the eccentricity [104]. A proper method for background subtraction involves utilizing an observable that is correlated with the elliptic flow via eccentricity, known as "Event Shape", or the emission pattern of the participant region. Since the background primarily arises from pair particles, this emission pattern should encompass both the shapes of resonance decays and primordial particles. The future sections will detail the development of the "Event Shape Selection" method that manage to capture the flowing background through the pair emission patterns.

## 3.2   Non-interdependency of Collective flow

The previous section reviews that the observed flowing charge separation background in $\Delta\gamma^{112}$ is influenced by the existence of the CME. In this section, we will look deeper at the complicated dynamics, and discuss the fact that the observed CME signal ($a_1$) may also be influenced by the collective flow dynamics. This is known as the non-interdependent collective motions in heavy-ion collisions [105], a scenario where different modes of collective motions are driven by factorized actions in the created nuclear medium.

The emission pattern of final-state particles in heavy-ion collisions is seen to reveal different collectivity modes of the created nuclear medium. Figure 3.5 illustrates a few examples of collective motions at midrapidities in noncentral collisions:

a) Directed flow ($v_1$): a slightly tilted participant region  [106] violates the boost invariance, and leads to a rapidity-odd emission of produced particles.
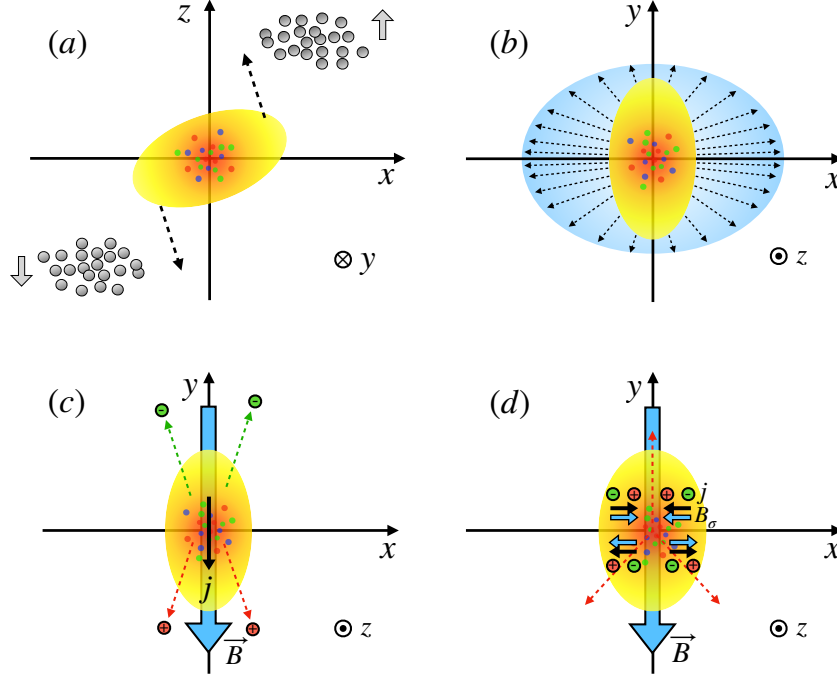
Figure 3.5: Collective motions in heavy-ion collisions: (a) directed flow, (b) elliptic flow, (c) the CME-induced electric current $j$ along the $\vec{B}$ field, and (d) the siCME-induced charge-dependent triangular emission.

b) Elliptic flow ($v_2$): the almond-shaped overlap zone in coordinate space is transformed via a hydrodynamic expansion [47] into a rapidity-even nondegeneracy between in-plane and out-of-plane emissions.

c) The chiral magnetic effect (CME) ($a_1^\pm$) [35] induces an out-of-plane electric charge separation, provided that a quark chirality imbalance emerges from the chiral anomaly, and an intense magnetic field ($\vec{B}$) is generated by protons from the colliding nuclei.

d) The shear-induced CME (siCME) ($a_3^\pm$) [107] has been proposed recently, in which the combination of the magnetic field and hydrodynamic shear creates a charge-dependent triangular flow.

In the widely used notation, the Fourier-expansion in Eq. (1.6) (Ch.1) represents a probability distribution in an orthonormal basis, i.e. $a_1$ is independent of $v_2$, which has a physics

assumption that each collectivity mode in the final states is non-interdependent. However, it leads to a logical inconsistency that if the collectivity modes are orthogonal or non-interdependent, each action should modulate the probability of particle emission with its own single-harmonic ($\tilde{a}_n$ or $\tilde{v}_n$) Fourier expansion. In other words, the probability of particle emission is the product of all these expansions:

$$\frac{2\pi}{N^\pm}\frac{dN^\pm}{d\varphi} = \prod_{n=1}^{\infty}(1 + 2\tilde{a}_n^\pm \sin n\Delta\varphi)\prod_{n=1}^{\infty}(1 + 2\tilde{v}_n^\pm \cos n\Delta\varphi). \tag{3.18}$$

Establishing the relationship between the Fourier coefficients and underlying physics mechanisms is nontrivial. It shows that the observed $a_n$ ($v_n$) may not fully match the true physics representation, $\tilde{a}_n$ ($\tilde{v}_n$), of the pertinent physics process, and may present internal correlations. The physics mechanisms could each dominate at a distinct evolution stage, or coexist simultaneously. Consequently, higher-order cross-terms between lower-order collective modes appear, and their contributions to experimental observables may be significant. In reality, the difference between $a_n$ and $\tilde{a}_n$ or between $v_n$ and $\tilde{v}_n$ is negligible for many harmonics, if the magnitude of $\tilde{a}_n\tilde{a}_m$ could be much smaller than $\tilde{v}_{n+m}$ or $\tilde{v}_{|n-m|}$. The lower-order term is thus to our most interest, namely the $a_1$ (CME) and $v_2$ (elliptic flow), while directed flow ($v_1$) is not included because as a rapidity-odd function, its rapidity-integrated contribution to other coefficients will be zero.

In particular, we argue that the chiral magnetic effect and elliptic flow can develop separately, with their convolution raising a new observable that is sensitive to the shear-induced CME, and modifying the observed $a_1$. In the factorized form of Fourier expansions, $\tilde{a}_1$ and $\tilde{v}_2$ appear in two separate Fourier expansions, $(1 + 2\tilde{a}_1 \sin \Delta\varphi)$ and $(1 + 2\tilde{v}_2 \cos 2\Delta\varphi)$, and their product specifies the final-state particle distribution:

$$4\tilde{a}_1\tilde{v}_2 \sin\Delta\varphi \cos 2\Delta\varphi = -2\tilde{a}_1\tilde{v}_2 \sin\Delta\varphi + 2\tilde{a}_1\tilde{v}_2 \sin 3\Delta\varphi.$$

Thus, we find a connection between phenomena and noumena as the following:

$$a_1 = \tilde{a}_1 - \tilde{a}_1 \tilde{v}_2, \tag{3.19}$$

$$a_3 = \tilde{a}_1 \tilde{v}_2, \tag{3.20}$$

Since $v_2 \simeq \tilde{v}_2$, we can abandon $\tilde{v}_2$, and only use $v_2$ in the following discussions. Eq. (3.19) indicates that the observed $a_1$ roughly equals $\tilde{a}_1(1 - v_2)$. Furthermore, Eq. (3.20) asserts that the observed $a_3$ contains a contribution of $\tilde{a}_1 v_2$ on top of the primordial $\tilde{a}_3$, if any. We can derive $\tilde{a}_1$ in terms of experimental observables: $\tilde{a}_1 = \frac{a_1}{1-v_2}$.
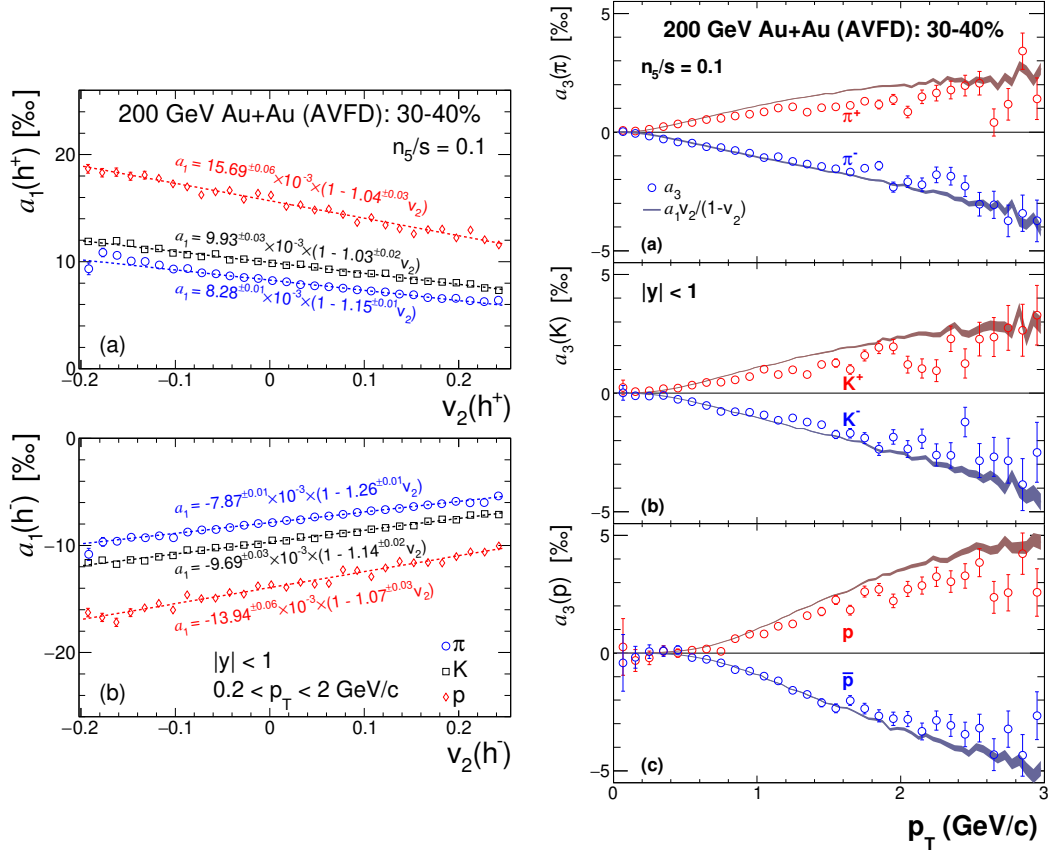


Figure 3.6: (left) Correlations between $a_1$ and $v_2$ and (right) $a_3$ as a function of $p_T$ in comparison with $a_1 v_2/(1 - v_2)$, calculated on an event-by-event basis from EBE-AVFD simulations of 30–40% Au+Au collisions at $\sqrt{s_{NN}} = 200$ GeV for $\pi^\pm$, $K^\pm$ and $p$, $\bar{p}$. Cited from our work [105].

This scenario is tested with the event-by-event AVFD simulations of Au+Au collisions

at 200 GeV in the 30–40% centrality range, shown in Fig. 3.6. In the left panel, a consistent linear correlation between the CME $a_1$ and elliptic flow $v_2$ is observed across different particle types ($\pi^\pm$, $K^\pm$, $p$ and $\bar{p}$), within a rapidity range of $|y| < 1$ and a transverse momentum range of $0.2 < p_T < 2$ GeV/$c$. This correlation is described by the function $a_1(v_2) = a_1(0) \times (1 + Cv_2)$, with the slope parameter $C$ approaching $-1$ for all particles. However, this correlation itself is not strong enough to support the factorized form, since it is limited by other explanations from trigonometric identity: $\sin^2 \Delta\varphi \equiv (1 - \cos 2\Delta\varphi)/2$. Both $a_1$ and $v_2$ could have mathematical relationships before the convolution effect. Additionally, the resonance decay complicates the correlation, particularly for pions. The extracted $a_1(0)$ or $\tilde{a}_1$ values also show a dependence on particle species, likely influenced by variations in mean $p_T$ of pions, kaons, and protons, and might be further modulated by the quark coalescence mechanism.

The observed $a_3$ as a function of $p_T$ in Fig. 3.6 displays strong evidence for the proposed factorized Form. As illustrated in the right panel, the data for $a_3$ align well with the modeled $\tilde{a}_1 v_2$ or the function $a_1 v_2 / (1 - v_2)$ across all particle species, as indicated by the shaded bands that effectively capture both the trends and magnitudes of $a_3$. These observations affirm the predictions of Eq. (3.18). Notably, at $p_T > 1$ GeV/$c$, $a_3$ exhibits a diminished magnitude compared to $\tilde{a}_1 v_2$, partly attributed to the observed anti-correlation between $\tilde{a}_1$ and $v_2$. Additionally, the apparent decrease in hydrodynamic coherence at higher $p_T$ contributes to this discrepancy, as collective flow effects diminish.

For completeness, if we include an additional existence of si-CME ($\tilde{a}_3$), the relation looks as follows:

$$
\text{Phenomena}
\begin{cases}
a_1 = \tilde{a}_1 - \tilde{a}_1 \tilde{v}_2 + \tilde{a}_3 \tilde{v}_2 \\
a_3 = \tilde{a}_3 + \tilde{a}_1 \tilde{v}_2, \\
v_2 = \tilde{v}_2 + \tilde{a}_1 \tilde{a}_3.
\end{cases}
\quad
\text{Noumenon}
\begin{cases}
\tilde{a}_1 = \frac{a_1 - a_3 v_2}{1 - v_2 - v_2^2}, \\
\tilde{a}_3 = \frac{a_3 - a_1 v_2 - a_3 v_2}{1 - v_2 - v_2^2}.
\end{cases}
\tag{3.21}
$$

It is notable that the size of true si-CME $\tilde{a}_3$ could be on the same order as the convolution

effect from $a_1 v_2$. Thus estimatting the true si-CME, if any, may also require taking into account the contribution from the cross-term.
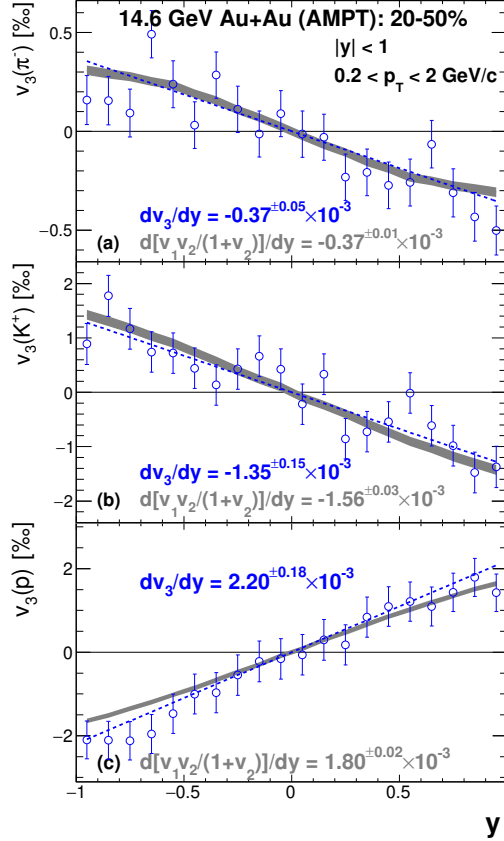


Figure 3.7: AMPT simulations of $v_3$ vs $y$ in comparison with $v_1 v_2 / (1 + v_2)$ for (a) $\pi^-$, (b) $K^+$, and (c) $p$ in 20–50% Au+Au collisions at 14.6 GeV.

Besides the CME search, the conventional flow harmonics $v_1$, $v_2$ and $v_3$, will also be affected by similar relations, and give rise to non-leading cross terms. These tests can be demonstrated in the feasible experimental data and by using a multiphase transport model (AMPT). If directed flow and elliptic flow are approximately non-interdependent in nature, we have the following:

$$\text{Phenomena} \begin{cases} v_1 = \tilde{a}_1 + \tilde{a}_1 \tilde{v}_2 + \tilde{a}_3 \tilde{v}_2 \\ v_3 = \tilde{a}_3 + \tilde{a}_1 \tilde{v}_2, \\ v_2 = \tilde{v}_2 + \tilde{a}_1 \tilde{a}_3. \end{cases} \qquad \text{Noumenon} \begin{cases} \tilde{v}_1 = \frac{a_1 - a_3 v_2}{1 + v_2 - v_2^2}, \\ \tilde{v}_3 = \frac{a_3 - a_1 v_2 - a_3 v_2}{1 + v_2 - v_2^2}. \end{cases} \qquad (3.22)$$

Hence, the observed $v_1$ represents the actual $\tilde{v}_1$ adjusted by the factor $(1 + \tilde{v}_2)$. A new rapidity-odd $v_3$ is included by the $\tilde{v}_1 \tilde{v}_2$, in addition to the true rapidity-even $\tilde{v}_3$ components. In real collisions, $\tilde{v}_3$ is typically negligible as the triangular anisotropy is primarily driven by event-by-event fluctuations and largely independent of the reaction plane [108]. Thus, the presence of an odd component in $v_3$ serves as a distinct marker of the factorized Fourier expansions. We utilize the string melting version of the multi-phase transport (AMPT) model [109][110] to simulate Au+Au collisions at $\sqrt{s_{NN}} = 14.6$ GeV/$c$ where directed flow is significant. Figure 3.7 displays AMPT-generated $v_3$ versus rapidity $y$ for $\pi^-$, $K^+$, and $p$ within the 20–50% centrality range. Due to the transported-quark effect, we present particles and antiparticles separately. The shaded band $v_1 v_2 / (1 + v_2)$ is well represented by the observed $dv_3/dy$ across all particle types, supporting the scenario of non-interdependent collective motions.

The above two examples support the universality of the collective motions as non-interdependent, that the particle azimuthal distribution can take a factorized form. This scheme is more self-consistent, better captures the genuine strength of each collectivity mode, and makes new predictions based on nonleading cross-terms. Since most CME-sensitive observables contain $a_1^2$, the corresponding reduction factor should be about $(1 - v_2)^2$. In other words, the observed CME signal is also expected to be influenced by the presence of elliptic flow dynamics.

## 3.3 Spectator Plane and decorrelation effects

The nonflow background $\Delta\gamma_{\mathrm{BG}}^{\mathrm{nonflow}}$ in Eq. (3.3) comes from mechanisms that can simultaneously contaminate $\varphi_\alpha$, $\varphi_\beta$, and the estimation of $\Psi_{\mathrm{RP}}$, leading to a finite $\Delta\gamma_{112}$ value even in the absence of genuine $a_1$. Nonflow effects are more conspicuous in smaller systems with lower multiplicities, like $p$+Au and $d$+Au collisions at $\sqrt{s_{NN}} = 200$ GeV [61]. In practical applications, to eliminate nonflow, the reaction plane can be approximated with the event plane defined by spectator nucleons [69], [70]. As spectators exit the participant zone early in the collision, the influence of most nonflow mechanisms becomes negligible when the spectator plane is used. While the momentum conservation effect could potentially impact spectators, deploying two spectator planes symmetrically positioned in rapidity effectively eliminates this effect, as demonstrated in prior flow measurements [111], [112]. Even with just one spectator plane, the momentum conservation effect can be nullified in observables like $\Delta\gamma_{112}$, as $\gamma_{112}^{\mathrm{OS}}$ and $\gamma_{112}^{\mathrm{SS}}$ are affected in the same manner [60], [112].
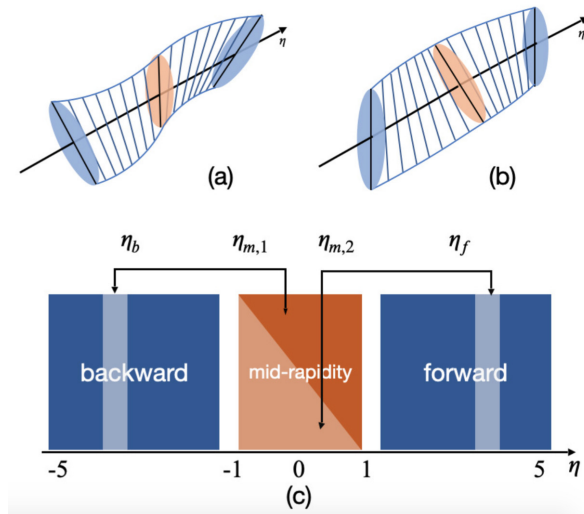


Figure 3.8: Schematic view of longitudinal distribution of the flow plane angle. Panel (c) delimits the kinematic regions for the particles at mid-, forward, and backward pseudorapidities.

Although the spectator plane can suppress the nonflow effects, the possible existence of a longitudinal decorrelation for flow plane at forward/backward (pseudo)rapidity($\eta$) may

affect the efficiency of measurement. This flow plane decorrelation may come from initial nuclear matter density distributions [113], the torque effect [114] [115], hydrodynamic fluctuations in the QGP fluid [116], and glasma dynamics [117]. Experimental measurements of factorization ratio $(r_2)$[118] and its derivative $(F_2)$[119][120][121] have shown non-zero values, but are affected by nonflow effects. If such an effect exists in the spectator region, it potentially affects the application of spectators and must be addressed in advance. To test the decorrelation effect of the flow plane [122], we design a new observable, the Twist observable $(T_2)$, which is sensitive to the two scenarios: (a) the "torque" or S-shaped and (b) the bow or C-shaped decorrelation patterns in the longitudinal distribution of the flow plane angle.

The Twist correlator as a four-particle cumulant is essentially free from non-flow contribution.

$$T_2 = \frac{\langle \sin 2(\Psi_f - \Psi_{m,1}) \sin 2(\Psi_b - \Psi_{m,2}) \rangle}{\langle \cos 2(\Psi_f - \Psi_{m,1}) \cos 2(\Psi_b - \Psi_{m,2}) \rangle} - \frac{\langle \cos 2(\Psi_f - \Psi_b) \rangle \langle \cos 2(\Psi_{m,1} - \Psi_{m,2}) \rangle}{2 \langle \cos 2(\Psi_f - \Psi_{m,1}) \rangle \langle \cos 2(\Psi_b - \Psi_{m,2}) \rangle} + \frac{1}{2}.$$

Thus, mathematically a positive $T_2 = \frac{1}{2} \tan^2[2\frac{d\Delta\Psi}{d\eta}(|\eta_{f(b)}| - 0.5)]$ would reflect a bow or a C-shaped decorrelation, and a negative $T_2 = -\frac{1}{2} \tan^2(2\frac{d\Delta\Psi}{d\eta}|\eta_{f(b)}|)$ signifies a torque or an S-shaped decorrelation. We employed a realistic model that uses Simple Monte Carlo calculations for the underlying event (UE) without nonflow and for different nonflow physics from pair, and from PYTHIA [96] events generated for $p+p$ collisions at $\sqrt{s} = 200$ GeV or 2.76 TeV. After adding a linear-$\Delta\Psi(\eta) = 2°$ decorrelation effect, the qualitative dependence of $T_2$ on $|\eta_{f(b)}|$ are shown in Fig. 3.9 with a rapid decreasing trend for the S-shaped case in panel (a), and an increasing trend for the C-shaped case in panel (b). The dotted curve manifests the two analytical equations without nonflow. With the AMPT model simulation, the decorrelation effects at mid-central events of 20–50% is found to be zero for forward regions $2 < |\eta| < 5$, as shown in Fig. 3.9.

We measured the $T_2$ correlator in STAR Au+Au collisions at 200 GeV and 27 GeV, and observed no significant decorrelation at 20–50% centrality in forward rapidity regions,
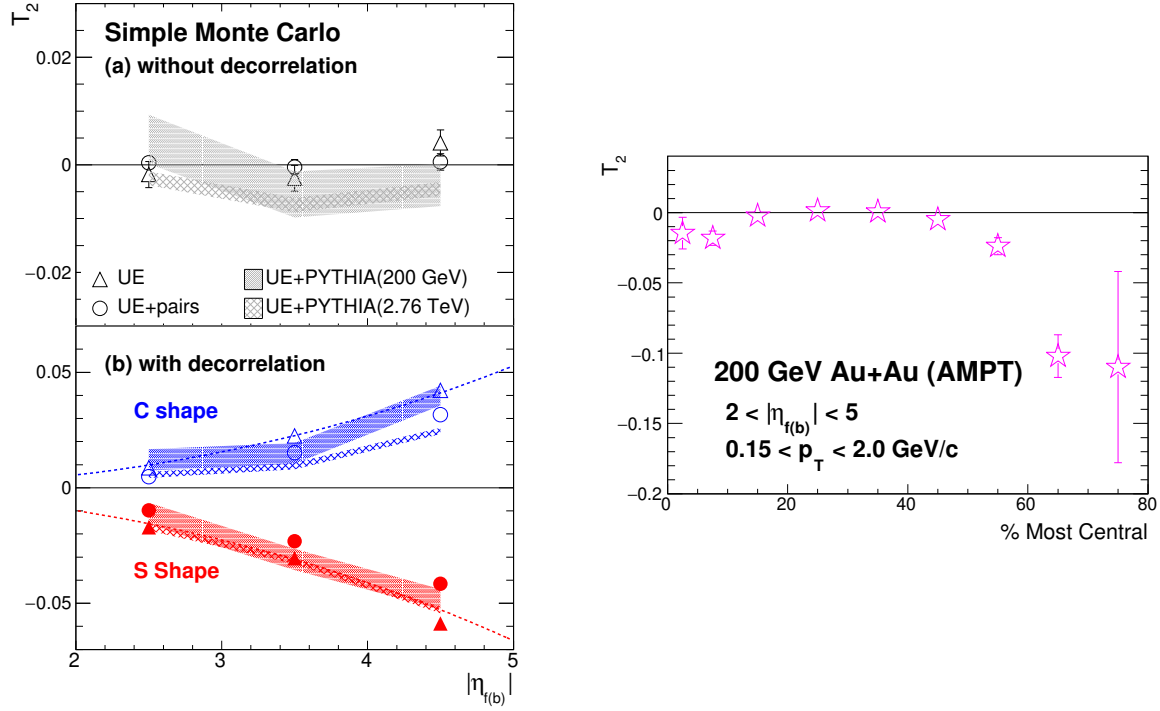
Figure 3.9: (Left) Simple Monte Carlo calculations of $T_2$ w/o and with decorrelation for the S-shaped and the C-shaped flow-plane decorrelations. (Right) AMPT simulations of $T_2$ in Au+Au collisions at 200 GeV. Cited from our work [122].

as shown in Fig. 3.10. Furthermore, we find that effects diminish towards more forward directions represented by inner BBC rings, causing $T_2$ values to approach zero. At 27 GeV, the nonflow impact clearly shown in the $F_2$ observable is significantly reduced with $T_2$, which consistently aligns with zero. Given the spectator region is beyond beam rapidity, typically chosen to be $|\eta| > 3.8$ at this energy, we argue that using spectator information should exhibit nearly no decorrelation effects. Therefore, for the Chiral Magnetic Effect (CME) analysis, we propose utilizing the spectator plane to measure the magnetic field direction and mitigate nonflow effects.
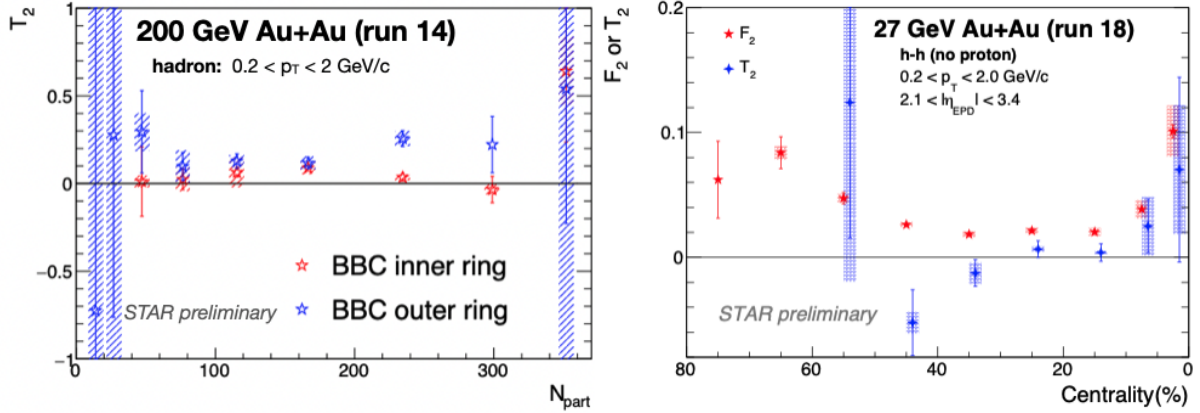
Figure 3.10: Decorrelation measurement with $T_2$ and $F_2$ in Au+Au collisions at 200 and 27 GeV.

## 3.4 Isobar analysis

To address the challenge of a significant background in measurements, two scientific approaches are common. The first strategy is conducting a controlled experiment to detect subtle signal differences between two measurements. The second is to directly mitigate the background which will be detailed in the following section of the Event Shape Selection. In this section, we discuss the major DOE project as an example of the first strategy, the STAR blind analysis of isobar collisions [65] using Ruthenium+Ruthenium ($^{96}_{44}\text{Ru}+^{96}_{44}\text{Ru}$) and Zirconium+Zirconium ($^{96}_{40}\text{Zr}+^{96}_{40}\text{Zr}$), and our findings to understand the post-blind analysis.
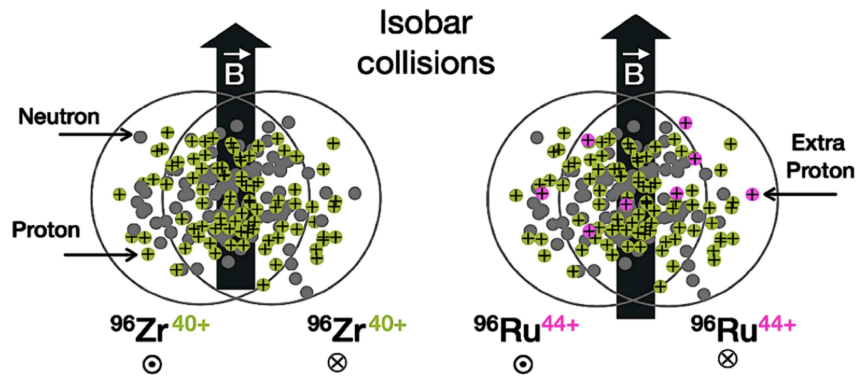


Figure 3.11: Isobar systems in a non-central collision for $^{96}_{40}\text{Zr}+^{96}_{40}\text{Zr}$ and $^{96}_{44}\text{Ru}+^{96}_{44}\text{Ru}$.

Isobar collisions employ two nuclear systems, $^{96}_{40}$Zr and $^{96}_{44}$Ru, which have the same total nucleon number (A=96) but different atomic numbers (Z), enabling comparisons under similar background conditions but with varying signal intensities [123]. The $^{96}_{44}$Ru nuclei, possessing four additional protons compared to $^{96}_{40}$Zr, are expected to generate an approximately 10% stronger magnetic field [35], [124], leading to a 15% increase in the Chiral Magnetic Effect signal in Ru+Ru collisions, while maintaining comparable flow-driven backgrounds due to their identical mass numbers. After rewriting Eq. (3.3), we expect the following:

$$\Delta\gamma^{\mathrm{Ru+Ru}} = \Delta\gamma^{\mathrm{CME}} + k \times \frac{v_2}{N} + \Delta\gamma^{\mathrm{nonflow}}_{BG}, \tag{3.23}$$

$$\Delta\gamma^{\mathrm{Zr+Zr}} = \underbrace{\Delta\gamma^{\mathrm{CME}}}_{15\% \text{ more in Ru}} + \underbrace{k \times \frac{v_2}{N}}_{4\%} + \underbrace{\Delta\gamma^{\mathrm{nonflow}}_{BG}}_{\text{same}}. \tag{3.24}$$

Although similar, the backgrounds in Ru+Ru and Zr+Zr collisions are not identical. The difference in the nuclear deformation of the two isobars was estimated to yield less than 1% difference in $\Delta\gamma$ background. For the flow background, an approximate 4% difference between these two systems is originally estimated [125]. At this beam energy, the beam rapidity exceeds the coverage of the EPD, therefore we did not use a high-resolution spectator plane. The corresponding nonflow background is believed to be canceled effectively by taking the ratio of the two isobar systems, as it is more correlated with the system size. Isobar is thus considered an effective way to achieve crucial systematic controls in minimizing background contributions to search for the possibly small CME signal.

To account for the difference in $v_2$, the pre-defined CME signal focuses on the ratio $\Delta\gamma/v_2$ that assumes the background proportionality to $v_2$ is identical between the isobar systems. The expected ratio of $\frac{\mathrm{Ru+Ru}}{\mathrm{Zr+Zr}}$ in the CME picture would be larger than unity; while it will be equal to unity for the pure-background picture. If we constrain the CME-related signal fraction

$$f_{\mathrm{CME}} = \frac{\Delta\gamma^{\mathrm{CME}}}{\Delta\gamma_{112}}, \tag{3.25}$$

by $f_{\mathrm{CME}} \simeq 14\%$, with 2 billion minimum-bias (MB) events obtained at RHIC for each
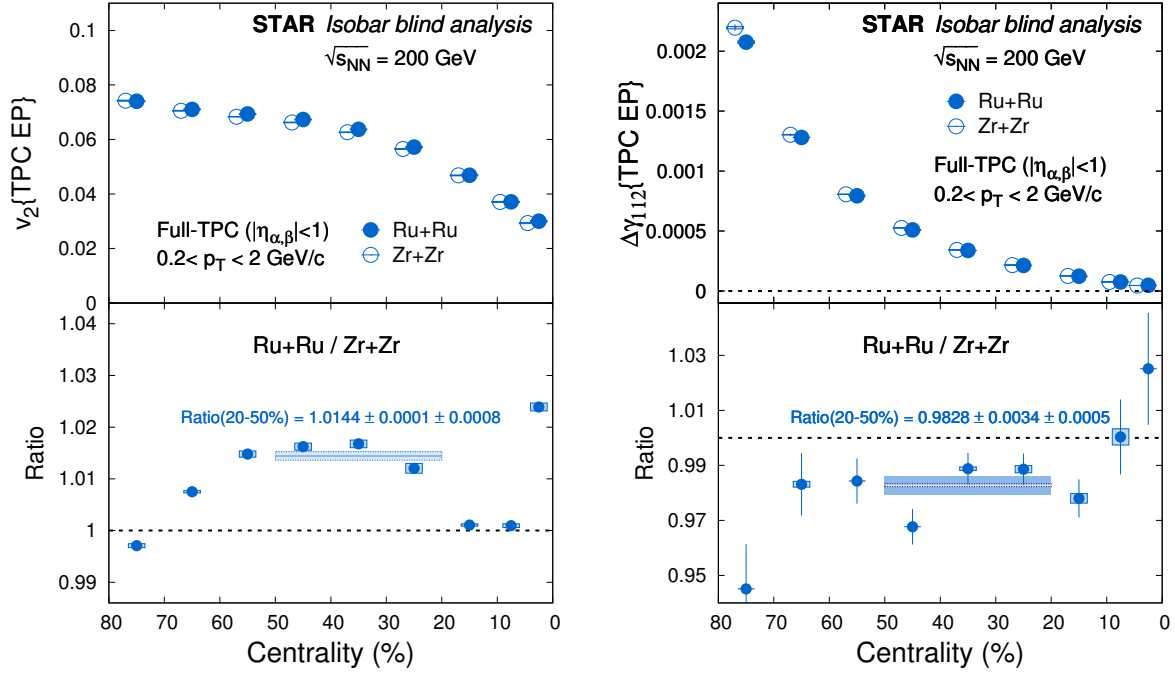
Figure 3.12: $v_2$ and $\Delta\gamma^{112}$ measured with the full TPC event plane (EP) in Ru + Ru and Zr + Zr collisions at 200 GeV, with their ratio presented in the lower panels. Cited from [65].

collision system, a $5\sigma$ significance from unity is expected in the ratio between Ru+Ru and Zr+Zr due to the CME.

The $v_2$ and $\Delta\gamma^{112}$ values measured with event plane from TPC as a function of centrality for Ru+Ru and Zr+Zr collisions at $\sqrt{s_{\mathrm{NN}}} = 200$ GeV are shown in Fig. 3.12, and the lower panels present the ratios between the two isobaric systems. The $v_2$ ratio averaged over the 20–50% centrality range is $1.0144 \pm 0.0001(stat.) \pm 0.0008(syst.)$, significantly above unity. The $\Delta\gamma_{112}$ ratio averaged over the 20–50% centrality range is $0.9828 \pm 0.0034(stat.) \pm 0.0005(syst.)$, which is not sensitive to the $\eta$ gap between the two particles or between the event plane and the particles. It reveals that $^{96}_{44}$Ru and $^{96}_{40}$Zr nuclei possess different nuclear density distributions and Ru+Ru is more deformed, resulting in higher eccentricity for Ru+Ru collisions compared to Zr+Zr collisions at the same centrality.

With five independent analyzing groups, we summarize the results in Fig. 3.13 for the
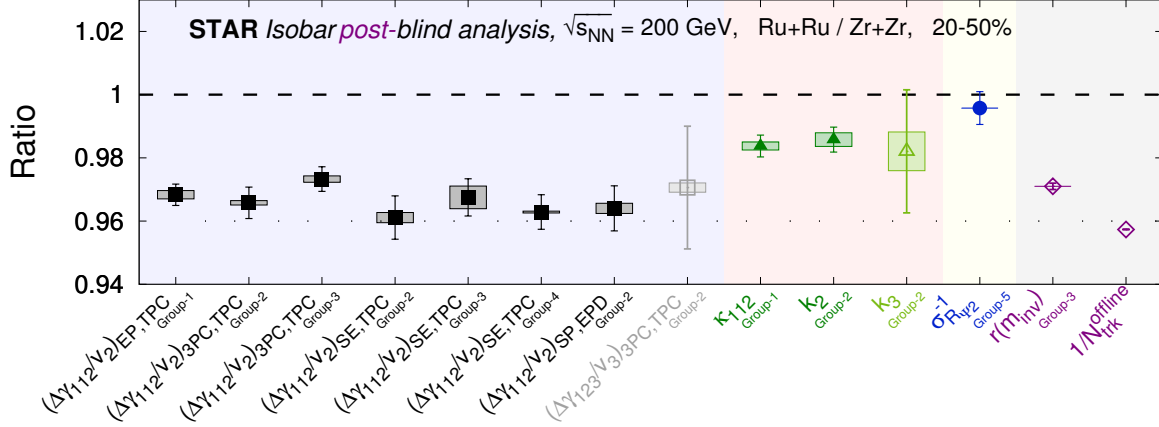
Figure 3.13: Isobar blind analysis with multiple observables for $^{96}_{40}Zr+^{96}_{40}Zr$ and $^{96}_{44}Ru+^{96}_{44}Ru$ in comparison to the baseline, cited from [65].

primary CME-sensitive observable $\Delta\gamma/v_2$ at different kinematic regions and detector combinations, and one result from the $R$ correlator. Prior to the blind analysis, the CME signature is predefined to be an excess of $\Delta\gamma/v_2$ in Ru+Ru compared to Zr+Zr collisions. Results from all groups observed the ratio below 1, inconsistent with this expectation. In the figure, solid dark symbols represent measures sensitive to the CME, while open light symbols denote measures believed to be insensitive to the CME. Different types of measures are distinguished by varying background colors. Moreover, the background quantity $\Delta\gamma_{123}/v_3$ and $k_3$ present ratios similar to the CME-sensitive counterparts. The consistent fact that the ratios of CME-sensitive observables are below unity leads to the conclusion that no predefined CME signatures were observed in this blind analysis.

After unblinding the isobar species, we observe the multiplicity difference between the two isobaric systems at a given centrality, as indicated as the last data point in Fig. 3.13 for the ratio of inverse multiplicities $N_{\mathrm{trk}^{offline}}$. This background mismatch from multiplicity is found to be the main reason for the ratio of two isobaric systems lower than unity. Recently, after forced-matching multiplicity, the post-blind analysis reported the isobar ratio to be consistent with one, yielding an upper limit of the CME signal fraction $f_{\mathrm{CME}}$ around 7%

in isobar collisions at the 95% confidence level. In addition, it has been pointed out and supported by AVFD simulations that the CME signal fraction could be substantially smaller in isobar collisions compared to Au+Au collisions [126], where the latter measured to be around 10% at 200 GeV with 1–3$\sigma$ significance [69]. This reduction of $f_{\text{CME}}$ is more notable in using the participant plane for measurement, potentially doubling the severity of signal suppression.

These findings from the isobar analysis advocate a return to larger collision systems, such as Au+Au, which have a higher atomic number (Z) and enhance the magnetic field by three to four times, in observation of the CME. Smaller nuclei systems are found to encompass larger background fluctuations, in comparison to the larger systems such as Au+Au, which further suppress the CME signal. In consideration of the key condition of the magnetic field, collisions at lower energies are preferred for observing the CME, such as in Au+Au collisions of BES-II, since their magnetic field decays more slowly than the top RHIC energy. Moreover, it is also less favorable to use the participant plane which encompasses nonflow background and causes dilution effects for the signal. A high-resolution spectator plane is crucial for reconstructing the magnetic field direction and avoiding nonflow backgrounds in the CME measurement. At BES-II, this can be achieved by the newly installed EPD detector.

More importantly, the first strategy aims for a controlled experiment using methods in search of signal differences and hold an assumption that the coupling of $v_2$ to flow background is universal across different systems, allowing for indirect control over a background by taking ratios. However, this assumption may not hold due to the difference in nuclei deformation, nuclear fluctuation, and kinematic correlations between the two measurements. Alternatively, we develop a new technique to directly isolate the flow background in measurements. This approach will be discussed in the next section.

## 3.5 Event Shape Selection
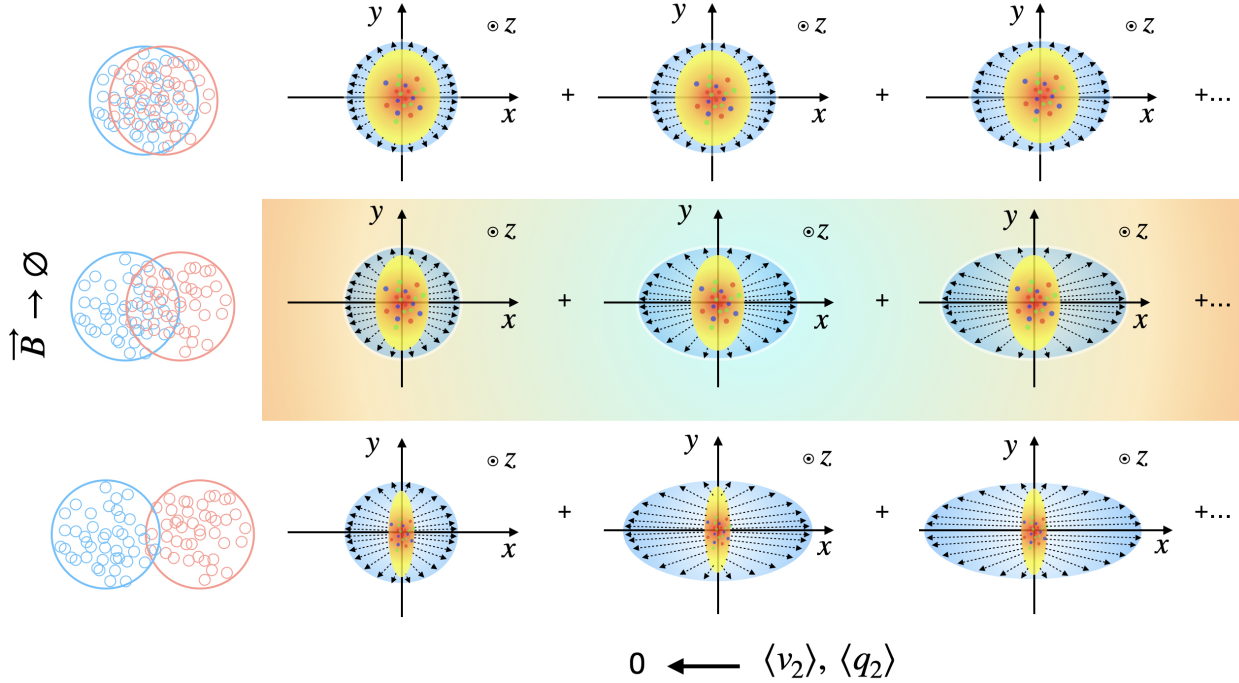


Figure 3.14: Schematic event-by-event shape of emission pattern.

Event Shape Selection (ESS) [77] aims to directly control the flow background by selecting events with isotropic emission patterns. To comprehend the observed CME flow background, we examine the schematic plot depicting the event shape of the emission pattern for a single heavy-ion collision, as shown in Fig. 3.14.

The emission patterns of second-order anisotropy have contributions from two primary sources. Plotted vertically is the initial source of the eccentricity of the overlapping nucleon geometry, which boosts the pressure gradients and pushes out particles from the QGP. This effect is correlated with long-range (pseudo-)rapidity ($\eta$) and is anticipated universally across hadronic species. Horizontally, the event-by-event fluctuation that arises from thermal fluctuations in a rapidly expanding system provides the second kind of source. These local fluctuations are short-ranged in (pseudo-)rapidity ($\eta$) and form a major contribution to event-by-event measurements such as the CME. It substantially affects the effectiveness of previous

selection methods that are solely dependent on "eccentricity", referred to as the event shape engineering [73] approach, and makes this method difficult for the CME detection [104].

To address the challenges, Event Shape Selection is developed to construct emission patterns that are sensitive to both sources. To correlate with the second-order anisotropy, the second-order event shape, $q_2$, is used to categorize collision events and map the CME observables to minimal flow. The early proposed event shape variable is the module of the second-order flow vector [104][127],

$$\overrightarrow{q_2} = \frac{1}{\sqrt{N}} \Big( \sum_{i=1}^{N} \cos 2\varphi_i, \sum_{i=1}^{N} \sin 2\varphi_i \Big). \tag{3.26}$$

Ideally, an event-shape variable derived from final-state particles accurately reflects the initial overlap region's eccentricity, so that the projection onto geometric spherical events ensures an average $v_2$ of zero for all particles, including primordial particles, resonances, or decay products. However, as illustrated in Fig. 3.14, particle emission patterns experience a substantial thermal fluctuation event by event, yielding minimal $v_2$ measurements despite finite eccentricity. Particularly, for the CME observation, we require non-central collisions where the magnetic field ($B$) from spectators can coexist with the QGP formed by participants. These non-central collisions by default own a nonzero eccentricity; while the event-by-event initial eccentricity fluctuation is typically small and less probable to deviate towards a spherical initial shape. The early methods that utilize $q_2$ to solely control over the eccentricity, which by logic construct from a different rapidity region (region B) from the particles of interest (POI) (region A) asserted to average out the fluctuation, typically present a weak correlation between the event shape $q_2\{B\}$ to the targeted kinematic region's $v_{2,POI}$. In practice, it leads to a sizable $v_{2,POI}$ measured at zero $q_2\{B\}$ isotropic events fluctuated from thermal expansion, and causing a wide, unmeasured $v_{2,POI}$ region towards zero. Thus, the extrapolation of $\Delta\gamma_{112}$ to zero flow introduces substantial statistical and systematic uncertainties, as reported at LHC [75][58].

Instead, controlling the emission pattern including both short- and long-ranged correla-

tions naturally requires building the event shape from the same kinematic region and directly using the POI [127]. Developing a feasible and effective ESS procedure is non-trivial. Prior studies have demonstrated that the event shape variable $q_2^2$ projects $v_2$ and $\Delta\gamma_{112}$ more linearly to the zero-flow limit. Based on the expansion,

$$q_2^2 = \frac{1}{N}\left[\left(\sum_{i=1}^{N}\sin 2\varphi_i\right)^2 + \left(\sum_{i=1}^{N}\cos 2\varphi_i\right)^2\right] = 1 + \frac{1}{N}\sum_{i\neq j}\cos[2(\varphi_i - \varphi_j)],$$

we estimate the event average of $q_2^2$ to be $\langle q_2^2\rangle \approx 1 + Nv_2^2\{2\}$, where $v_2\{2\}$ is the elliptic flow from two-particle correlations free from nonflow effects. The connection between the event shape variable and the elliptic flow variable is clearly inherited, along with the normalization correction. To the first-order correction, we define $q_2^2$ as

$$q_2^2 = \frac{\left(\sum_{i=1}^{N}\sin 2\varphi_i\right)^2 + \left(\sum_{i=1}^{N}\cos 2\varphi_i\right)^2}{N(1 + Nv_2^2\{2\})}. \tag{3.27}$$

Note that $N$ varies from event to event, whereas $v_2\{2\}$ is a static constant averaged over all events. In practice, the ensemble-averaged $v_2$ can be a good proxy.

Since the CME flow background comes from pair production mechanisms, the pair event shape is particularly sensitive to both primordial and pair patterns. For instance, to the background arising from flowing resonances, the $v_2$ and the corresponding $q_2$ of the parent resonances should be more relevant than those of the kindred decay daughters. Accordingly, we use the pair azimuthal angle, $\varphi^p$, from the momentum sum for each pair of particles, regardless of the existence of a genuine parent, to define the pair $q_2^2$:

$$q_{2,\text{pair}}^2 = \frac{\left(\sum_{i=1}^{N_{\text{pair}}}\sin 2\varphi_i^p\right)^2 + \left(\sum_{i=1}^{N_{\text{pair}}}\cos 2\varphi_i^p\right)^2}{N_{\text{pair}}(1 + N_{\text{pair}}v_{2,\text{pair}}^2\{2\})}. \tag{3.28}$$

Note that the $v_{2,\text{pair}}^2\{2\}$ in practice can use the $v_{2,\text{pair}} = \langle\cos(2\varphi^p - 2\Psi_{\text{RP}})\rangle$ in Eq. (3.11) as proxy. The correction term in the normalization is crucial given that $N_{\text{pair}}$ is basically on the order of $N^2/2$.

With event shape selection built upon POI, now we return to the very first two examples of simple resonance pictures in Section 3.1, we observe below:

a) In case of "hidden" anisotropy: $q_2^2 = 0$, $q_{2,\text{pair}}^2 = 1$.

b) In case of "explicit" anisotropy: $q_2^2 = 1$, $q_{2,\text{pair}}^2 = 1$.

Hence, we learned that utilizing the single $q_2^2$ is insufficient and may be blind to some background physics, potentially resulting in residual background. Meanwhile, the pair $q^2$ proves more sensitive to the emission background.

In ESS, we categorize events into different subsets based on $q_2^2$. Then, $\Delta\gamma_{112}$ and elliptic flow variable $v_2$ are computed for each data subset. Finally, the mapping of $\Delta\gamma_{112}$ to the elliptic flow variable is plotted to linearly project towards the zero-flow limit.
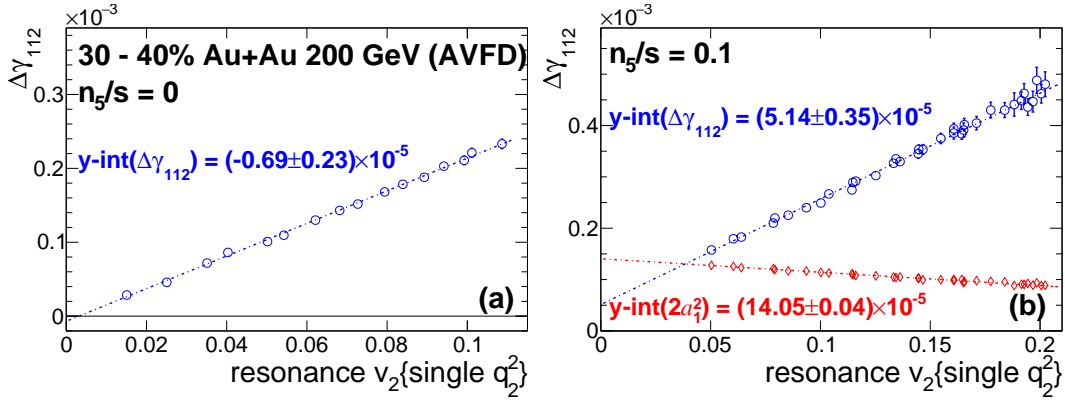


Figure 3.15: AVFD simulation for Event Shape Selection with resonance $v_2$ used for (a) pure background and (b) moderate CME signal.

In Section 3.1, we have discussed the choice of the elliptic flow variable. Now, we can perform an assessment on the event shape approaches by first examining the resonance $v_2^{\text{res}}$ for the flow background subtraction. We have learned that $v_2^{\text{res}}$ can reflect the true background in the absence of the CME, but is highly influenced by the CME signal in its presence. The AVFD simulations are presented in Fig. 3.15 for $\Delta\gamma_{112}$ and $v_2^{\text{res}}$ calculated for $\pi$-$\pi$ correlations with respect to the true reaction plane in 30–40% Au+Au collisions at 200 GeV, and each sub-event is categorized with single $q_2^2$. In scenarios of pure background, $n_5/s = 0$ (a), the intercept extrapolated to zero-flow background limit is reduced to below zero. In the second panel, with a moderate CME input, $n_5/s = 0.1$ (b), the true CME signal, $2a_1^2$, under

event shape mapping is shown in red, while the $y$-intercept obtained from linear fitting of our observable $\Delta\gamma^{112}$ demonstrates a substantial over-subtraction of the CME signal. This result is recalled to the Eq. (3.15).

For the Event Shape Selection, we would use the elliptic flow not severely affected by the CME. From Section 3.1, we observed that both single and pair $v_2$ are nearly constant under the CME, thus, we explore the following ESS combinations built upon single particles or particle pairs:
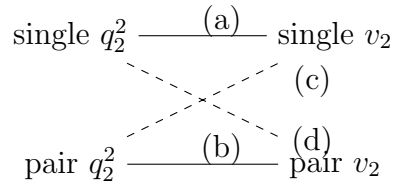


Figure 3.16: The four combinations in Event Shape Selection.

Among the four ESS recipes, the two unmixed ESS combinations, with (a) single $q_2^2$ and single $v_2$ and with (b) pair $q_2^2$ and pair $v_2$, inherent a correlation between the event shape variable and the elliptic flow variable building from the same kindred particles, as indicated by Eq. (3.27). This self-correlation of $q_2$-$v_2$ can bias the projection to the zero-flow limit, leading to a residual background. Consequently, these two unmixed ESS recipes (a) and (b) would under-subtract the background. In contrast, the mixed recipes, with (c) pair $q_2^2$ and single $v_2$ and with (d) single $q_2^2$ and pair $v_2$, have more independent relation between the event shape variable and the elliptic flow variable. Thus, they better suppress such residual backgrounds. However, the pair $v_2$ includes a small CME contribution (Eq. (3.17)), analogous to the case using $v_2^{\text{res}}$, which may lead to certain over-subtraction of the signal in mapping to $\Delta\gamma_{112}$. Hence, the optimal ESS recipe is proposed to be (c), which utilizes pair $q_2^2$ as the event shape variable to capture the flowing pair production background, while employing single $v_2$ as the elliptic flow variable.

The efficiency of four ESS combinations can be tested with the AVFD model, which
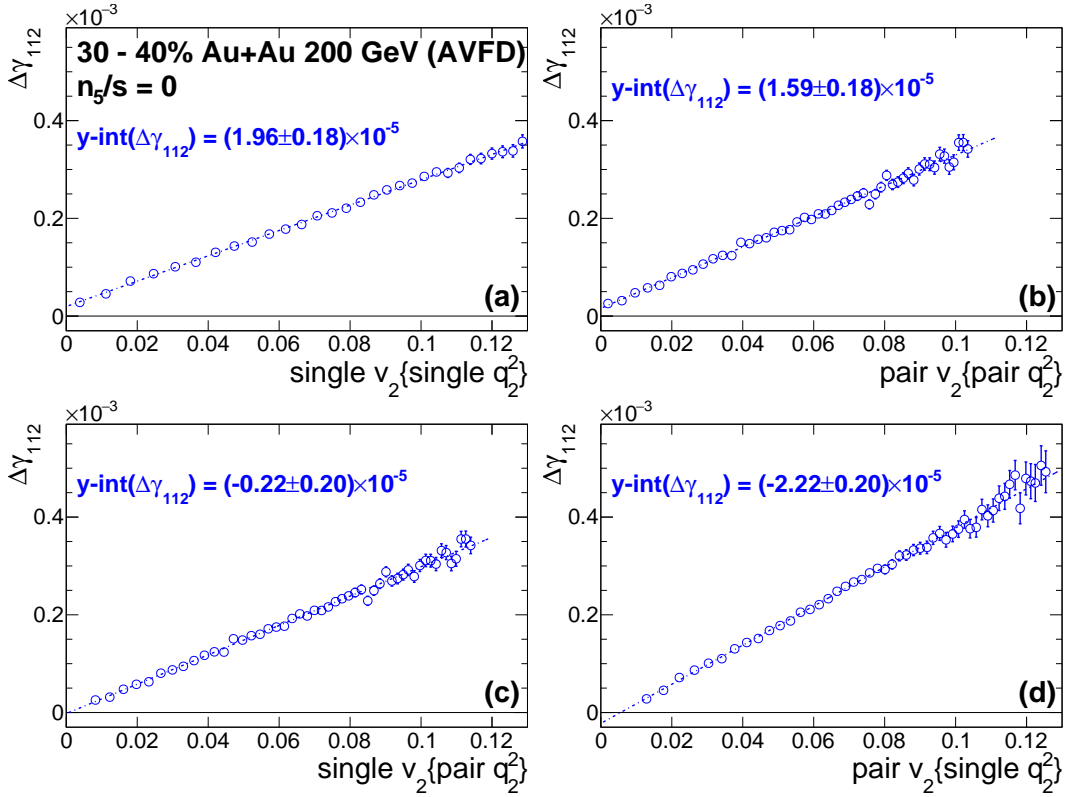
Figure 3.17: AVFD simulations of Event Shape Selection for the pure-background case.

allows for background control and adjustment of the CME strength.

In the scenario of pure background ($n_5/s = 0$), Fig. 3.17 shows the $\Delta\gamma_{112}$ mapping against single or pair $v_2$ measured at the corresponding single or pair $q_2^2$, in the application of the four ESS combinations (a) through (d). For 30–40% Au+Au collisions at 200 GeV, the $y$-intercepts from linear fits presents $\Delta\gamma_{112}$ after flow background reduction. Built with the particle of interest, event shape with $q_2^2$ can allow for a close-to-zero projection, which is linear and reliable.

The first two panels, representing unmixed combinations (a) and (b), demonstrate an approximate eight-fold suppression of background in comparison to the ensemble-averaged $\langle\Delta\gamma_{112}\rangle$. The finite intercepts of single $v_2\{$single $q_2^2\}$ and pair $v_2\{$pair $q_2^2\}$ reflect the anticipated residual background from self-correlation. The second row shows mixed combinations, where the optimal solution (c) single $v_2\{$pair $q_2^2\}$ aligns with zero, while pair $v_2\{$single $q_2^2\}$
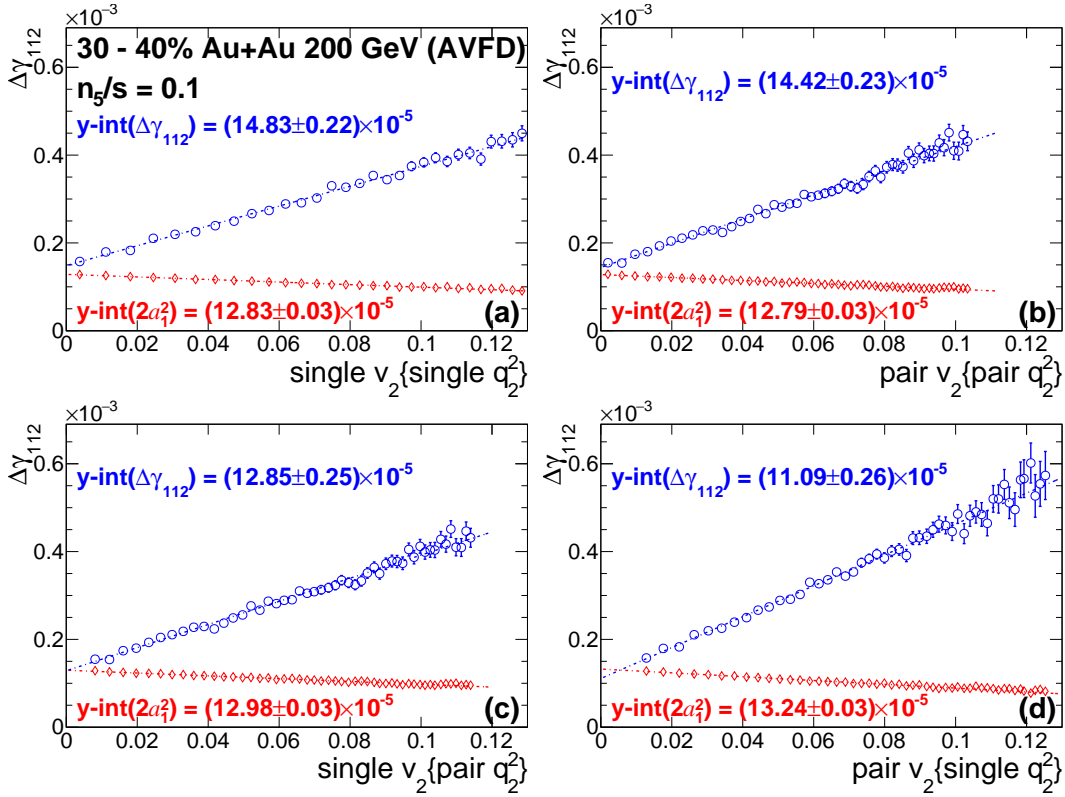
Figure 3.18: AVFD simulations of Event Shape Selection for the moderate CME input $(n_5/s = 0.1)$.

over-subtracts the background, as expected. Therefore, for the pure background simulations, an ordering of intercept by $(a) > (b) > (c) > (d)$ is observed, with the optimal solution accurately removing the flow background.

The Event Shape selection is further investigated by introducing the CME signal in AVFD at the moderate $(n_5/s = 0.1)$ and high level $(n_5/s = 0.2)$. Similar conclusions and intercept-ordering are observed.

Fig. 3.18 presents the moderate CME signal in the application of the ESS approaches. In contrast to the observed $\Delta\gamma_{112}$ (blue circle), the true signal $2a_1^2$ (red diamond) is included and project to zero $v_2$. Their $y$-intercepts from linear subtraction can be directly compared in the plot, reflecting the effectiveness of the four ESS recipes in revealing the true CME signal. To the four ESS outcomes, the $y$-intercepts of $\Delta\gamma_{112}$ obtained from (a) single $v_2\{$single $q_2^2\}$
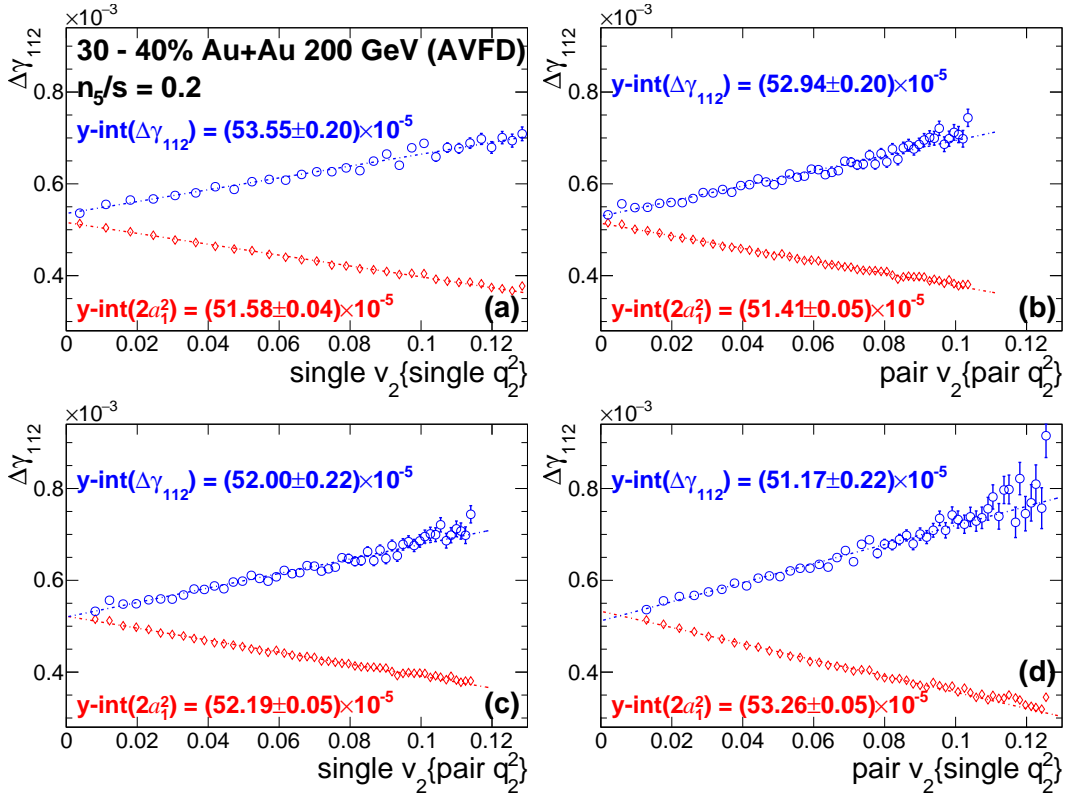
Figure 3.19: AVFD simulations of Event Shape Selection for a strong CME input ($n_5/s = 0.2$).

and (b) pair $v_2\{$pair $q_2^2\}$ clearly under-subtracts the actual background, which reflects the residual background from a self-correlation. While using (d) pair $v_2\{$single $q_2^2\}$ overestimates the background, leading to the over-subtraction. In contrast, the optimal ESS approach using single $v_2\{$pair $q_2^2\}$ appear to recover the true signal within the uncertainties robustly for different signal strengths.

Fig. 3.19 further investigates the ESS approaches with a strong CME input. The same conclusions are observed, with the unmixed recipes underestimating the background and the mixed recipes further suppressing the background. ESS (c) is again found to successfully reconstruct the true CME signal. Thus, this method holds robust at pure-background, moderate CME, or high CME input, and is validated as the optimal solution.

In addition, in the extrapolation to the zero-flow limit, the true signal $a_1^2$ is found to

63

increase, which comes from the aspect of non-interdependent flow discussed in Section 3.2. To restore the CME contribution, $\Delta\gamma^{\mathrm{CME}}$, to the ensemble average observable, the $y$-intercept of $\Delta\gamma_{112}$ needs to be scaled with a corresponding factor. It is suggested by $\langle a_1 \rangle = a_1|_{v_2=0} \cdot (1 - \langle v_2 \rangle)$, that

$$\Delta\gamma^{\mathrm{CME}} = (1 - \langle v_2 \rangle)^2 \times \text{Intercept}. \tag{3.29}$$

Here, $v_2$ is represented by the single-particle $v_2$, typically on the order of 5%. Higher-order effects could exist even without considering non-interdependent effects. This reestablishes the ensemble average of $\Delta\gamma^{\mathrm{CME}}$ to the first order.

Besides the AVFD model, various event generators have been investigated to study background contributions to the $\gamma_{112}$ correlator. Notably, models like PYTHIA [96], HIJING [128][129], MEVSIM [130], and UrQMD [131] substantially underestimate the background [52][60]. While the AMPT model [109][110] can partially reproduce the background contributions comparable to experimental measurements [132], but fails to describe some such as the local charge conservation background. Even with the ESS (a) application using single $v_2$ and single $q_2^2$ can effectively eliminate all backgrounds generated by AMPT [133]. The outcomes of our four ESS recipes from the AMPT simulations exhibit the same ordering as observed in EBE-AVFD, with the tendency to over-subtract the AMPT background, as shown in Fig. 3.20.

EBE-AVFD remains the most realistic model for CME simulations. Since it develops from the hydrodynamic calculation, all the known background mechanisms including flowing resonance decays, TMC, and LCC are fully equipped in the model. We also investigated augmenting the strength of the LCC effect by half in the EBE-AVFD simulations. The conclusions drawn above remained unchanged.

For a complete understanding of the event shape approaches, we also compute the method utilizing $q^2$ from a different kinematic region B, which targets the control of eccentricity alone. As demonstrated in Fig. 3.21, the event shape variable exclusive of POI, $q_{2,\mathrm{B}}$, are constructed using single particles with $1 < |y| < 2$, while POI are within $|y| < 1$. In 30–40%
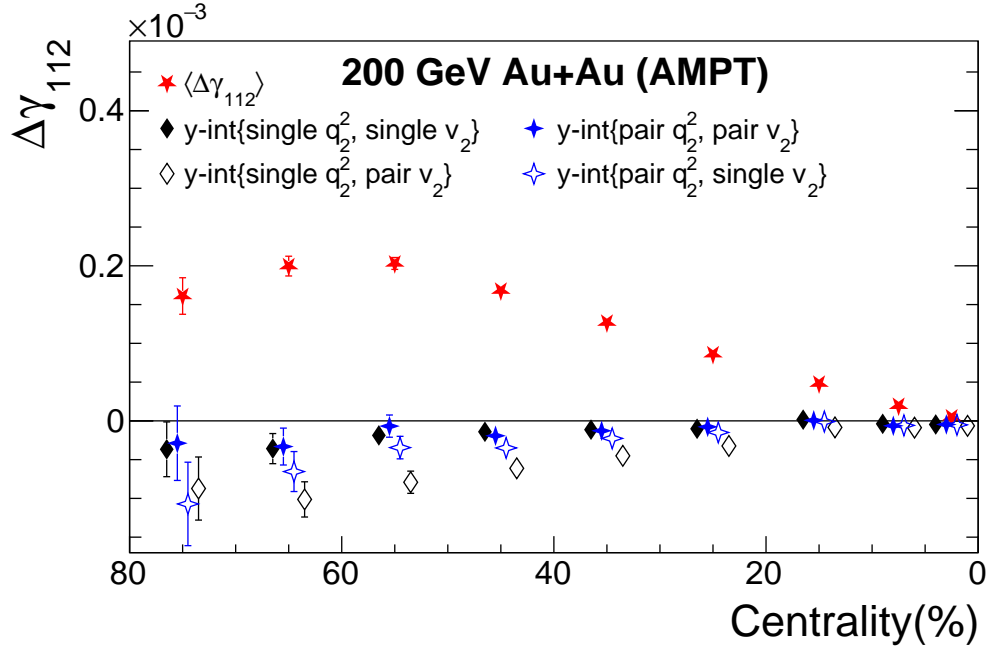
Figure 3.20: AMPT simulations of Event Shape Selection in Au+Au at 200 GeV.

Au+Au collisions at 200 GeV, the first panel shows the weak correlation between the $q_{2,\mathrm{B}}$ with single $v_2$: the latter remains sizable at zero $q_{2,\mathrm{B}}$, in contrast to the $q_2^2$ involving POI. Panel (b)–(d) in Fig. 3.21 present $\Delta\gamma_{112}$ as a function of single $v_2$ categorized by this $q_{2,\mathrm{B}}$ in the different CME signal scenarios, at $n_5/s = 0$, $0.1$, and $0.2$, respectively. The $y$-intercepts obtained with linear fits (solid lines) indicate a certain degree of over-subtraction of the background. The extensive blank regions at low $v_2$ considerably amplify the statistical uncertainties of the $y$-intercepts, leading to a tripling of the uncertainties compared with using event shape variables involving POI. Moreover, second-order polynomial fits (dashes lines) demonstrate the systematic uncertainties due to long extrapolations, where the variations of the $y$-intercepts exceed the statistical uncertainties. Conversely, employing POI for the event shape variable renders significantly more reliable results, in terms of both statistical accuracy and systematic consistency.

In summary of this chapter, we have examined the origin of the CME flow background and presented the newly developed method, Event Shape Selection, which is hitherto the
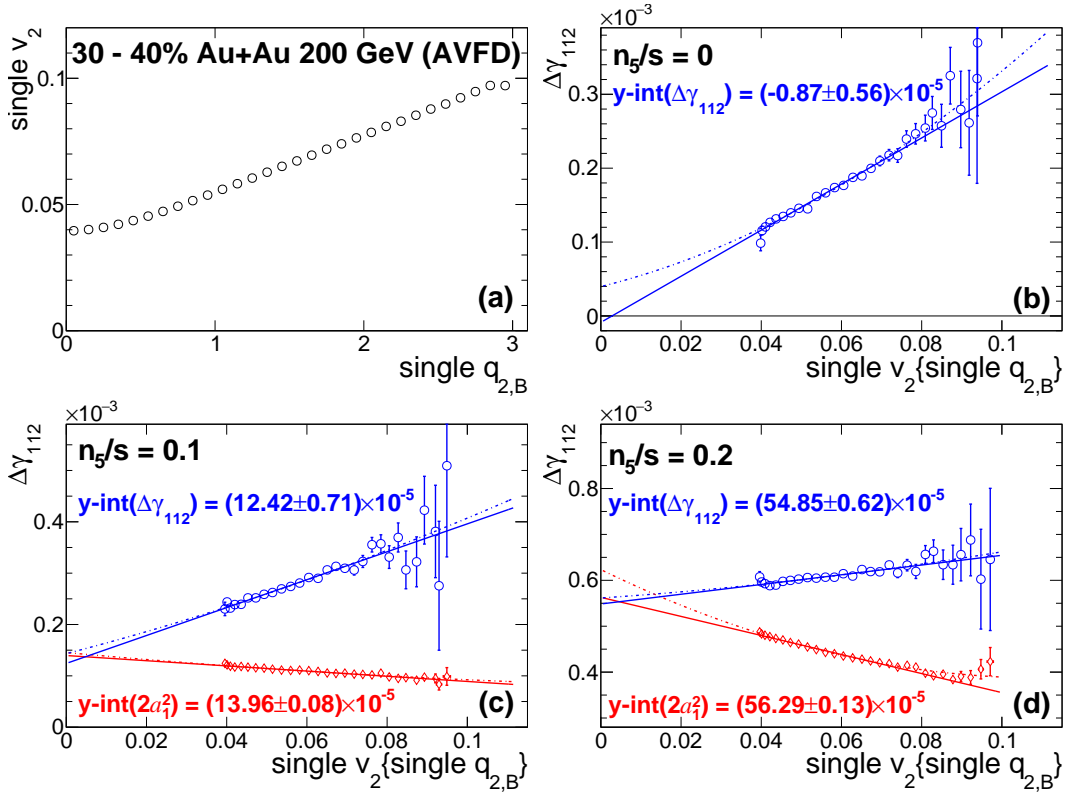
Figure 3.21: AVFD simulations utilizing the event shape variable independent of the POI rapidity region.

most robust method for directly removing the flow-related background. We will perform this ESS analysis on STAR data. In addition, the advantage of the EPD subsystem at STAR allows the construction of the high-resolution spectator plane to suppress the nonflow background and construct the $B$-field direction. We aim to search for the CME in $\Delta\gamma_{112}$ with all known backgrounds suppressed in the RHIC BES-II data.

$$\Delta\gamma_{112} = \Delta\gamma^{\mathrm{CME}} + \cancel{\Delta\gamma_{BG}^{\mathrm{flow}}} + \cancel{\Delta\gamma_{BG}^{\mathrm{nonflow}}}. \tag{3.30}$$

# CHAPTER 4

# CME measurements at STAR

The Chiral Magnetic Effect (CME) creates a charge separation along the magnetic field direction for quarks at chirality imbalance. The STAR Beam Energy Scan-II provides high-statistic data of Au+Au collisions for detecting the CME, where the magnetic field effects could potentially be enhanced at lower energies. Charged hadrons from STAR Time Projection Chamber (TPC) are selected as particles of interest (POI) with the rejection of (anti)proton to avoid transport effect. The Event Plane Detector (EPD) at STAR allows the reconstruction of the $B$ field direction with a high-resolution spectator-enriched plane, which at the same time suppresses the nonflow background effects. Additionally, detector corrections and PID cut efficiency corrections are calculated and applied. We also discuss the evaluation of systematic uncertainty in this measurement of BES-II data.

## 4.1 BES-II datasets

The datasets used in this work are Au+Au collisions at RHIC systematically acquired during the Beam Energy Scan phase II (BES-II) program launched from 2018 to 2021. Table 4.1 provides a comprehensive overview of the production parameters, including STAR detector triggers, the trigger tags, the data library, and minimum bias (MB) trigger ID used for each collision energy, specifically, at $\sqrt{s_{NN}} = 27$, 19.6, 17.3, 14.6, 11.5, 9.2, and 7.7 GeV. We primarily concentrate on the "st_physics" data stream and the minimum bias trigger events, which are critical for collision dynamics. The last column of the table displays the total number of events collected after applying all event-level cuts used in this analysis. These

Table 4.1: BES-II Au+Au trigger and production list for this work.

| Energy | Trigger Name | Tag | Lib | Trigger ID | Total Events |
|---|---|---|---|---|---|
| 27 GeV | 27GeV_production_2018 | P19ib | SL19b | 610001,610011,610021 610031,610041,610051 | 513 M |
| 19.6 GeV | production_19GeV_2019 | P23id | SL23d | 640001,640011,640021 640031,640041,640051 | 453 M |
| 17.3 GeV | production_17p3GeV_2021 | P23id | SL23d | 870010 | 202 M |
| 14.6 GeV | production_14p5GeV_2019 | P23id | SL21d | 650000 | 234 M |
| 11.5 GeV | production_11p5GeV_2020 | P23ia | SL23a | 710000,710010,710020 | 175 M |
| 9.2 GeV | production_9p2GeV_2020 | P23ia | SL23a | 780010 | 5 M |
| | production_9p2GeV_2020b | P23ia | SL23a | 780020 | 20 M |
| | production_9p2GeV_2020c | P23ia | SL23a | 780020 | 84 M |
| 7.7 GeV | production_7p7GeV_2021 | P22ib | SL22b | 810010,810020 810030,810040 | 60 M |

cuts are based on the selection of the primary collision vertex, and by the exclusion of run periods with bad quality. Further details on both processes are provided in the following sections.

## 4.2 Event Selection and Quality Assurance

### 4.2.1 Event Selection

For all the datasets mentioned above, the uniform event-level cuts are maintained across different beam energies to ensure a reliable systematic comparison. In search of the CME,
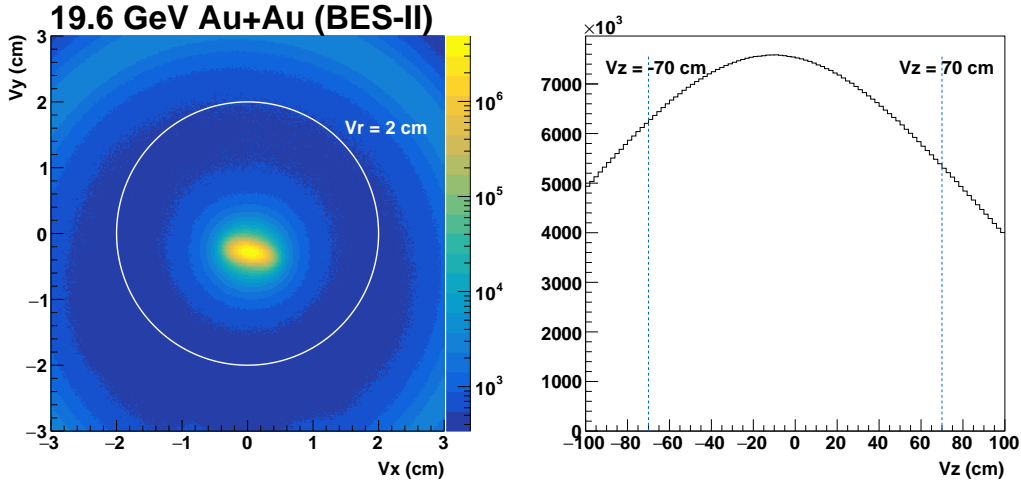
Figure 4.1: Event vertex distribution in Au+Au at 19.6 GeV (BES-II).

we focus on using the collision events detected by the STAR TPC. The event level cuts are listed in the following.

- Minimum bias (MB) trigger

- Primary vertex along the beam direction $|V_z| \leq 70$ cm.

- Primary vertex perpendicular to the beam within $V_r \leq 2$ cm.

- The STAR official bad runs are rejected, which are provided by the STAR QA board.

- The pile-up events are rejected, which are provided by the STAR centrality definition group.

- Additional bad runs are excluded based on the quality assurance (QA) conducted by the analyzer for this work with a higher standard.

Around 80% of the raw collision events have the MB trigger. Furthermore, the primary vertex position of an event is required to have the longitudinal position at the $z$-axis ($V_z$) within $(-70, 70)$ cm, and a transverse location ($V_r$) within of $< 2$ cm. This vertex selection ensures an excellent acceptance for all charged hadrons at positive or negative rapidity
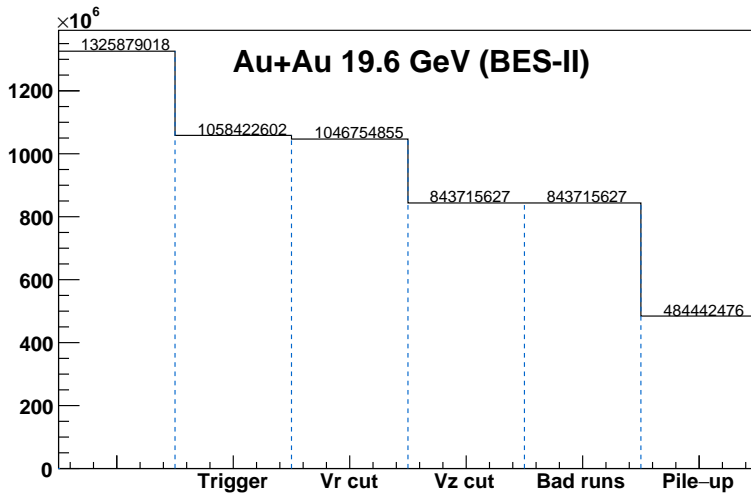
Figure 4.2: Number of events after sequential cuts in Au+Au at 19.6 GeV (BES-II).

recorded by the TPC. The example of the $V_z$ and $V_r$ distribution in Au+Au collisions at 19.6 GeV is shown in Fig. 4.1. In the left panel, the beam pipe (the shaded ring) is located around 3 cm away from the center. By implementing the $V_r$ cut, we retain 99% of the events. Although the current STAR TPC can operate along the entire longitudinal range of $V_z$ up to ±150 cm, we prioritize analyzing collisions close to the center of the TPC. This focus is due to the detector inefficiency at the edges of the TPC, where the detection of tracks at positive and negative rapidities can become uneven. The implementation of the $V_z$ cut retains approximately 80% of high-quality events, optimizing the analysis for the CME search.

Then, the bad runs of each energy at BES-II are identified and excluded by the Quality Assurance (QA) procedure. In addition to the official list of bad runs provided by the STAR QA board (as discussed in Section 2.3.2), we have conducted a thorough QA with variables crucial to our analysis in search of the Chiral Magnetic Effect. The detailed examination will be discussed in the following section. Several additional bad runs thus identified are excluded from the analyses. After that, we reject the pile-up events, identified with outliers in the matching multiplicity between the TPC and the fast TOF detector. Such information

is provided by STAR's standard centrality definition, as discussed in Section 2.3.2. This procedure effectively keeps about 50% of good events. In the last step, the centrality ranges of 0–80% will be selected for this work.

### 4.2.2 Quality Assurance and bad run rejection

Table 4.2: QA variable list

| RefMult | nBTOFMatch | $V_z$ | $N_{\text{Track}}$ |
|---|---|---|---|
| dE/dx | $\langle \text{DCA} \rangle$ | $\langle \eta \rangle$ | $\langle p_T \rangle$ |
| $\langle \varphi \rangle$ | $Q_{1x}$ | $Q_{1y}$ | $Q_{2x}$ |
| $Q_{2y}$ | EPD east hits | EPD west hits | EPD $Q_{1x}$ |
| EPD $Q_{1y}$ | EPD $Q_{2x}$ | EPD $Q_{2y}$ | |

Additional bad runs for this work are excluded based on our Quality Assurance (QA) processes, which incorporate the specific event-level cuts of radial vertex $V_r$ and axial vertex $V_z$, as specified above.

The event- and track-level QA variables are checked for each run period (referred to Table. 4.2). This requires the assessment of the TPC performance, starting with Reference Multiplicity (RefMult) per run, defined as the total number of charged hadrons within $|\eta| <$ 0.5. Then, the number of barrel TOF matches (nBTOFMatch) per run is checked, which targets the potential additional pile-up events. The primary vertex position along the $z$-axis ($V_z$) per run, and total track count per run ($N_{\text{Track}}$) are checked for the event performance.

On the particle track level, the average energy loss per unit length (dE/dx) per particle per run is accessed for particle identification purposes. The average Distance of the Closest Approach ($\langle \text{DCA} \rangle$) per track per run is also a critical parameter. Then, the mean pseudo-rapidity ($\langle \eta \rangle$), average transverse momentum ($\langle p_T \rangle$), and mean azimuthal angle ($\langle \varphi \rangle$) per particle per run represent typical kinematics that need to be accessed.

In using the Event Shape method, the constructed flow vectors associated with the particles of interest require the evaluation of its $x$ $(y)$ components such as $Q_{1x}$, $Q_{1y}$, $Q_{2x}$, and $Q_{2y}$, where $\vec{Q}$ is defined in Eq. (3.26) for Fourier harmonics of $n = 1,\ 2$.

To use the Spectator Plane (SP) reconstructed from the EPD, we also estimate the EPD performance by checking the hits on the east and west disks of the Event Plane Detector (EPD) per run. In addition, the reconstructed SP requires the assessment of the EPD event flow vectors $(Q_{1x}$, $Q_{1y}$, $Q_{2x}$, $Q_{2y})$.

For the above QA variables, we employ the run-by-run code package provided by the STAR QA group and adhere to their standard procedures. The runs are first divided into different segments based on the Kernseg algorithm. The criteria to reject a bad run are defined as the deviations exceeding $> 5\sigma$ locally and/or $> 20\sigma$ globally from the mean value per local segment. The details on these criteria for each Au+Au run in the BES-II will be discussed below.

### 4.2.2.1 QA of Au+Au Collisions at $\sqrt{s_{NN}} = 27$ GeV

Data of Au+Au collisions at 27 GeV from the BES-II were collected in 2018. The production of "27GeV_production_2018" with Tag "P19ib" and the stream "st_physics" are used. The additional QA is conducted on a run-by-run basis following the QA variables listed in Table 4.2. The analysis period is segmented into several stable running intervals defined by breakpoints at 19141047, 19144036, 19146026, 19155057, and 19168040. Within each segment, we allowed a $y$-range deviation of up to $20\sigma$ for categorizing runs as acceptable.

Our QA process identifies 23 additional bad runs out of the total 715: 19131026, 19131042, 19131048, 19131049, 19134008, 19134009, 19134024, 19134025, 19134029, 19134030, 19134050, 19135001, 19135012, 19135039, 19135040, 19136005, 19136014, 19137020, 19156004, 19156005, 19156006, 19156033, 19156047.

After the implementation of event-level cuts, we collected 513 million events for Au+Au

at 27 GeV.

## 4.2.2.2 QA of Au+Au Collisions at $\sqrt{s_{NN}} = 19.6$ GeV

Data of Au+Au collisions at 19.6 GeV from the BES-II were taken in 2019. The production of "production_19GeV_2019" with Tag "P23id" and the stream "st_physics" are used. The additional QA based on variables listed in Table. 4.2 is presented in Fig. 4.3. The different QA variables per run are plotted against the run numbers (run ID), with identified outliers (red).
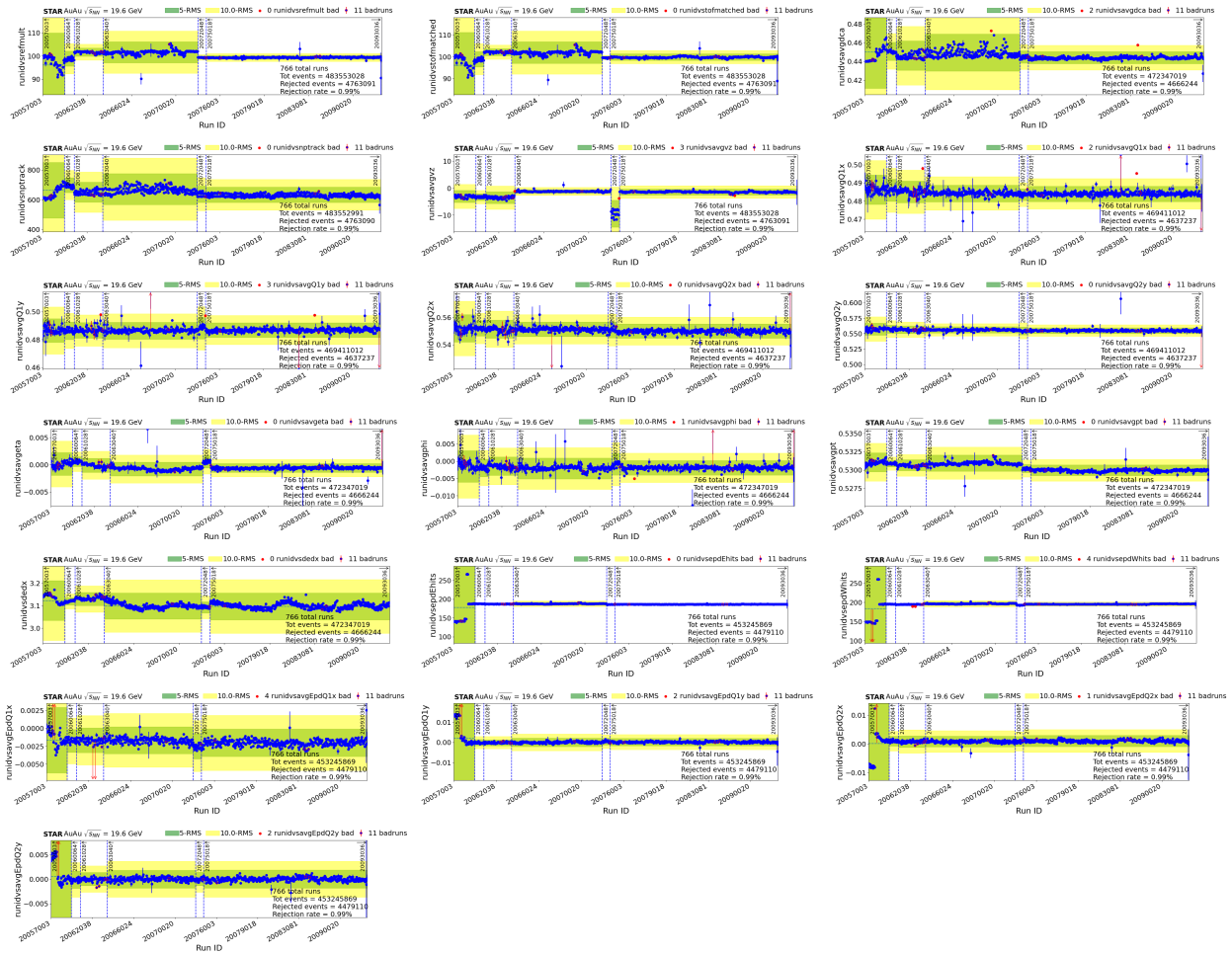


Figure 4.3: Quality Assurance plots for Au+Au at 19.6 GeV (run 19).

The run is divided into several stable run periods at the breakpoints: 20060064, 20061028,

20063040, 20072048, 20075018, as shown in Fig. 4.3. We identified 11 additional bad runs out of the total 767: 20057033, 20057043, 20062051, 20063002, 20063028, 20063037, 20069055, 20073027, 20076005, 20085003, 20085018. After the event level cut, we collect 453 M events for the Au+Au at 19.6 GeV.

### 4.2.2.3   QA of Au+Au Collisions at $\sqrt{s_{NN}} = 17.3$ GeV

The data of Au+Au collisions at 17.3 GeV from the BES-II were taken in 2021, and the production name of "production_17p3GeV_2021" with Tag "P23id" and the stream "st_physics" are used. Similar to above, we conduct additional run-by-run QA based on variables listed in Table. 4.2.

Figure A.1 (in Appendix) presents the results for Au+Au at 17.3 GeV. The data are found to be divided into several stable run periods at the breakpoints: 22148019, 22150018, and 22155012. We successfully identified 12 additional bad runs out of the total 234: 22145028, 22149004, 22149016, 22152038, 22155004, 22155006, 22155007, 22155044, 22156028, 22156034, 22157021, 22158019. After the event level cut, we collect 202 M events for this run of Au+Au at 17.3 GeV.

### 4.2.2.4   QA of Au+Au Collisions at $\sqrt{s_{NN}} = 14.6$ GeV

The data of Au+Au collisions at 14.6 GeV from the BES-II were taken in 2019. Here, the production of "production_14p5GeV_2019" with Tag "P23id" and the stream "st_physics" are used. The additional run-by-run QA is based on variables listed in Table. 4.2 and results are presented in Fig. A.2 (in Appendix). Similarly, the data are divided into several stable run periods at the breakpoints: 20099035, 20102055, 20105035, 20110002, 20117058, 20122038, 20137044, and 20138025. We identified 22 additional bad runs out of the total 925: 20094048, 20099043, 20111029, 20113029, 20113060, 20113061, 20113062, 20113064, 20113079, 20117042, 20119017, 20123007, 20128020, 20135005, 20135006, 20138004, 20140001,

20140002, 20140003, 20140004, 20140005, 20152036. After the event level cut, we collect 234 M events for this run of Au+Au at 14.6 GeV.

### 4.2.2.5 QA of Au+Au Collisions at $\sqrt{s_{NN}} = 11.5$ GeV

The data of Au+Au collisions at 11.5 GeV from the BES-II were taken at the end of 2019 and the first three months of 2020. Here, the production name of "production_11p5GeV_2020" with Tag "P23ia" and the stream "st_physics" are used. The total run is split into two periods. The run number 20342002 – 20365041 are for data collected at the end of 2019, and run 21001001 – 21055017 for those at the beginning of 2020. The additional QA is conducted correspondingly, based on variables listed in Table. 4.2. Figures A.3 and A.4 (in Appendix) list the QA details for 11.5 GeV.

For 20365001 – 20365041, the run is divided into several stable run periods at the breakpoints: 20346051, 20354003, 20355023. We find 19 additional bad runs out of the total 593: 20342006, 20344020, 20344046, 20345023, 20352014, 20352048, 20355045, 20356006, 20356009, 20356011, 20356026, 20361021, 20361022, 20361024, 20361025, 20362032, 20365019, 20365023, 20365031.

For 21001001 – 21027007, the run is divided into several stable run periods at the breakpoints: 21003044, 21005025, 21008042, 21012013 21014022, 21019031, 21020007, 21023031, 21041027, 21042022, 21045029, 21047029, 21051035, 21054017. We find 19 additional bad runs out of the total 1291: 21001022, 21004028, 21006026, 21008001, 21008034, 21013020, 21019019, 21021014, 21023026, 21024027, 21050064, 21051004, 21051017, 21052036, 21053025, 21053026, 21053027, 21053028, 21053063.

After the event level cut, we collect 175 M events for this run of Au+Au at 11.5 GeV.

### 4.2.2.6   QA of Au+Au Collisions at $\sqrt{s_{NN}} = 9.2$ GeV

The data of Au+Au collisions at 9.2 GeV from the BES-II were taken in three periods in 2020, and the additional QA was conducted separately based on Table. 4.2. Fig. A.5, Fig. A.6, and Fig. A.7 (in Appendix) present the QA details.

The short period of 21030030 – 21041013 is considered as one whole run period. No bad run is identified.

For 21055032 - 21080027, the run is divided into two stable run periods at the breakpoint 21073043. We found 14 additional bad runs out of the total 581: 21055032, 21056002, 21056026, 21057025, 21057027, 21057028, 21058025, 21061001, 21061002, 21064048, 21070028, 21073042, 21078004, 21080019.

For 21169035 - 21245010, the run is divided into several stable run periods at the breakpoints: 21172033, 21190054, 21198021, 21203018, 21210013, 21225044, 21227004, 21229042. We found 64 additional bad runs out of the total 1352: 21169039, 21170018, 21171031, 21171032, 21171033, 21172032, 21174049, 21174050, 21176020, 21177019, 21177020, 21177021, 21177022, 21179001, 21179018, 21179026, 21181033, 21189039, 21189040, 21190053, 21192018, 21192020, 21203017, 21205011, 21205012, 21205020, 21205023, 21206003, 21206004, 21206005, 21206007, 21206008, 21206016, 21206030, 21208027, 21210009, 21211004, 21211009, 21213004, 21213005, 21213006, 21217003, 21217010, 21218001, 21218002, 21218003, 21218004, 21218005, 21218006, 21218007, 21218014, 21222026, 21224016, 21224017, 21225035, 21225042, 21225043, 21227021, 21235015, 21235035, 21237021, 21237022, 21237023, 21241015,

After the event level cut, we collect 107 M events for this run of Au+Au at 9.2 GeV.

### 4.2.2.7   QA of Au+Au Collisions at $\sqrt{s_{NN}} = 7.7$ GeV

The data of Au+Au collisions at 7.7 GeV from the BES-II were taken in 2021, while the production of "production_7p7GeV_2021" with Tag "P22ib" and the stream "st_physics" are used here. The additional run-by-run QA are shown in Fig. A.8.

The run is divided into several stable run periods at the breakpoints: 22038019, 22044021, 22046001, 22048041, 22050036, 22054045, 22063015, 22072002, 22078037, 22082012, 22083011, 22088024, 22105006, 22118060. We found 44 additional bad runs out of the total 2545: 22032014, 22033009, 22033010, 22033012, 22033013, 22033014, 22033017, 22033018, 22033028, 22033031, 22033033, 22033034, 22033036, 22033037, 22033038, 22033039, 22033040, 22033041, 22033042, 22033043, 22035008, 22038026, 22039016, 22040030, 22044006, 22046005, 22064013, 22068039, 22068040, 22081026, 22083027, 22094045, 22097037, 22106017, 22117037, 22117038, 22117039, 22117040, 22117041, 22117042, 22117043, 22117044, 22118059, 22120031.

After the event level cut, we collect 60 M events for this run of Au+Au at 7.7 GeV.

## 4.3   PID selection

### 4.3.1   Track Level Cuts

In search of the CME, we focus on all hadrons, excluding protons, as our particles of interest (POI). These hadrons are identified by the Time Projection Chamber (TPC), which measures the transverse momenta of charged particles using their trajectory curvatures under a constant magnetic field of 0.5 T.

The following cuts are required for general track quality assurance:

- Primary track that extrapolates to the vertex

- DCA < 3 cm

- Transverse momentum $p_T > 0.2$ GeV/c

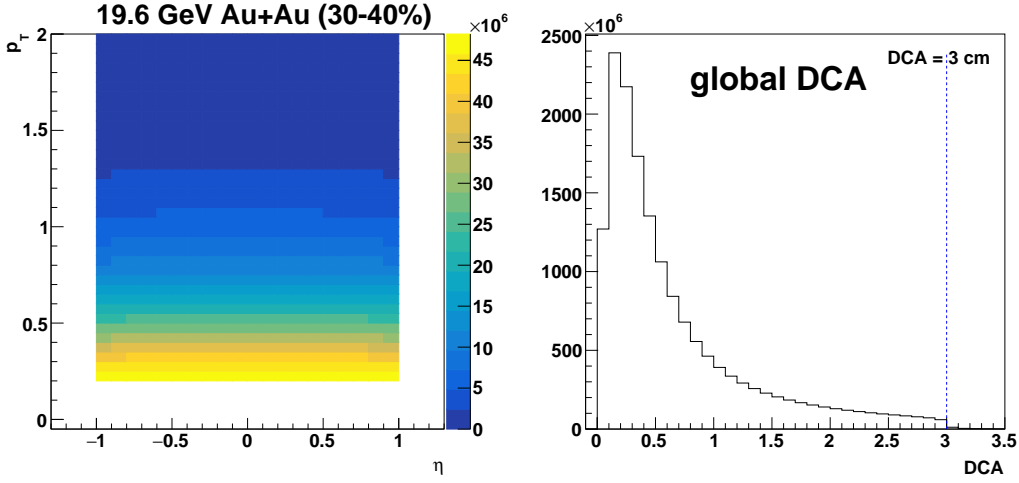- Total momentum $p < 1.4$ GeV/c (at 7.7 GeV, it is tightened to $p < 1.3$ GeV/c)

- Pseudorapidity $|\eta| < 1$

- Number of fitting hits, nHitsFit > 15.

Figure 4.4: (Left) $p_T$ vs $\eta$ and (right) the global DCA distribution in 30–40% centrality Au+Au at 19.6 GeV (BES-II).

- Rejection of (anti-)proton ($p$ and $\bar{p}$)

As shown in Fig. 4.4, the $p_T$ vs $\eta$ distribution suggests the cut keeps 98% of tracks, and after the global DCA cut we retain most of the particles.

Early studies found that protons are largely impacted by the transported-proton effect, which presents a different flow background coupling than the produced quarks. Thus, to avoid the transported protons, we reject the possible $p$ and $\bar{p}$ from the charged hadrons in the $\Delta\gamma^{112}$ measurement. This involves particle identification and rejection of proton candidates, and the corresponding hadron efficiency needs a correction, which is discussed below.

### 4.3.2 Proton Rejection

We identify and exclude all proton candidates based on the ionization energy loss ($dE/dx$) collected by the TPC, which can be described by a Bichsel function. The standard deviation $\sigma_{\text{proton}}$ is defined by:

$$n\sigma \propto \frac{\langle dE/dx \rangle}{\langle dE/dx \rangle_{\text{expectation}}}. \tag{4.1}$$

78

For a particle to be classified as a proton candidate, its measured $dE/dx$ is required to be close to the expected value of a proton, or $\sigma_{\text{proton}} > -2$. This threshold includes around 98% of the $\sigma_{\text{proton}}$ Gaussian distribution. The higher end of the Gaussian distribution contains contributions from other heavier particles such as deuteron, and should be rejected as well. We do not implement additional particle identification (PID) cuts, which are typically done to identify pure particle samples, because our goal is to reject all (anti)proton candidates and include pions and kaons.

In Fig. 4.5, the 2D distribution of $n\sigma_{\text{proton}}$ against the hadron momentum, $p$, is illustrated at different BES-II energies. In the 2D distribution, the bright central band represents proton candidates whose $dE/dx$ is within around $2\sigma$ of the expectation. For Au+Au collisions with beam energies ranging from 9.2 to 27 GeV, the distribution peak for $n\sigma_{\text{proton}}$, which indicates the deviation from the expected energy loss value for a proton, centers around zero. Accordingly, we apply a cut of $\sigma < -2$ to exclude proton candidates for these six energies. At the lower energy of 7.7 GeV, the $n\sigma_{\text{proton}}$ distribution peak is shifted to approximately -0.5 at low momenta. Correspondingly, we adjust the proton exclusion cut to $\sigma < -2.5$ to effectively encompass this variation.

Therefore, the following PID cut is applied to exclude proton candidates:

- $n\sigma_{\text{proton}} < -2$ (at 7.7 GeV, it is tightened to be $n\sigma_{\text{proton}} < -2.5$)

In addition, at higher momenta of $p > 1.4$ GeV/c, the bands of other hadron particles (mostly $\pi^{\pm}$ and $K^{\pm}$) merged with the proton band. Thus, we restrict momentum to $p < 1.4$ GeV/c. The effective yield at higher momenta ($p > 1.4$ GeV/c) is less than 0.1% of the total hadron yield, after applying the proton rejection cut on $n\sigma$. For 7.7 GeV, the two bands are found to merge earlier. Therefore, we further restrict the upper momentum limit to $p < 1.3$ GeV/c.
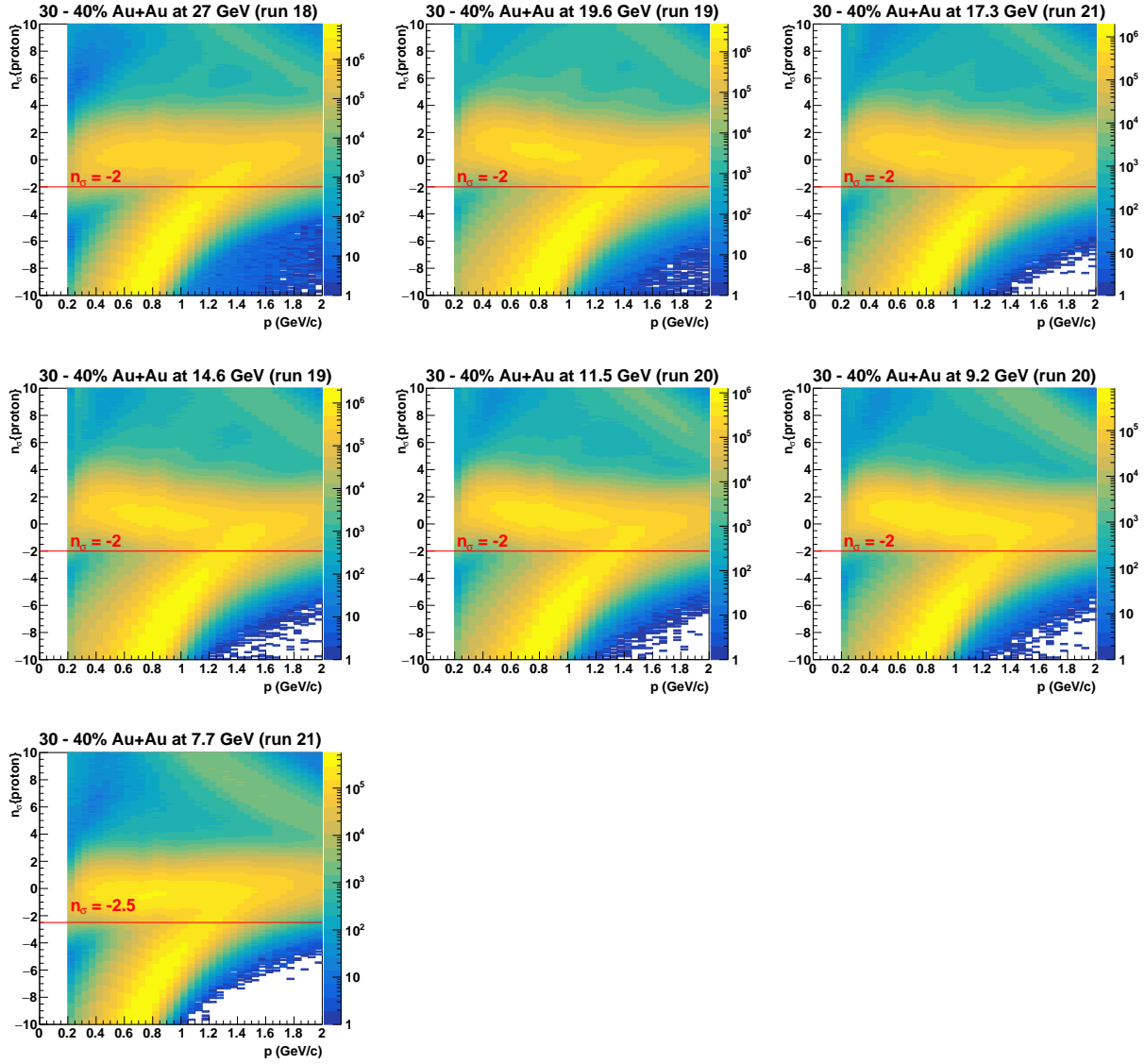
Figure 4.5: Particle Identification for proton candidates based on $n\sigma_{\mathrm{proton}}$ distribution. The red lines marks the proton $dE/dx$ within around $2\sigma$ of the expectation value for $9.2 - 27$ GeV, and above $2.5\sigma$ for 7.7 GeV.

### 4.3.3 Proton rejection efficiency correction

When the (anti-)proton candidates are rejected from the POI, the overlap of the targeted hadron bands (particularly $\pi^\pm$ and $K^\pm$) with the proton band around $p = 1 - 1.4$ GeV/$c$ results in the potential loss of POI with the $n\sigma_{\text{proton}}$ cut. This requires an efficiency correction due to proton rejection. Since the number of anti-protons is generally much lower than that of protons (the $\bar{p}/p$ ratio is approximately 10% at 27 GeV and less than 1% at 7.7 GeV), this proton rejection efficiency correction must be distinguished for positively and negatively charged particles separately.
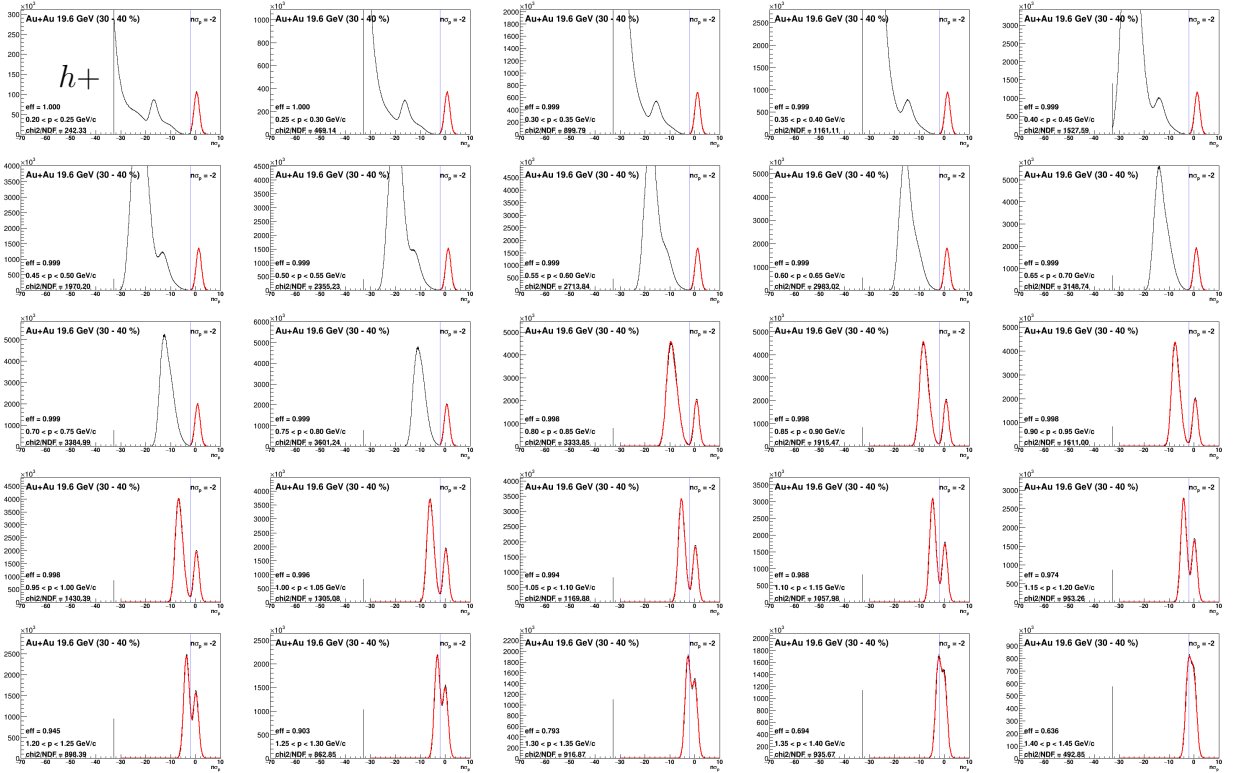


Figure 4.6: $n\sigma_{\text{proton}}$ distribution for all positive hadrons ($h^+$) for $0.2 < p < 1.45$ GeV/$c$ in 30–40% Au+Au at 19.6 GeV (run 19).

The typical $n\sigma_p$ distribution for the positive hadrons ($h^+$) is illustrated in Fig. 4.6 in 30–40% Au+Au at 19.6 GeV, which covers the momentum $p$ range $0.2 - 1.45$ GeV/$c$ with narrow intervals of 0.05 GeV/$c$. The proton peaks are then determined in this projected

$n\sigma_p$ distribution using a multi-Gaussian fit with the proton peak by definition located near $n\sigma = 0$, and a standard deviation around 1.

To better obtain the proton contribution, the following fitting strategy at different momentum regions has been applied.

- For $p < 0.8$ GeV/$c$, the hadron and proton peaks are well-separated, and a single proton Gaussian is fitted.

- For $0.8 < p < 1.2$ GeV/$c$, the $\pi^{\pm}$, $K^{\pm}$, and $p$ peaks are close to merging, but may have different mean and $\sigma$ values, thus three separate Gaussian distributions are fitted to optimize the proton peak.

- For $p > 1.2$ GeV/$c$, the hadron and proton bands are merged, with $\pi^{\pm}$, $K^{\pm}$ mean values nearly identical. Thus, we fit two Gaussian distributions for $p$ and $h$ separately.

The hadron peaks completely merge with protons beyond $p > 1.4$ GeV/$c$, which sets our track level cut.

The hadron efficiency after proton rejection, denoted as $e_{\mathrm{PR}}$, is calculated by subtracting the proton yield, determined from the fitted Gaussian peak, from the total entries in the histogram. The proton Gaussian fitting parameters are extracted from the strategy discussed previously.

$$e_{\mathrm{PR}} = \frac{N^{p<1.4}}{N^{Total} - \mathrm{A}^{\mathrm{protonGaus}}}, \tag{4.2}$$

where $N^{p<1.4}$ means histogram entries for $p < 1.4$ GeV/$c$, $N^{Total}$ is total entries, and $\mathrm{A}^{\mathrm{protonGaus}}$ is the area of the proton peak over the full ranges.

Similarly, for negative hadrons ($h^{-}$), we employ the same strategy on each momentum bin to calculate the hadron efficiency after (anti-)proton rejection, $e_{\mathrm{PR}}$. The corresponding example for $h^{-}$ in the 30–40% centrality class of Au+Au collisions at 19.6 GeV is illustrated in Fig. 4.7. Notably, the peak height corresponding to anti-protons is significantly lower than that for protons.
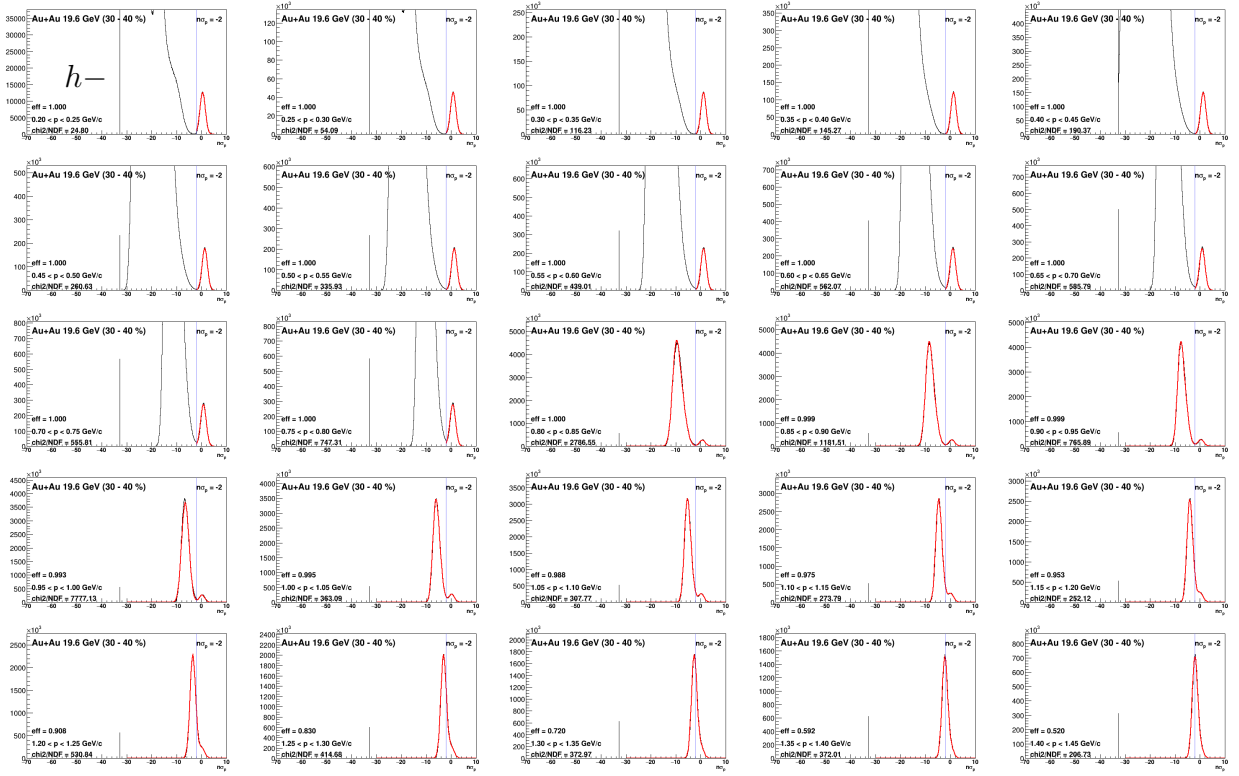
Figure 4.7: $n\sigma_{\text{proton}}$ distribution for all negative hadrons in $0.2 < p < 1.45$ GeV/$c$ in 30–40% Au+Au at 19.6 GeV (run 19).

Across different centrality bins from 0–80%, the efficiency $e_{\text{PR}}$ for $h^+$ and $h^-$ is calculated for each momentum bin and then fitted with a Sigmoid function to model the behavior,

$$y = \frac{1}{1 + e^{-a(x-b)}}. \tag{4.3}$$

The Sigmoid function in this context is designed to approach the maximum value of 1 at low momenta. The momentum $p$ dependence of efficiency $e_{\text{PR}}$ for $h^+$ and $h^-$ is illustrated in Fig. 4.8 and Fig. 4.9, respectively.

For 7.7 GeV, the cut of $n\sigma < -2.5$ is applied in calculating $e_{\text{PR}}$. Since the transported-proton effect is stronger at this energy, the $h^+$ band merges earlier with the proton band at around $p = 1.3$ GeV/$c$. Therefore, the momentum upper limit is set to $p < 1.3$ GeV/$c$.
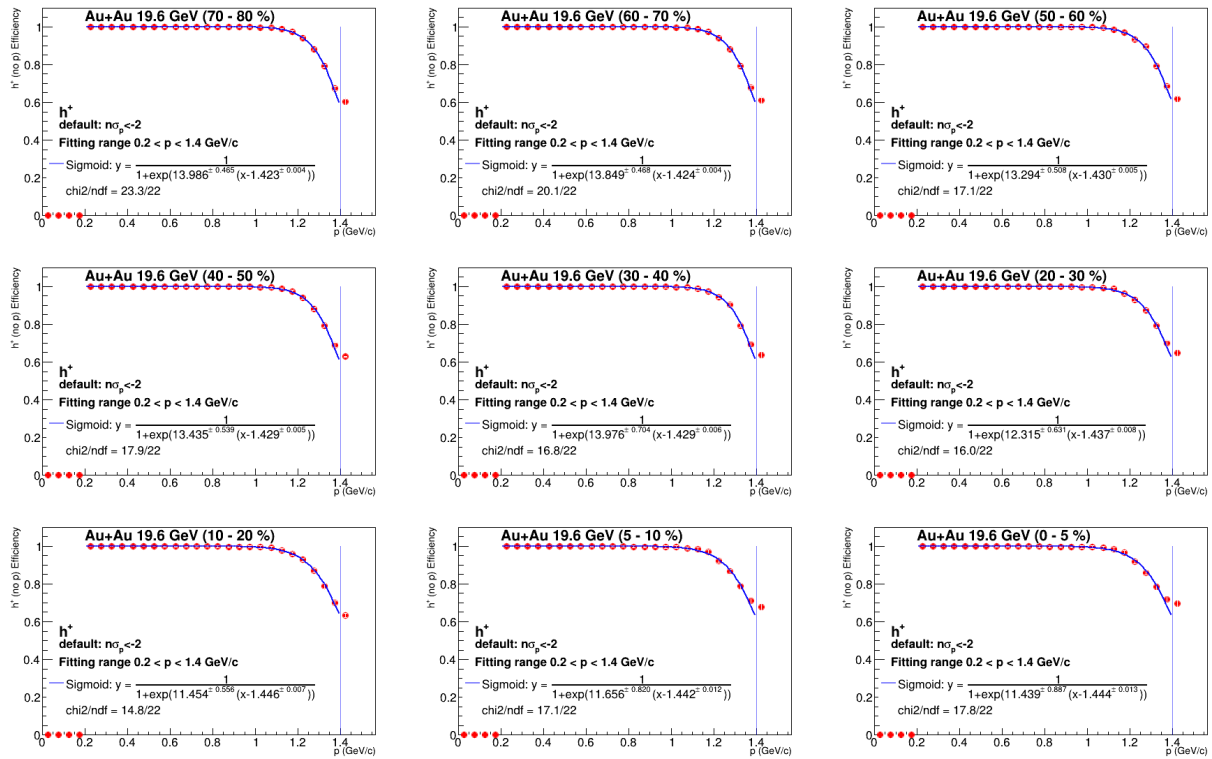
Figure 4.8: Hadron efficiency after proton rejection $e_{\mathrm{PR}}$ for $h^+$ in Au+Au at 19.6 GeV.
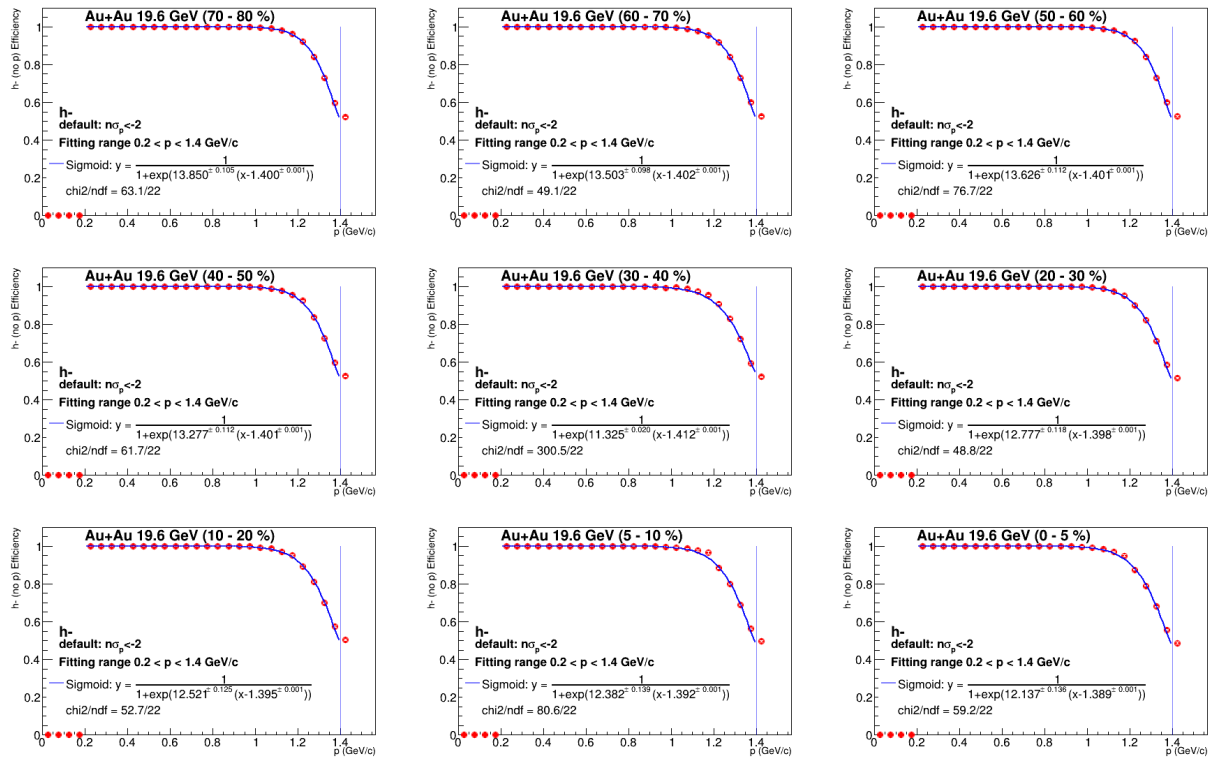
Figure 4.9: Hadron efficiency after antiproton rejection $e_{\mathrm{PR}}$ for $h^-$ in Au+Au at 19.6 GeV.

## 4.4 TPC detector corrections

This work primarily uses the particle information from the Time Projection Chamber (TPC) and Event Plane Detector (EPD) at STAR. Detector correction is required to compensate for the uneven azimuthal angle distribution and efficiency loss such that the systematic effects are minimized. The hadron tracks are reconstructed using the Time Projection Chamber (TPC) hits within $|\eta| < 1$ and are selected based on the event-level and track-level cuts outlined in previous sections. After (anti)proton rejection, these particles are designated as Particles of Interest (POI). Our analysis targets the 0–80% centrality range, with particular interest in the mid-central region of 20–50% to search for the Chiral Magnetic Effect. This is where the prerequisites of a strong magnetic field from spectator protons, and the QGP matter from participants can be simultaneously satisfied to stimulate the charge separation signal perpendicular to the reaction plane.

In the following, I will first discuss the TPC correction for particle azimuthal angle distribution $\varphi$, and the TPC acceptance efficiency loss correction.

### 4.4.1 TPC $\varphi$ flatness

The TPC detector tracks the momentum of the particles, and this work primarily focuses on transverse momentum, $\vec{p_T} = (p_x, p_y)$. The azimuthal angle $\varphi$ of a POI is derived from the transverse momentum vector as $\varphi = \tan^{-1} \frac{p_y}{p_x}$. Given that the reaction plane is unknown and presumed to be randomly distributed, the overall data distribution of particle angle $\varphi$ is ideally expected to be uniform over $(0, 2\pi)$. However, due to the detector non-uniformity and potential time-dependent effects from specific operational periods, the raw $\varphi$ distribution could not be quite flat.

To correct the detector effects, we employ a shifting method that adjusts each angle by adding a correction obtained from the Fourier coefficients of the raw distribution up to the fifth order. Additionally, the full data set was segmented into multiple subsets, each
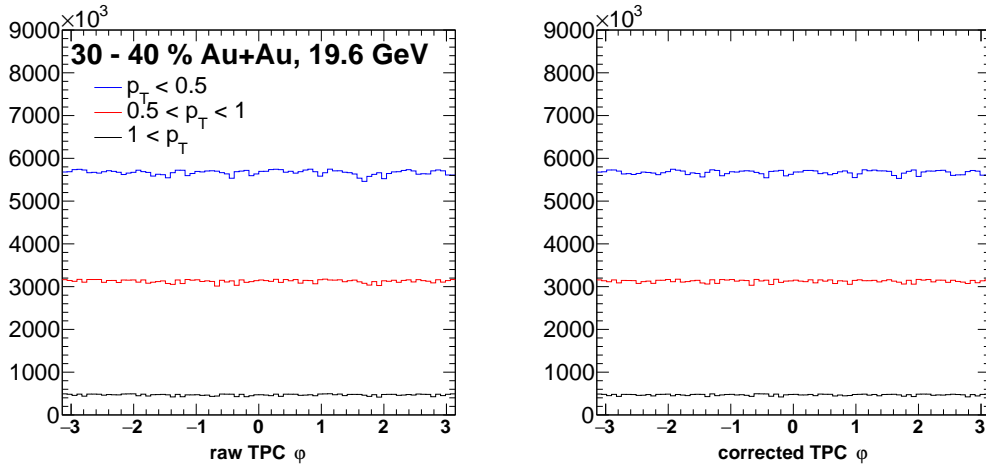
Figure 4.10: The azimuthal angle distribution for particles of interest within $-0.1 < \eta < 0.1$, (left) before and (right) after flattening.

containing 10 neighboring runs to gather sufficient statistics and prevent over-weighting. The POI are initially grouped into three transverse momentum ranges: $0.2 < p_T < 0.5$ GeV/$c$, $0.5 < p_T < 1$ GeV/$c$, and $p_T > 1$ GeV/$c$. They are also categorized into 10 pseudorapidity ($\eta$) sets ranging from $(-1, 1)$, as illustrated in Fig. 4.10 for an example of the $\varphi$ distribution in $-0.1 < \eta < 0.1$ in 30–40% Au+Au collisions at 19.6 GeV.

After applying the angular adjustments, the lower Fourier orders ($n < 5$) in the TPC $\varphi$ distributions are effectively flattened. In practice, we also observe that for most energies at BES-II, the raw distribution is fairly flat, suggesting that the $\varphi$ shifting should have a minimal impact.

### 4.4.2 TPC acceptance and reconstruction efficiency

In the reconstruction of the charged particles, possible TPC inefficiency at lower transverse momenta requires additional correction for its acceptance, which is known as the TPC tracking efficiency ($e_{\mathrm{TPC}}$). The detector acceptance and reconstruction efficiency of TPC are simulated by using STAR embedding data. For this analysis, the $e_{\mathrm{TPC}}$ of $\pi^\pm$ is calculated based on the fact that most charged hadrons after rejecting (anti)protons would be pions.

87

$e_{\text{TPC}}$ is calculated from the yield ratio of reconstructed tracks to Monte Carlo tracks in embedding data,

$$e_{\text{TPC}} = \frac{Y_{RC}}{Y_{MC}}. \tag{4.4}$$

for different $p_T$ ranges from 0.2–4 GeV/$c$ for each centrality and each collision energy.
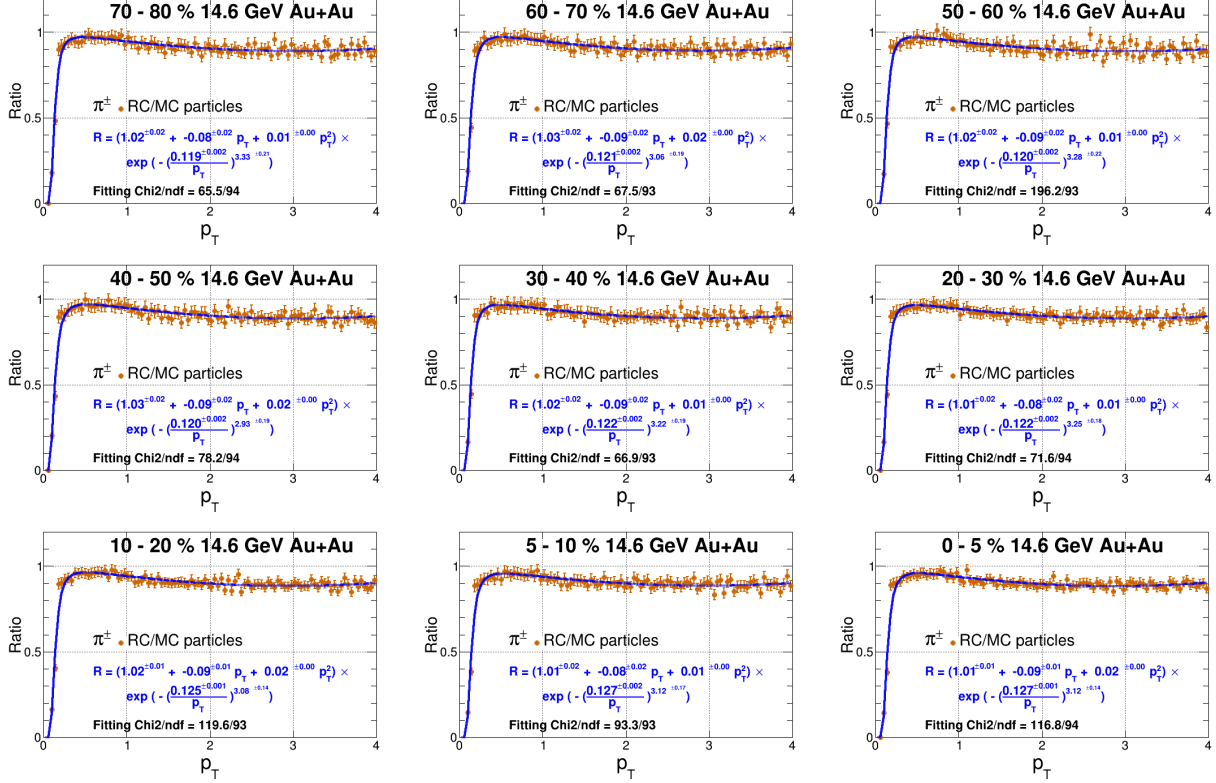


Figure 4.11: TPC efficiency of $\pi^\pm$ in 0–80% Au+Au at 14.6 GeV.

The ratio is fitted with a smooth function,

$$f = (a_0 + a_1 p_T + a_2 p_T^2) \times e^{-(\frac{a_3}{p_R})^{a_4}}, \tag{4.5}$$

to describe the shape. For the BES-II data, a little bump near 0.5 GeV/$c$ is present, which can be well described by the second-order term in the polynomial factorization. In Fig. 4.11, the $e_{\text{TPC}}$ for $\pi^\pm$ is presented for nine centrality bins in 0–80% Au+Au at 14.6 GeV (BES-II).

## 4.5 Event Plane reconstruction

To estimate the reaction plane, we construct the first-order spectator plane (SP) using hits from the Event Plane Detector (EPD) located at forward rapidities, where the protons show a strong correlation with the direction of the magnetic field. The EPD detectors consist of two disks positioned in the forward and backward directions, each equipped to detect charged particle hits within its rings. By using both east and west spectator planes, nonflow effects such as momentum conservation can be suppressed. The EPD detects a pseudorapidity range of $2.1 < |\eta| < 5.1$, which well covers the beam rapidity range of the Beam Energy Scan II for identifying the spectator enriched region. Particularly, we select the EPD hits from $|\eta| > y_{\text{beam}}$ range to define the SP.

### 4.5.1 Spectator Plane

The Event Plane Detector was installed in year 2018 and comprises two disks located on the forward (west) and backward (east) of TPC. Each disk is segmented into 16 concentric rings, extending from the outer to the inner edge. Within each ring, the EPD tiles are responsible for collecting the analog-to-digital converter (ADC) readings from hits and recording the information corresponding to the number of minimum ionizing particles (MIPs). The EPD hits beyond the $\eta > y_{\text{beam}}$ cut (listed in Table 4.3) are used to reconstruct the spectator region, where $y_{\text{beam}} \sim \ln\left(\sqrt{s_{NN}}/m_p\right)$.

Table 4.3: BES-II Beam rapidities and EPD $\eta$ cuts for spectator planes.

| $\sqrt{s_{NN}}$ (GeV) | 7.7 | 9.2 | 11.5 | 14.6 | 17.3 | 19.6 | 27 |
|---|---|---|---|---|---|---|---|
| $y_{\text{beam}}$ | 2.11 | 2.28 | 2.51 | 2.75 | 2.91 | 3.04 | 3.36 |
| EPD $\eta$ cut ($>$) | 2.3 | 2.5 | 2.7 | 3.0 | 3.1 | 3.2 | 3.8 |

The spectator plane is defined from the flow vectors $\overrightarrow{q_1}$

$$\overrightarrow{q_1} = \frac{1}{\sqrt{N}}\Big(\sum_{i=1}^{N} w_i(\eta_i)\cos\varphi_{i,\mathrm{EPD}}, \sum_{i=1}^{N} w_i(\eta_i)\sin\varphi_{i,\mathrm{EPD}}\Big), \qquad (4.6)$$

where $\varphi_{i,\mathrm{EPD}}$ is obtained from the EPD hits at each tile. In practice, a weighting related to $\eta_i$ needs to be added based on each tile to better construct the first-order plane [45]. The first order event plane ($\Psi_1$) is defined as

$$\Psi_1 = \tan^{-1}\frac{q_{1,y}}{q_{1,x}}. \qquad (4.7)$$

The east and west EPD spectator planes are separately constructed.

### 4.5.1.1 EPD weights from $v_1(\eta)$

To optimize the detector performance and the event plane resolution, a weight for EPD hit is applied by the direct flow at the forward direction ($v_1(\eta)$) [134]. This method was first implemented to BES-II data at 27 GeV in published analyses utilizing the forward EPD [70], and was confirmed to significantly enhance the event plane resolutions. Following the same procedure, we calculated the $v_1(\eta)$ distribution at other BES-II energies, which is defined by

$$v_1 = \frac{\langle\cos(\varphi_{i,\mathrm{EPD}} - \Psi_{1,\mathrm{TPC}})\rangle}{Res_{1,full}}, \qquad (4.8)$$

where the first-order event plane ($\Psi_{1,\mathrm{TPC}}$) is constructed from the TPC in the same way as Eq. (4.7). All charged hadrons are chosen for $|\eta| < 1$, $0.2 < p_T < 2$ GeV/$c$, and applying the flatness procedure (see discussions above) both for $\varphi$ and for $\Psi_1$.

The resolution of a TPC $\Psi_1$ is calculated using the sub-event method [45]. The charged hadrons are randomly divided into two samples to construct two TPC sub-events, $\Psi_{1,e}$ and $\Psi_{1,w}$, and the resolution of the sub-event plane is obtained with $Res_{sub} = \sqrt{\langle\cos(\Psi_{1,e} - \Psi_{1,w})\rangle}$. Then, the sub-event plane $\chi_{sub}$ is estimated from $Res_{sub}$ by the inverse function of the following Bessel function:

$$Res_1 = \frac{\sqrt{\pi}}{2\sqrt{2}}\chi_1\exp{-\chi_1^2/4}[I_0(\frac{\chi_1^2}{4}) + I_1(\frac{\chi_1^2}{4})]. \qquad (4.9)$$

90

Based on the relationship $\chi \sim \sqrt{N}$, where $N$ represents the number of particles, the full event plane $\chi$ is estimated by $\chi_{full} = \sqrt{2}\chi_{sub}$. The calculated $\chi_{full}$ value is then incorporated into Eq. (4.9) to yield $Res_{1,full}$, the full event plane resolution.
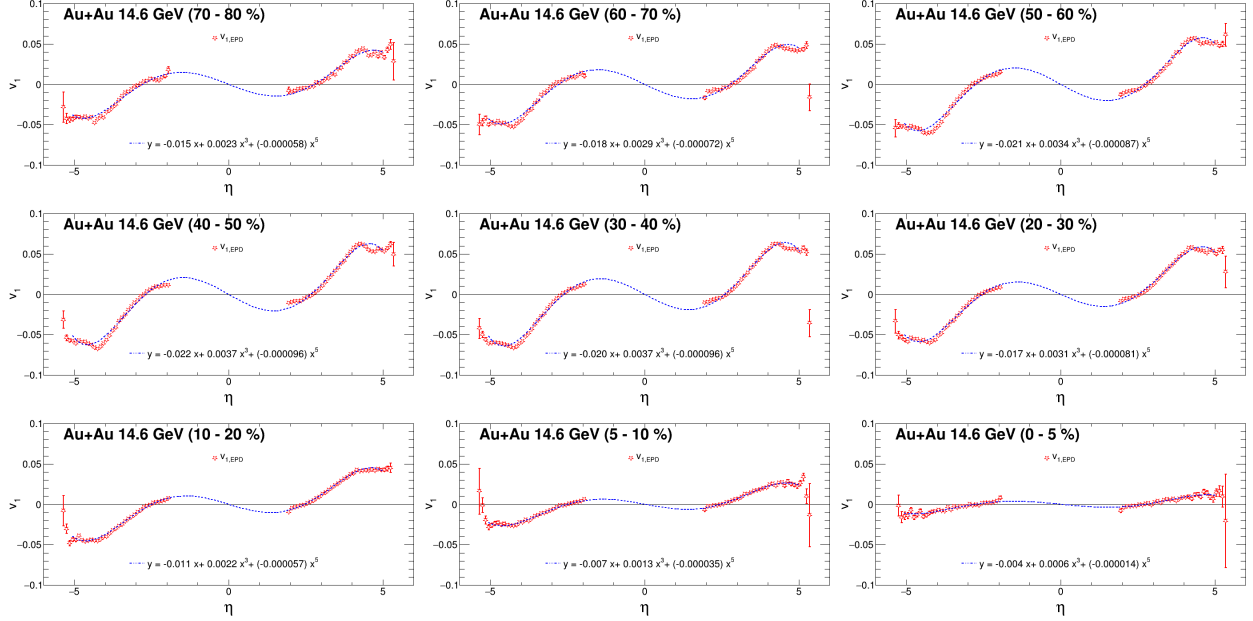


Figure 4.12: $v_1(\eta)$ for EPD hits in 0–80% Au+Au at 14.6 GeV.

$v_1(\eta)$ for $-6 < \eta < 6$ is illustrated in Fig. 4.12 in Au+Au at 14.6 GeV, and the data points roughly cover the EPD hits from $\eta \in (-5.1, 5.1)$. The zero-crossing point in negative (positive) pseudorapidity marks the boundary between spectator and participant regions.

Note that this $v_1$ might differ from other published values by a scale factor, as we have not applied additional scaling corrections for the TPC mid-rapidity effect. For our purposes, this $v_1(\eta)$ serves as a weight for the EPD, thus its absolute value of $v_1(\eta)$ is not critical. Instead, its relative value is to our concern.

An odd polynomial function is used to fit $v_1(\eta)$ in each centrality bin with $v_1 = p_0\eta + p_1\eta^3 + p_2\eta^5$ for Au+Au at 7.7 –14.6 GeV, and $v_1 = p_0\eta + p_1\eta^3$ for Au+Au at 19.6 GeV. The inclusion of the fifth-order term is not always necessary. This value is then applied to each tile of the EPD detector in reconstructing the spectator plane.

### 4.5.1.2 EPD spectator plane $\Psi_1$ flattening

In order to correct for the detector azimuthal unevenness, a similar shifting approach is applied to the EPD $\Psi_1$ as discussed in Sec. 4.4.1. The dataset is segmented into several subsets based on every ten run periods, with corrections applied up to the 5th-order Fourier coefficients.
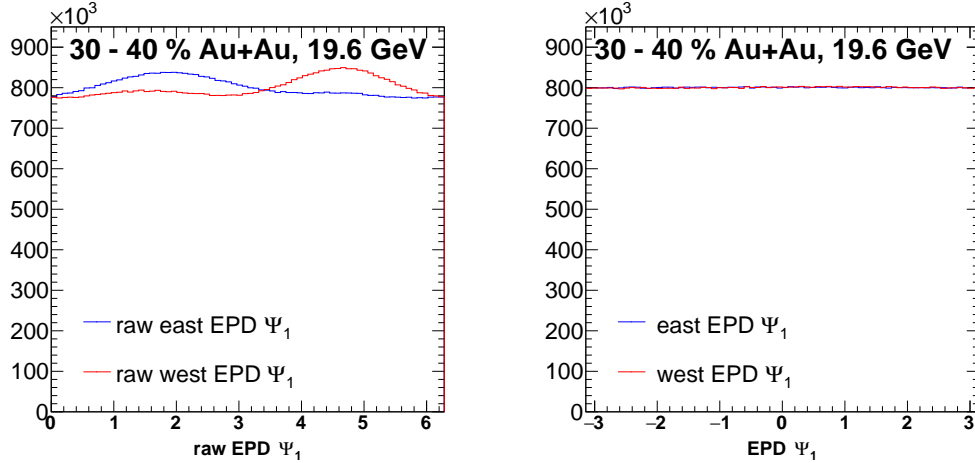


Figure 4.13: EPD east and west $\Psi_1$ distribution before (left) and after (right) flattening in 30–40% Au+Au at 19.6 GeV.

As illustrated in Fig. 4.13, the raw spectator plane distribution takes the range $(0, 2\pi)$. After applying the flatness correction, we adjust $\Psi_1$ into the range $(-\pi, \pi)$, by subtracting $2\pi$ from $\Psi_1$ if it exceeds $\pi$, or adding $2\pi$ if it falls below $-\pi$. The EPD spectator plane distribution is flat after correction for both east and west disks.

### 4.5.1.3 Spectator Plane $\Psi_1$ resolution

Both the east and west EPD planes are utilized in the measurement, effectively canceling out the momentum conservation effect. Consequently, the resolution is calculated using the sub-event plane method.

$$Res_{1,sub} = \sqrt{\langle \cos(\Psi_{1,e} - \Psi_{1,w}) \rangle}. \tag{4.10}$$

The obtained SP resolution in 0–80% Au+Au at BES-II energies is shown in Fig. 4.14. The resolution is significantly higher in the mid-central region. The resolution at higher energies in the BES-II, particularly at 27 GeV, is limited by the EPD hit statistics, because nearly half of the EPD was excluded to select the spectator region.
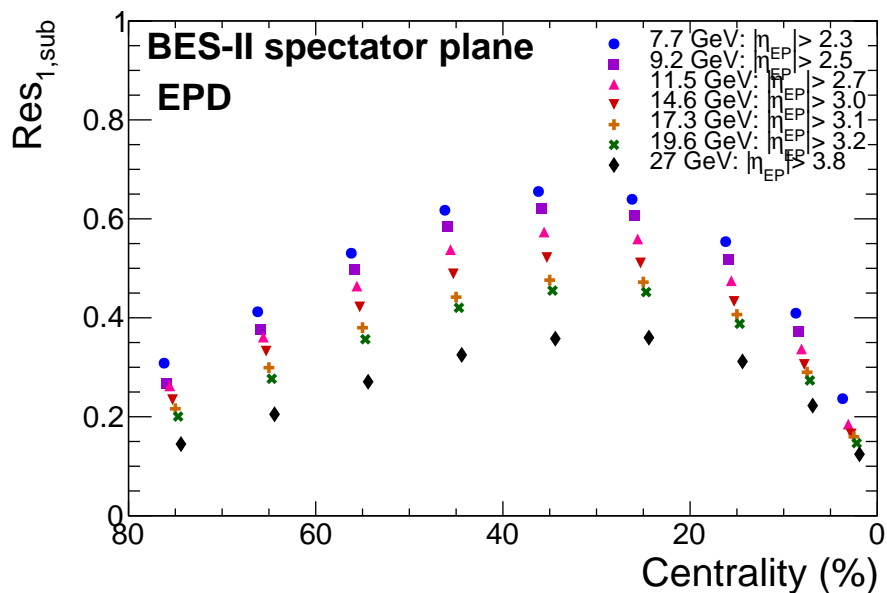


Figure 4.14: Resolution of EPD $\Psi_1$ in BES-II.

## 4.6 Systematic uncertainties

### 4.6.1 systematic sources

The assessment of systematic uncertainties is critical to understanding the potential influence of a single detector on the analysis results, which is not precisely defined and different from statistical uncertainties. These effects generally come from the detector performance, such as effects from backgrounds, beam position, energy resolution, variation of efficiency, etc [135], and/or from the imperfect understanding of the theory, and/or the uncertainty associated with analysis correction. The uncertainty of these systematic effects needs to be addressed

and remains one of the most important tasks in data analysis of high-energy experiments. Unlike the statistical uncertainties, which are typically Gaussian distributed, the systematic uncertainties don't necessarily follow the same distribution. Many aspects can be used to evaluate systematics, including calibration, method comparison, and performance stability assurance. The cut variation is the standard way to evaluate the detector's performance. In this work, we conduct the systematics assessment based on individual variations of the following cuts used in the work:

Table 4.4: Default and varied cuts for the systematic uncertainty study.

| Cut | default | systematic check |
|---|---|---|
| Vertex z | $|V_z| < 70$ cm | $0 < V_z < 70$ cm |
| global DCA | $< 3$ cm | $< 1$ cm |
| nFitHits | $> 15$ | $> 20$ |
| Track Splitting ratio | no cut | $0.52 < $ nFitHits/nMaxHits $< 1.05$ |
| $n\sigma_p$ | $n\sigma_p < -2$ | $n\sigma_p < -3$ |
| | (7.7 GeV) $n\sigma_p < -2.5$ | $n\sigma_p < -3.5$ |

The $V_z$ cut is implemented to assess the vertex position effect in the TPC detector by comparing positive and negative rapidities. The variation of DCA and the number of hits used in track fitting aims to evaluate the detector's particle reconstruction capabilities. Typically, the DCA value has a resolution around 0.5 cm, and a DCA selection below 1 cm makes no difference. The criteria on track splitting test its possibly different influences on the same-charge and opposite-charge pairs in measurements. The last one, the $n\sigma$ variation, is applied to assess the particle identification (PID) effect.

94

### 4.6.2 Barlow approach

For each variation $i$, we apply the Barlow test [136] to account for the contributions from statistical uncertainties. In this approach, systematic checks should utilize a subset of the analysis dataset, where the analyses are conducted identically. Within this subset, the purely statistical covariance matrix yields a $1\sigma$ deviation from the mean as $\sigma = \sqrt{\sigma_{df}^2 - \sigma_i^2}$. By examining the discrepancy between the variance of central values and statistical uncertainties, we can assess the impact of systematic effects.
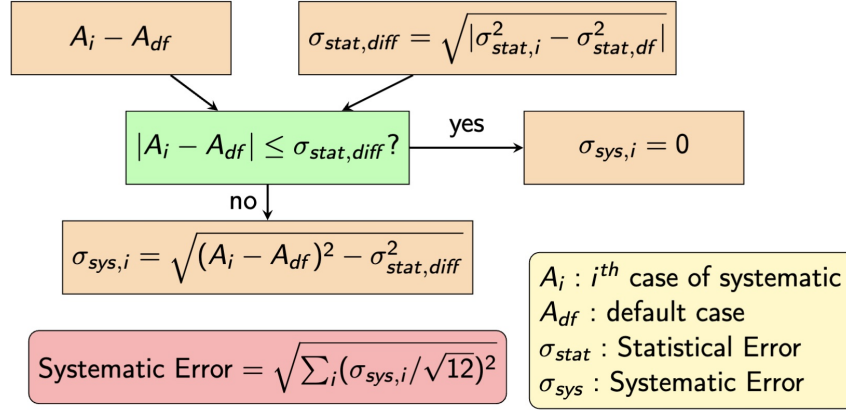


Figure 4.15: Procedure to obtain systematic uncertainties, including the Barlow test.

As illustrated in Fig. 4.15, the $\sigma_{stat,d}$ and $\sigma_{stat,i}$ denote the statistical uncertainties for the results with the default and varied cuts, respectively. If $\Delta_i^2 = (A_i - A_{df})^2$ exceeds $|\sigma_{stat,i}^2 - \sigma_{stat,d}^2|$, it passes the Barlow test, we define the systematic uncertainty for this case as $\sigma_i = \sqrt{\Delta_i^2 - |\sigma_{stat,i}^2 - \sigma_{stat,d}^2|}$. Otherwise, the contribution of this systematic is zero, $\sigma_i = 0$. The overall systematic uncertainty is the quadrature sum of $\sigma_i/\sqrt{12}$, assuming a uniform probability distribution.

In our work, we find that the DCA and $n\sigma_p$ cuts are the primary systematic sources, each typically at the level of 10% of the corresponding statistical uncertainty. The variations in the rest of the cuts have negligible effects.

### 4.6.2.1 gDCA cut scan

As an example, the global DCA variation is checked with a scan of the cut from 1 to 3 cm, and the results for $\langle \Delta\gamma^{112} \rangle$ are presented below in Fig. 4.16 for Au+Au collisions at 19.6 GeV.
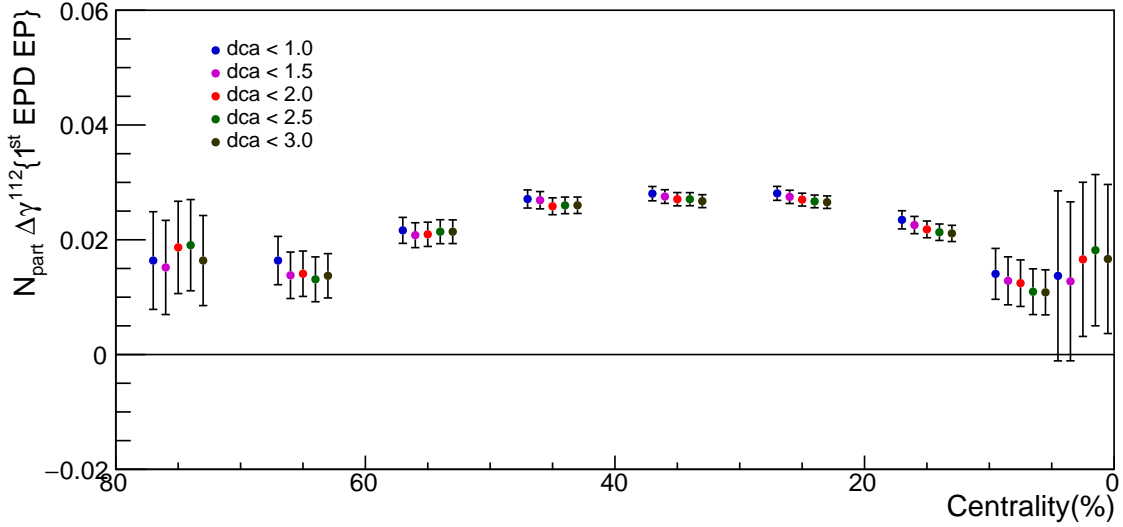


Figure 4.16: Scan of systematic variations on the gDCA cut from 1 to 3 cm at 19.6 GeV.

By scanning the DCA cut, we confirm that the cuts at 1 and 3 cm define the upper and lower bounds, respectively, of the maximum allowable range. This validation enables us to continue with the previously outlined calculation procedure utilizing the assumption of a uniform distribution. We find that the overall systematic uncertainties are small as this measurement is dominated by statistical uncertainties.

# CHAPTER 5

# Results

We report the charge separation measurement with a three-point correlator $\Delta\gamma^{112}$ in search of the Chiral Magnetic Effect (CME) in Au+Au collisions at RHIC BES-II. The Event Shape Selection method is applied to minimize the flow background in the $\Delta\gamma^{112}$ measurements, by projecting $\Delta\gamma^{112}$ to zero-flow limit and obtain the corresponding $\Delta\gamma^{112}_{\text{ESS}}$. The charge separation measurement is conducted with respect to the spectator planes reconstructed from EPD detector, which effectively mitigate the nonflow background contributions. Here, we report and discuss the observed finite charge separation after background subtraction at BES-II data.

## 5.1   Observables

The observables in this work include flow vector $q_2^2$, elliptic flow $v_2$, the CME observable $\Delta\gamma^{112}$, and the background indicator $\Delta\gamma^{132}$ and $\Delta\delta$. All the variables are calculated based on the charged hadron POI from the TPC and the SP reconstructed from the EPD. Then, necessary efficiency corrections from $e_{PR}$ (PID proton rejection) and $e_{\text{TPC}}$ are implemented. The systematic uncertainties are then evaluated.

In addition to the single particle $\varphi$ of POI, we construct the particle pairs of interest (PPOI) angle $\varphi_p$ from adding the momenta of two POI particles, $\varphi_p = \arctan(\frac{p_{1y}+p_{2y}}{p_{1x}+p_{2x}})$. The following is a list of observables for this work:

- event shape $q_2^2 = \frac{1}{N+N^2\langle v_2\rangle^2}\{[\sum_i^N \cos(2\varphi)]^2 + [\sum_i^N \sin(2\varphi)]^2\}$

- pair event shape $q^2_{2,\text{PPOI}} = \frac{1}{N_p + N_p^2 \langle v_{2,\text{PPOI}} \rangle^2} \{ [\sum_i^{N_p} \cos(2\varphi_p)]^2 + [\sum_i^{N_p} \sin(2\varphi_p)]^2 \}$

- elliptic flow $v_2 = \langle \cos(2\varphi - \Psi_{1,e} - \Psi_{1,w}) \rangle / Res^2_{1,sub}$

- pair elliptic flow $v_{2,\text{PPOI}} = \langle \cos(2\varphi_p - \Psi_{1,e} - \Psi_{1,w}) \rangle / Res^2_{1,sub}$

- CME sensitive $\gamma^{112} = \langle \cos(\varphi_1 + \varphi_2 - \Psi_{1,e} - \Psi_{1,w}) \rangle / Res^2_{1,sub}$

- background indicator $\gamma^{132} = \langle \cos(\varphi_1 - 3\varphi_2 + \Psi_{1,e} + \Psi_{1,w}) \rangle / Res^2_{1,sub}$

- two particle correlator $\delta = \langle \cos(\varphi_1 - \varphi_2) \rangle$

For the event shape variables $q^2$, $N$ denotes the total number of POI in one event, while $N_p$ refers to the total PPOI number, which is typically $\sim N^2$ for each event. The correction term $\langle v_2 \rangle$ is applied as a proxy of the two-particle cumulant $v_2\{2\}$.

The elliptic flow variable $v_2$ and the $\gamma$ correlator require the correction for the spectator plane resolution, as defined in Eq. (4.10). After measuring $\gamma$ for opposite- and same-sign pairs of $\varphi_1$ and $\varphi_2$, one can obtain the CME sensitive observable $\Delta\gamma^{112} = \gamma_{\text{OS}}^{112} - \gamma_{\text{SS}}^{112}$. Similarly, for the BKG-indicator, $\Delta\gamma^{132} = \gamma_{\text{OS}}^{132} - \gamma_{\text{SS}}^{132}$.

## 5.2 Event Shape Selection

The Event Shape Selection method first categorizes the events based on the size of $q^2_{2,\text{POI}}$ or $q^2_{2,\text{PPOI}}$ into multiple subsets. The typical distributions of $q^2_{2,\text{POI}}$ and $q^2_{2,\text{PPOI}}$ for mid-centrality 30–40% Au+Au at 19.6 GeV are illustrated in Fig. 5.1. After applying first-order corrections, the mean value of $q^2_{2,\text{POI}}$ is close to one. However, the mean for $q^2_{2,\text{PPOI}}$ remains around 4, suggesting the need for higher-order corrections.

Therefore, in the ESS projection, we retain up to 97% of total events by implementing an upper limit cut of $< 3.4\langle q_2^2 \rangle$ based on the mean value of $\langle q_2^2 \rangle$. This exclusion of the 3% of events with large $q_2^2$, typically characterized by $q_2^2 > 5$ and $q^2_{\text{PPOI}} > 15$ in mid-central
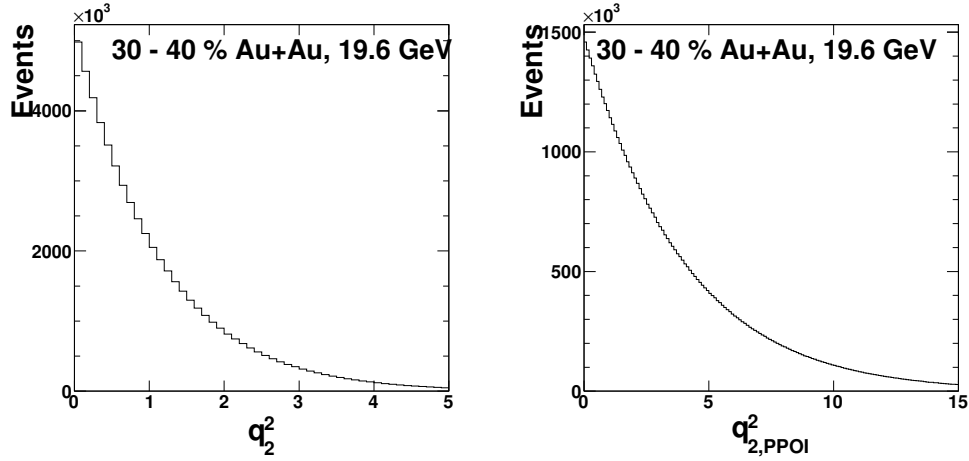
98

Figure 5.1: The distributions of (left) $q_2^2$ and (right) $q_{2,\mathrm{PPOI}}^2$ in 30–40% Au+Au collisions at 19.6 GeV.

events, is due to the statistical unreliability of a few events, and possible contamination from other effects such as potential detector inefficiency bias. Furthermore, the spectator plane resolution in the large $q^2$ fringes turns unrealistically negative, with substantial statistical errors. The mean values of $q_2^2$ may vary according to centrality, thus this selection helps to minimize statistical uncertainties across collision centrality.
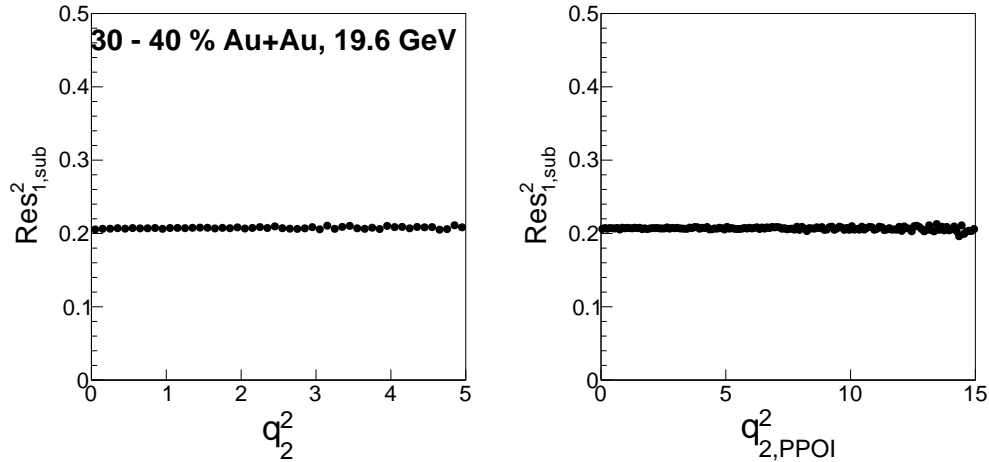


Figure 5.2: The sub-event resolution as a function of (left) $q_2^2$ and (right) $q_{2,\mathrm{PPOI}}^2$ in 30–40% Au+Au at 19.6 GeV.

In each data subset marked by $q_2^2$, the spectator plane resolution $Res_{1,sub}$ is measured, as

99

shown in Fig. 5.2 in 30–40% Au+Au at 19.6 GeV. $Res_{1,sub}$ is stable as a function of the POI or PPOI $q_2^2$, suggesting the successful reconstruction of the spectator plane with the EPD, which is not highly correlated with the participants at midrapidities.
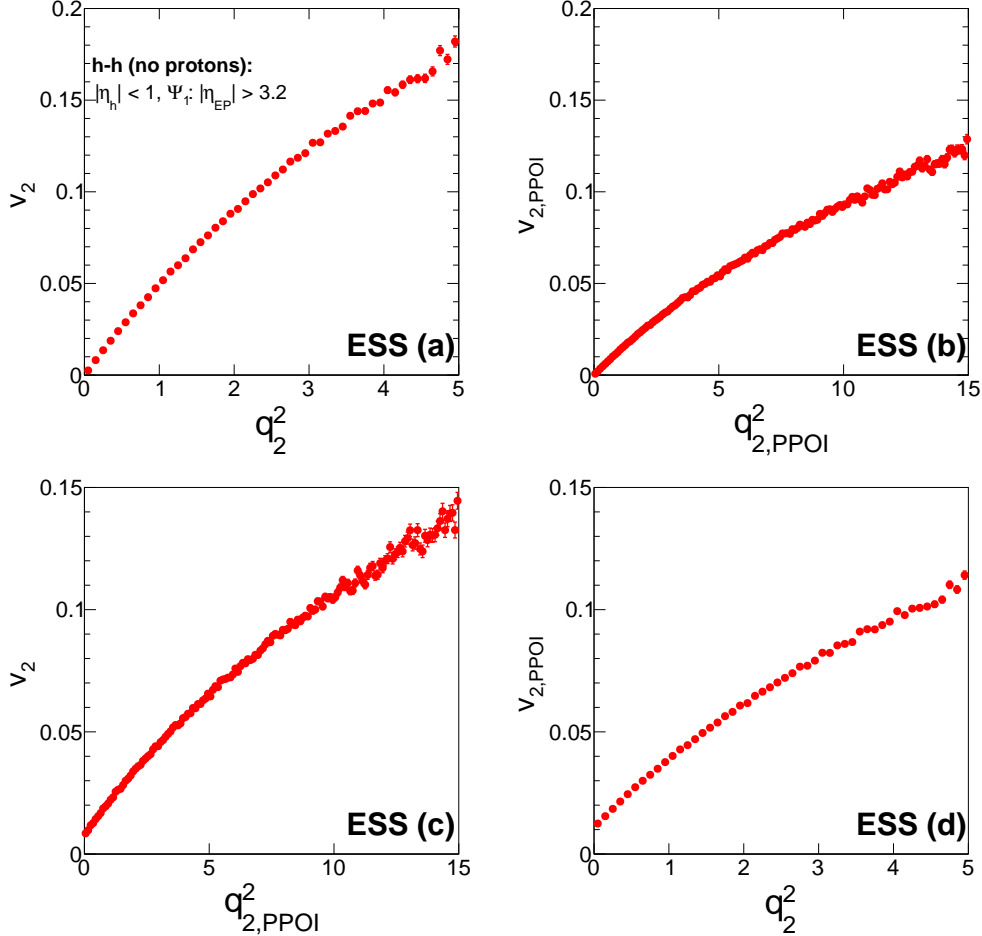


Figure 5.3: The four ESS combinations: $v_2$ or $v_{2,\mathrm{PPOI}}$ vs $q_2^2$ or $q_{2,\mathrm{PPOI}}^2$ in 30–40% Au+Au at 19.6 GeV.

Similarly, the flow coefficients $v_2$ and $v_{2,\mathrm{PPOI}}$ are plotted against $q_{2,\mathrm{POI}}^2$ and $q_{2,\mathrm{PPOI}}^2$, yielding four distinct ESS combinations (a)–(d), as depicted in Fig. 5.3. Utilizing the same particles as in panels (a) and (b), a strong correlation between $v_2$ and $q_2^2$ is observed, and $v_2$ reaches zero at zero $q_2^2$. However, it introduces a residual background due to self-correlation in subsequent mappings of $\Delta\gamma$-$v_2$.

The mixed combinations in panels (c) and (d) effectively mitigate this self-correlation and reduce residual backgrounds. $v_2$ and $q_2^2$ from different sources are correlated by eccentricity at the same kinematic regions as well as the emission pattern fluctuations. Consequently, at the zero event shape, both $v_2$ and $v_{2,\text{PPOI}}$ are finite though quite close to zero. This allows for a reliable projection to the zero-flow limit, meanwhile suppressing residual backgrounds.

With the same approaches, the correlator $\gamma^{112}$ and $\gamma^{132}$ are measured for the same-sign (SS) and opposite-sign (OS) pairs as a function of $q_{2,\text{POI}}^2$ and $q_{2,\text{PPOI}}^2$. The results are presented in Fig. 5.4 for the 30–40% centrality Au+Au collisions at 19.6 GeV. In each row, the left column displays the $\gamma$ correlator for OS pairs (in blue) and SS pairs (in red) separately. The average values for OS and SS pairs highlight the total momentum conservation effect. Since the particle pairs contributing to $\gamma^{112}$ are also employed to construct $q_{2,\text{PPOI}}^2$, a correlation between these variables is seen.

The differences $\Delta\gamma^{112}$ (solid marker) and $\Delta\gamma^{132}$ (open marker) at different $q_2^2$ bins are shown in the right column. An increasing trend is present, which indicates the contribution from the flow background correlated to emission patterns. $\Delta\gamma^{132}$ is similarly influenced as $\Delta\gamma^{112}$, but at a reduced extent, which was consolidated by many other studies.
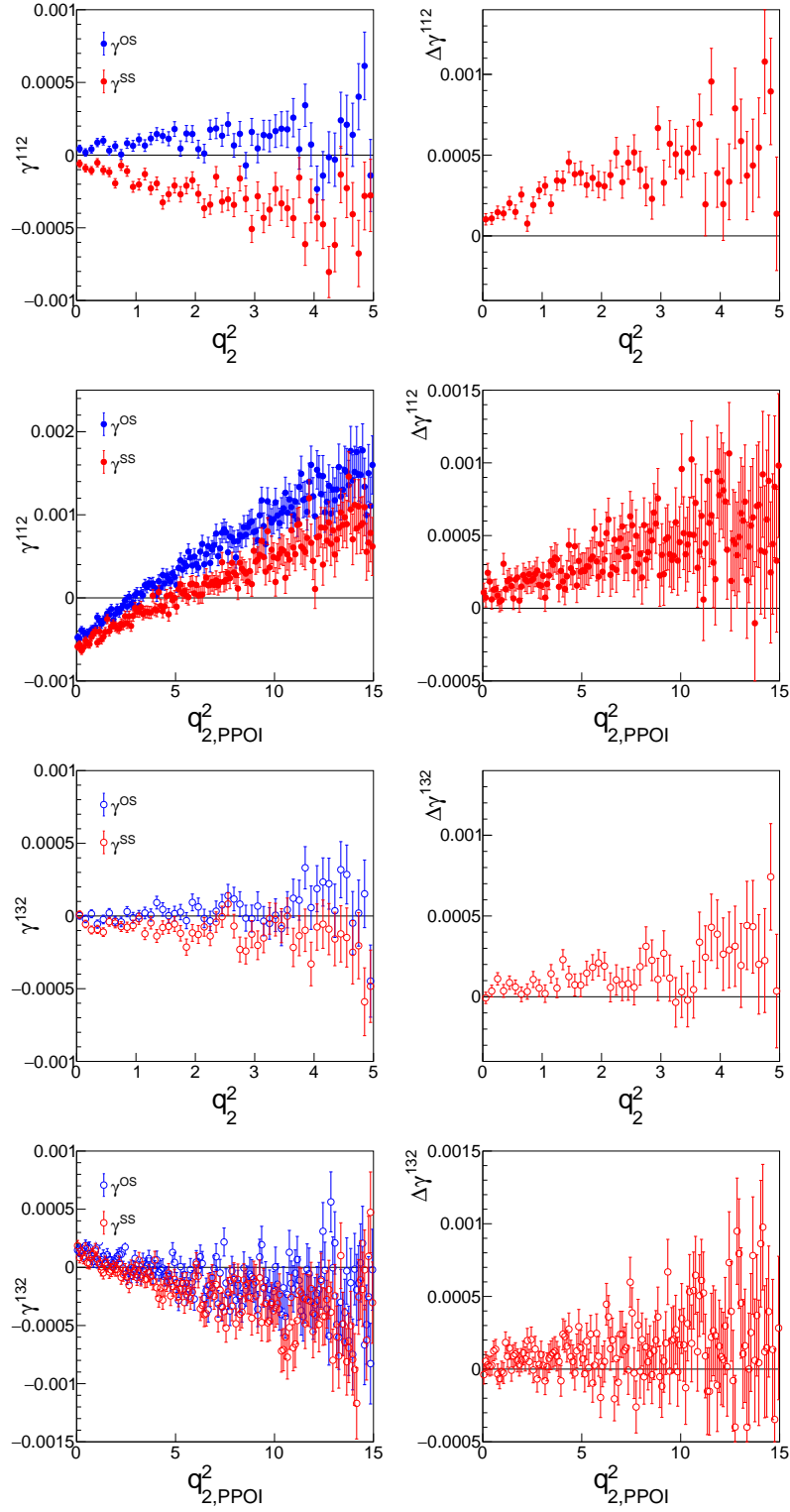
Figure 5.4: The observable $\Delta\gamma^{112}$ and the BKG-indicator $\Delta\gamma^{132}$ as a function of $q_2^2$ and $q_{2,\text{PPOI}}^2$ in 30–40% Au+Au at 19.6 GeV. Note that $\Delta\gamma = \gamma^{\text{OS}} - \gamma^{\text{SS}}$.

Based on the above measurement, we plot $\Delta\gamma^{112}$ against $v_2$ to extrapolate to the zero-flow ($v_2$) limit. The results, utilizing four different Event Shape Selection combinations, are shown in Fig. 5.5. The ESS provides a more effective lever arm for linear extrapolation. A descending order in the intercept values from ESS (a) to (d) for $\Delta\gamma^{112}$ is observed, similar to the trends seen in model simulations using AVFD and AMPT, and the intercepts of $\Delta\gamma^{112}$ remain positively finite. This observation is supportive of our successful suppression of the flow background in the CME measurement, with an expected ordering of intercepts.
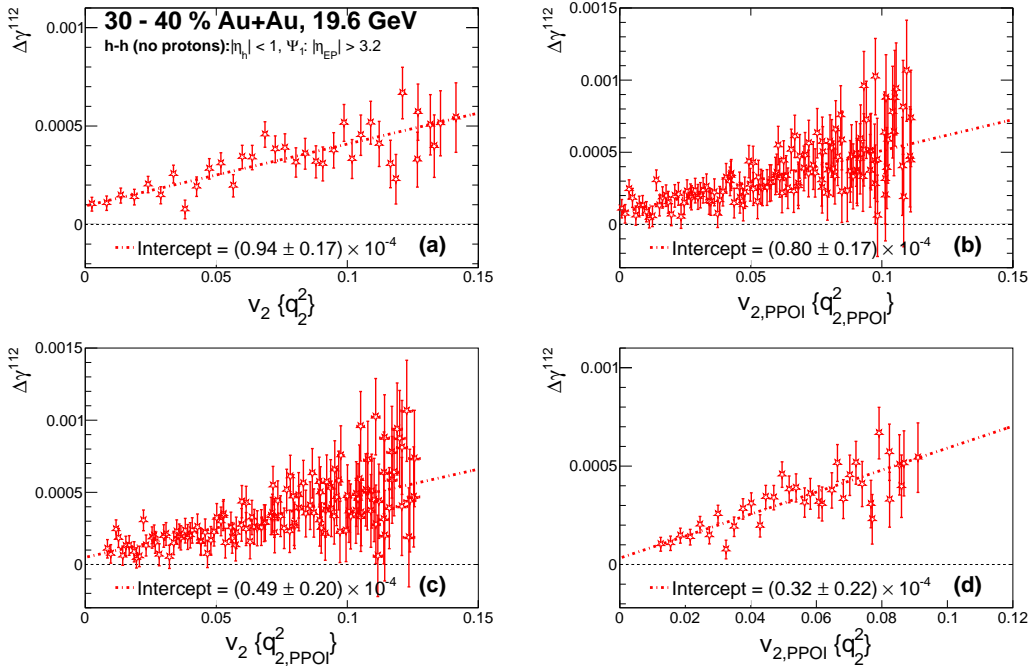


Figure 5.5: The four ESS combinations: $\Delta\gamma^{112}$ as a function of $v_2$ or $v_{2,\mathrm{PPOI}}$, categorized by $q_2^2$ or $q_{2,\mathrm{PPOI}}^2$ in 30–40% Au+Au at 19.6 GeV.

Furthermore, the comparison between $\Delta\gamma^{112}$ and background indicator $\Delta\gamma^{132}$ using optimal ESS combination (c) ($q_{2,\mathrm{PPOI}}^2$-$v_2$) is shown in Fig. 5.6. The data points have been rebinned by 2 for clarity in presentation, but the intercepts are derived directly from the data without any rebinning. With ESS, the intercept for the background indicator $\Delta\gamma^{132}$ is found to be consistent with zero, indicating that all the flow backgrounds are successfully mitigated. In comparison, at zero $v_2$, a finite intercept is observed for $\Delta\gamma^{112}$, indicating a
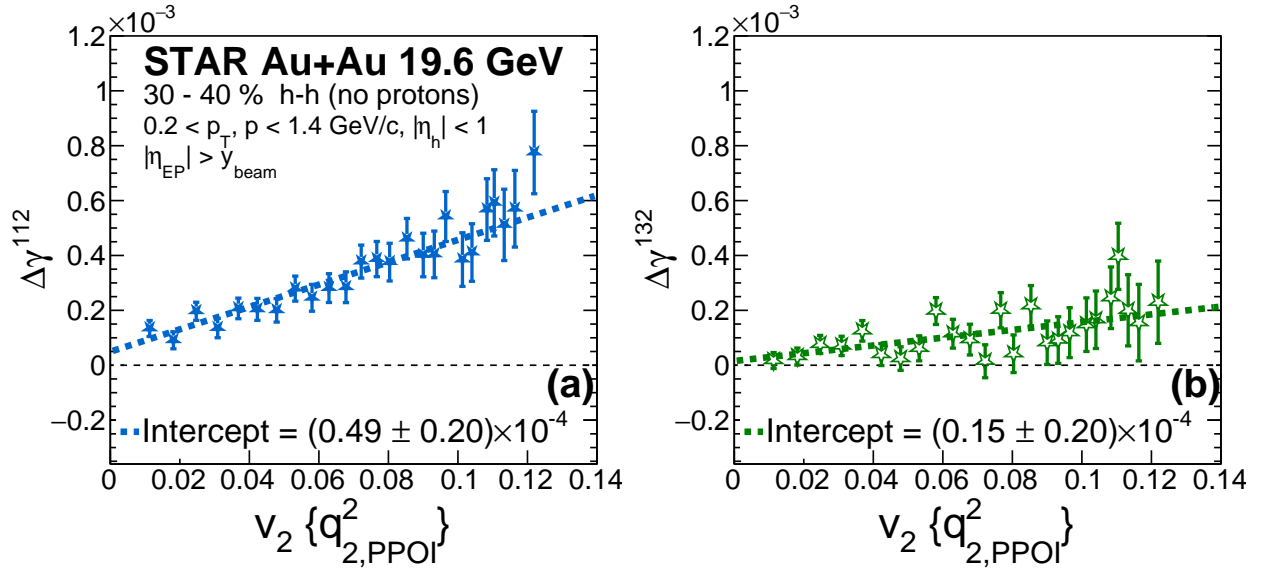
Figure 5.6: Comparison between $\Delta\gamma^{112}$ and $\Delta\gamma^{132}$ for ESS(c). The data points are rebinned by 5 for presentation. The intercept is obtained from data without any rebin.

non-trivial charge separation after background reduction.

To restore the unbiased CME signal, $\Delta\gamma^{112}_{\text{ESS}}$, the obtained intercept requires a correction based on the discussions in the previous chapter, as follows:

$$\Delta\gamma^{112}_{\text{ESS}} = \text{Intercept} \times (1 - v_2)^2. \tag{5.1}$$

### 5.2.1 Background check based on $v_{1,even}$

The definition of $\gamma^{112}$ incorporates the common background term $\langle v_1 v_1 \rangle$, which is expected to cancel out between opposite-sign (OS) and same-sign (SS) particle pairs. To ensure a thorough analysis, we also investigate the potential effects of momentum conservation arising from a non-zero $v_{1,even}$. Specifically, we examine the difference $\langle v_1 v_1 \rangle^{OS} - \langle v_1 v_1 \rangle^{SS}$ vs $q_2^2$, which could influence the $\Delta\gamma$ measurements when using the Event Shape Selection method. We find that the $v_{1,even}$ term is consistent with zero at all BES-II energies.

Figure 5.7 presents the measurements for the 20–50% centrality range of Au+Au collisions at 19.6 GeV, an illustrative example. The first column shows that the intercept of $v_{1,even}$
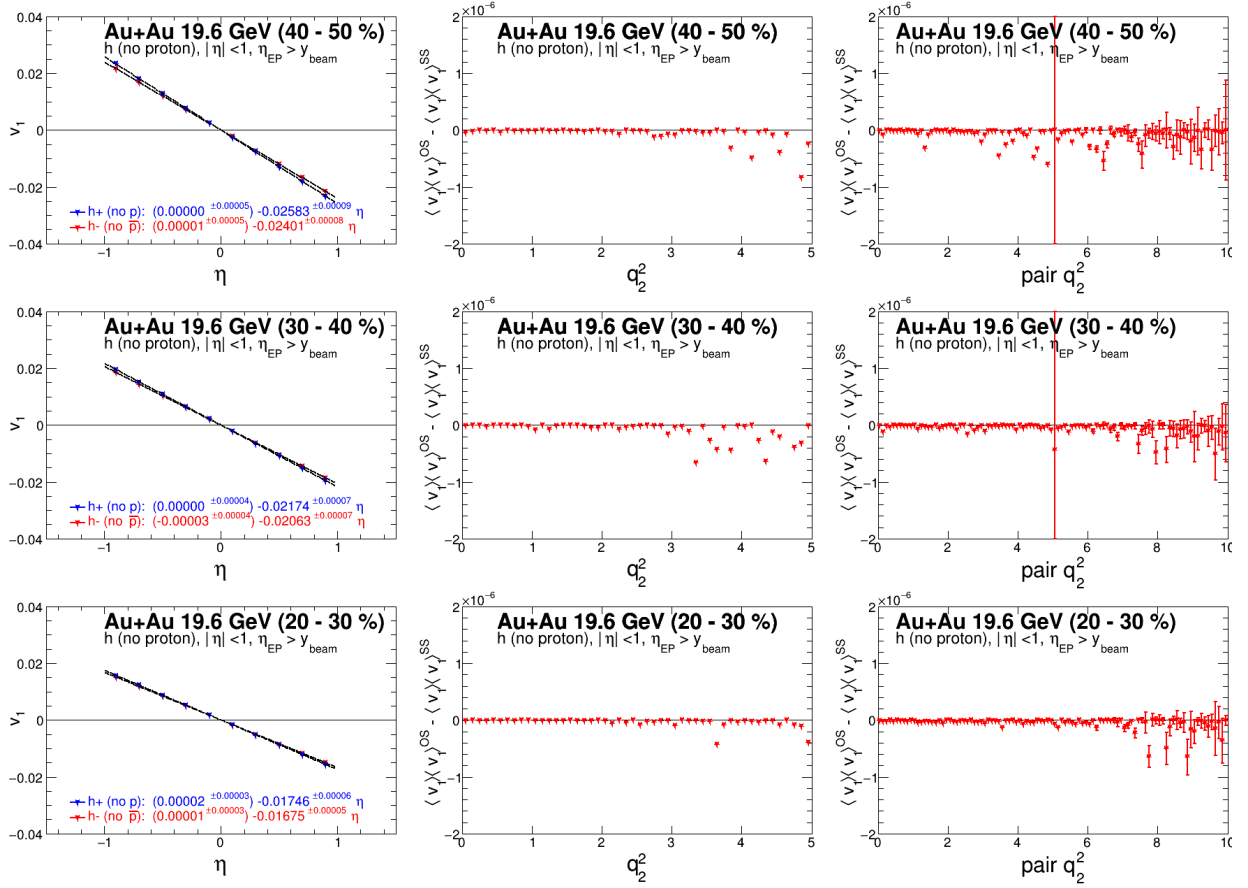
Figure 5.7: The check for $\langle v_1 v_1 \rangle^{\mathrm{OS}} - \langle v_1 v_1 \rangle^{\mathrm{SS}}$ in 20–50% Au+Au collisions at 19.6 GeV.

at $\eta = 0$ is consistent with zero for both positive and negative hadrons across the 20–30%, 30–40%, and 40–50% centrality ranges. The middle and right columns present the difference $\langle v_1 v_1 \rangle^{\mathrm{OS}} - \langle v_1 v_1 \rangle^{\mathrm{SS}}$ across different event shape variable $q_2^2$ bins. The measurements are consistent with zero, and their magnitude is at least two orders of magnitude (100 times) smaller than $\Delta \gamma \sim 10^{-5}$.

Based on these observations, we conclude that the effects of momentum conservation will not impact the $\Delta \gamma$ measurements at the BES-II.

## 5.3  Beam Energy Scan Results

The Chiral Magnetic Effect is anticipated to show a significant centrality dependence, because the magnetic field generated by spectator protons is most pronounced in peripheral collisions, while the QGP matter produced by participant nucleons is more prominent in central collisions, as indicated by the increasing number of participants ($N_{\text{part}}$). Therefore, we conduct the measurement at nine finer centrality ranges: 0–5%, 5–10%, 10–20%, 20–30%, 30–40%, 40–50%, 50–60%, 60–70%, 70–80% in Au+Au collisions.

In addition, the CME requires a strong magnetic field that may change with beam energy. At the lower energies, the rapid decay of the $B$ field could slow down. On the other hand, HBT measurements also suggest a decrease in the fireball size at energies down to 7.7 GeV. Consequently, it is imperative to analyze the beam energy dependence of the CME measurements within the BES-II datasets, ranging from 7 to 27 GeV, to better understand the CME dynamics.

We will first examine the measurement of inclusive observables, followed by an analysis of the results after background subtraction by utilizing the Event Shape Selection method.

### 5.3.1  BES-II ensemble average measurement

Figure 5.8 shows elliptic flow ($v_2$) measured for hadrons (excluding protons) with respect to the first-order EPD spectator plane in Au+Au collisions from 7.7 to 27 GeV in the BES-II. A strong centrality dependence is observed for elliptic flow at each energy. In the most central collisions, the initial eccentricity is expected to be smaller. In peripheral collisions, $v_2$ also drops and is significantly lower than measurements using the second-order participant plane from the TPC, indicating that using the spectator plane removes the nonflow effects that are most severe in peripheral collisions. $v_2$ also exhibits a strong monotonically decreasing trend with decreased beam energy in the 0–60% centrality range. This is because elliptic flow is pushed out by the pressure gradient from the QGP, which is smaller at lower energies with
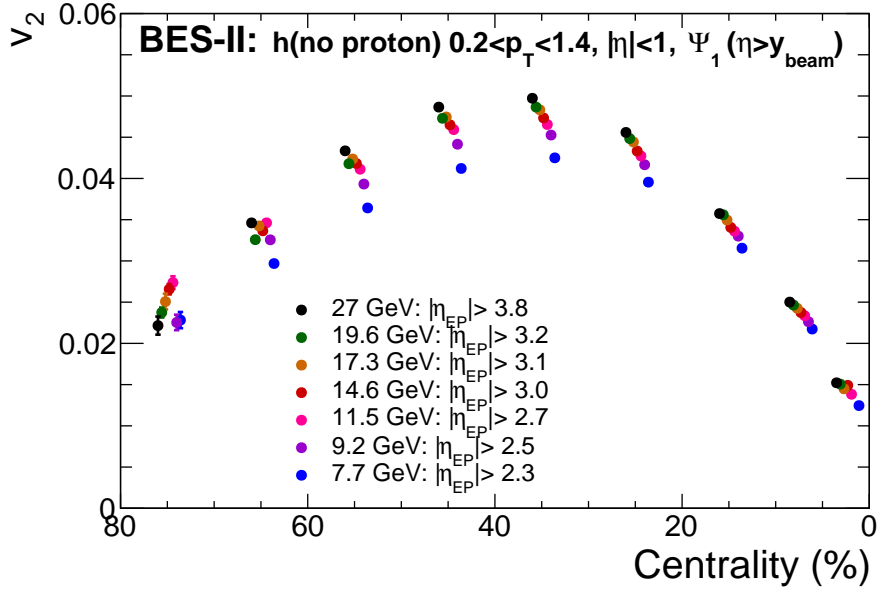
Figure 5.8: $v_2$ of hadrons (no proton) measured with EPD spectator plane $\Psi_1$ in BES-II

lower densities. At 70–80%, a reversed energy dependence trend is observed, which might indicate some interesting features to be understood.

$\gamma_{112}^{\text{OS}}$ (red) and $\gamma_{112}^{\text{SS}}$ (blue) measured using hadrons (excluding protons) with respect to the spectator plane in Au+Au collisions at BES-II energies are presented in Fig. 5.9. The overall trend is similar to the observed BES-I results [60], with nonflow effects successfully suppressed by using the spectator plane. The $\gamma_{112}^{\text{SS}}$ values are similar across different beam energies. The opposite-sign pair $\gamma_{112}^{\text{OS}}$ is observed to be higher than the same-sign pair $\gamma_{112}^{\text{SS}}$. In central collisions, both $\gamma_{112}^{SS}$ and $\gamma_{112}^{SS}$ are close to zero, while in peripheral collisions, the statistical uncertainties significantly increase, mainly because of the limited participants. However, we can not conclude on the CME based on the finite $\Delta\gamma^{112}$ in mid-central regions because there could still be flow backgrounds.

Figure 5.10 shows the corresponding $\gamma_{132}^{\text{OS}}$ and $\gamma_{132}^{\text{SS}}$ measurements at the BES-II energies. The opposite-sign pair $\gamma_{132}^{\text{OS}}$ is also observed to be higher than the same-sign pair $\gamma_{132}^{\text{SS}}$, in the mid-central centrality regionss from 10–60%. Thus, the background indicator $\Delta\gamma^{132}$ is finite,
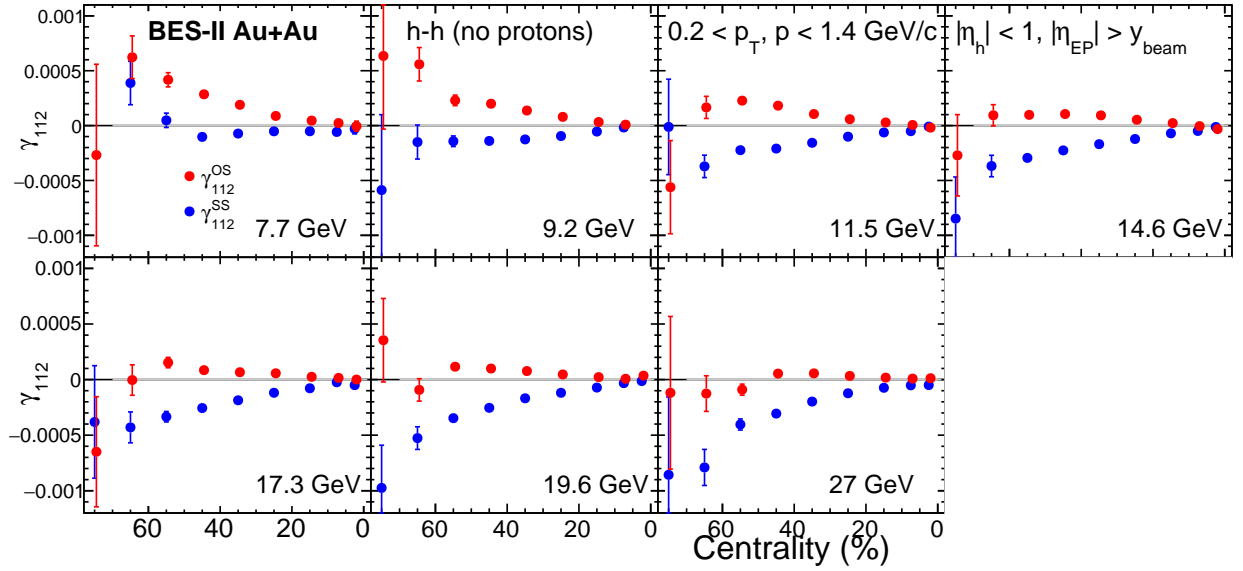
Figure 5.9: $\gamma_{112}^{OS}$ and $\gamma_{112}^{SS}$ of hadrons (no proton) measured with the EPD spectator plane $\Psi_1$ in the BES-II.
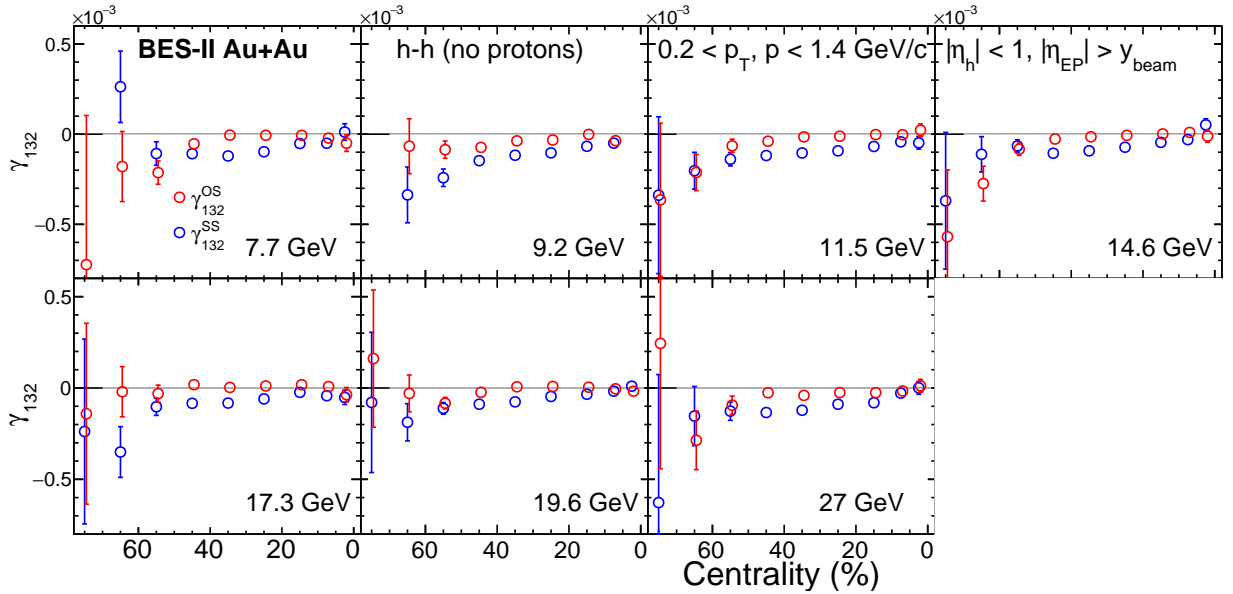


Figure 5.10: $\gamma_{132}^{OS}$ and $\gamma_{132}^{SS}$ of hadrons (no protons) measured with the EPD spectator plane $\Psi_1$ in the BES-II.

suggesting that the flow contribution in the inclusive observable needs to be subtracted.

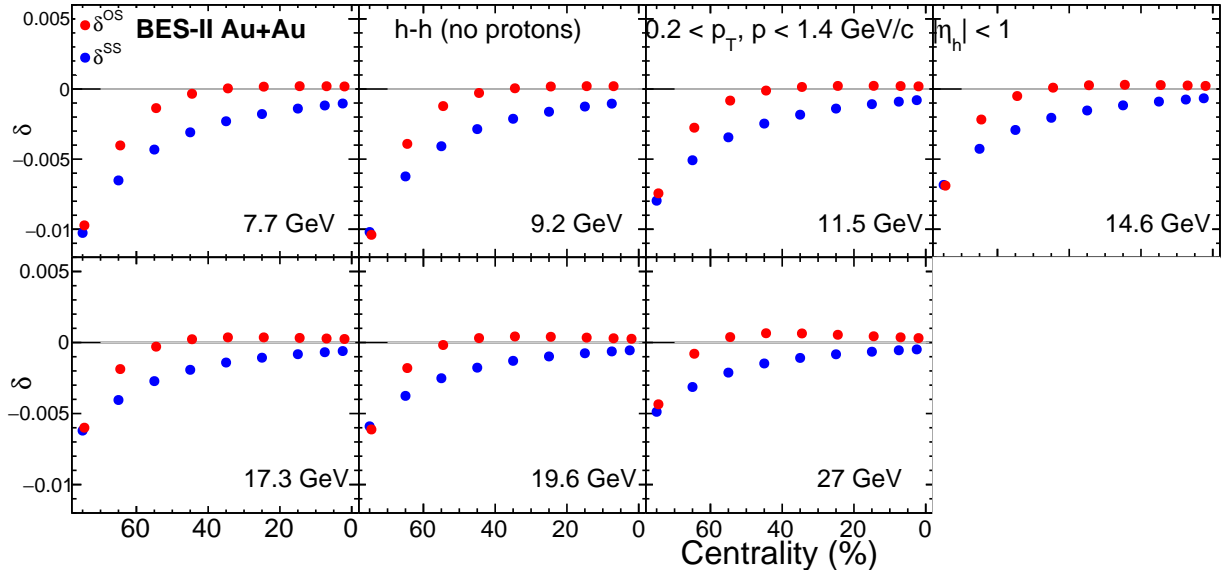Furthermore, we present the two-particle correlation $\delta^{OS}$ and $\delta^{SS}$ measured at the BES-II

Figure 5.11: $\delta^{\mathrm{OS}}$ and $\delta^{\mathrm{SS}}$ of hadrons (no proton) in the BES-II.

energies in Fig. 5.11. The results are similar to those from the BES-I, but with much better statistics. By taking the difference, we observe finite $\Delta\delta$ in mid-central collisions, indicating finite background contributions to the $\Delta\gamma^{112}$ measurement due to its coupling with elliptic flow.

In the following, we will discuss the application of Event Shape Selection method to suppress the flow-related backgrounds.

### 5.3.2  ESS at BES-II from 7.7 to 27 GeV

The Event Shape Selection method is applied to the BES-II measurements for the 9 fine centrality bins. To compensate for the dilution effect from participants, $N_{\text{part}}$ will be multiplied at each centrality for a fair comparison. The $N_{\text{part}}$ values at each centrality at the BES-II are obtained from the MC Glauber Model calculation (see discussion in Sec. 2.3.2), and are listed in Table 5.1.

Table 5.1: $N_{\text{part}}$ for each centrality in Au+Au collisions at the BES-II.

| $\sqrt{s_{NN}}$ | 7.7 GeV | 9.2 GeV | 11.5 GeV | 14.6 GeV | 17.3 GeV | 19.6 GeV | 27 GeV |
|---|---|---|---|---|---|---|---|
| 70-80% | 14.51 | 13.58 | 13.74 | 13.80 | 14.14 | 14.63 | 14.36 |
| 60-70% | 26.29 | 26.01 | 26.08 | 26.13 | 25.90 | 26.94 | 26.29 |
| 50-60% | 45.03 | 45.40 | 44.85 | 45.29 | 44.69 | 45.72 | 45.08 |
| 40-50% | 71.67 | 72.79 | 72.11 | 72.15 | 72.26 | 73.12 | 72.96 |
| 30-40% | 108.96 | 109.82 | 109.32 | 109.60 | 109.70 | 110.16 | 110.51 |
| 20-30% | 158.37 | 158.78 | 158.14 | 159.76 | 159.53 | 159.76 | 160.34 |
| 10-20% | 224.33 | 224.17 | 223.44 | 225.83 | 226.39 | 225.28 | 226.86 |
| 5-10% | 288.45 | 288.00 | 286.79 | 289.49 | 289.97 | 289.41 | 291.23 |
| 0-5% | 336.22 | 336.18 | 337.02 | 339.41 | 338.71 | 340.18 | 339.82 |

Therefore, we compare $N_{\text{part}}\langle\Delta\gamma^{112}\rangle$ with the four ESS results after background subtraction, $N_{\text{part}}\Delta\gamma^{112}_{\text{ESS}}$, in 0–80% centrality Au+Au collisions at the BES-II. Similarly, the background indicator $N_{\text{part}}\langle\Delta\gamma^{132}\rangle$ is compared with the four ESS results of $N_{\text{part}}\Delta\gamma^{132}_{\text{ESS}}$. Then, the ratio $\Delta\gamma^{112}_{\text{ESS}}/\langle\Delta\gamma^{112}\rangle$ at each centrality bin is also calculated to understand the fraction of the remaining charge separation in $\Delta\gamma^{112}$ after flow background subtraction.

Figure 5.12 shows the results at 27 GeV. In the first panel, we observe that the ESS $\Delta\gamma^{112}_{\text{ESS}}$ values from the four intercepts, after flow background subtraction, are significantly lower than the inclusive $\langle\Delta\gamma^{112}\rangle$ (red) for mid-central collisions. This indicates an effective
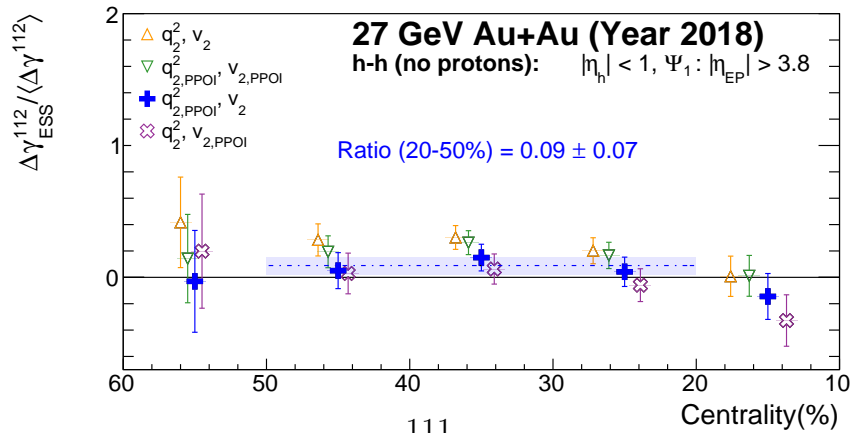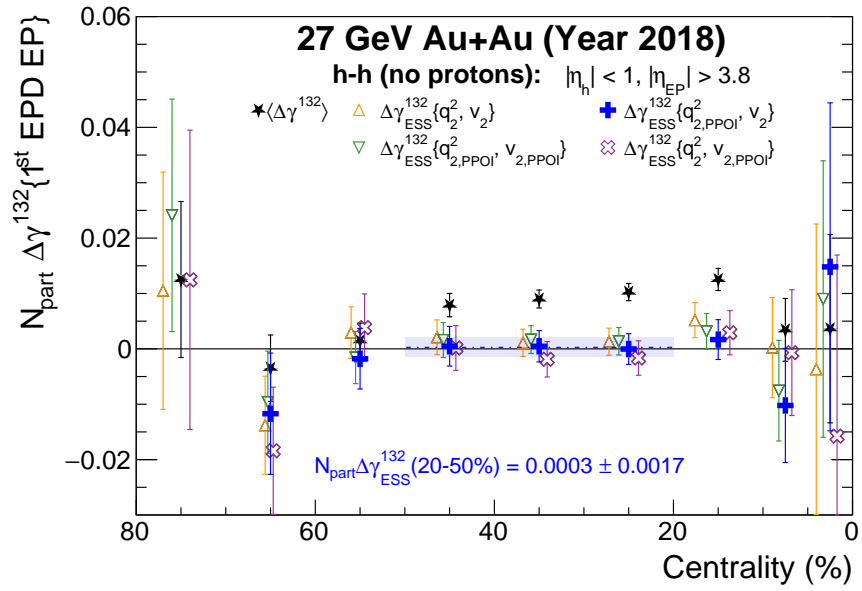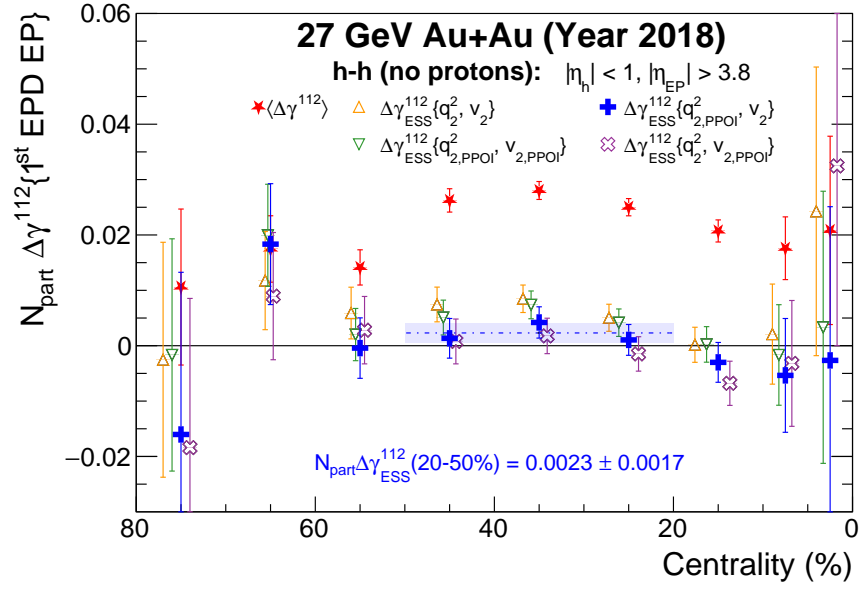
Figure 5.12: ESS results in Au+Au collisions at $\sqrt{s_{NN}} = 27$ GeV.

background suppression. The four ESS measurements (a)–(d) show a descending trend with some positively finite values in mid-central regions.

In the most central and peripheral collisions, the statistical errors are large, and the results are consistent with zero. Fitting $N_{\text{part}}\Delta\gamma_{\text{ESS}}^{112}$ from the optimal ESS (c) over the 20–50% region yields a positive value of 1.3 $\sigma$ above zero, which is statistically consistent with zero.

In the second panel, the background indicator $\Delta\gamma_{\text{ESS}}^{132}$ with ESS(a) (yellow triangle) and ESS(b) (green triangle) suggests a residual background, as previously discussed, from the self-correlation in these two combinations. The optimal Event Shape Selection, ESS(c) (blue cross), shows $\Delta\gamma_{\text{ESS}}^{132}$ values consistent with zero, indicating effective background removal. In contrast, ESS(d) (purple cross) results are lower than those for ESS(c), suggesting a possible over-subtraction. A fitting for the optimal ESS (c) over the 20–50% range for $N_{\text{part}}\Delta\gamma_{\text{ESS}}^{132}$ renders a result consistent with zero, indicating the successful subtraction of the flow background.

The ratio $\Delta\gamma_{\text{ESS}}^{112}/\langle\Delta\gamma^{112}\rangle$, presented in the bottom panel, allows us to assess the remaining charge separation after flow background subtraction via ESS. Fitting the 20–50% region indicates that the ratio is approximately $8.9 \pm 6.5(stat.)\%$. This finding at 27 GeV aligns with other STAR measurements at the same energy [70], which did not observe any definitive result due to the statistical uncertainty. The large statistical uncertainty at 27 GeV is caused by the restricted $\eta$ coverage of the EPD in the spectator region at this energy, which results in relatively lower event plane resolutions, as shown in Fig. 4.14. Going towards lower energies, the EPD coverage in the spectator region is enhanced.

The results at 19.6 GeV are shown in Fig. 5.13. In the first panel, similar to 27 GeV, we observe a finite remaining charge separation after using the Event Shape Selection to suppress the flow background. The peripheral and central collisions are consistent with zero, albeit with substantial uncertainties. A fitting of $N_{\text{part}}\Delta\gamma_{\text{ESS}}^{112}$ from the optimal ESS (c) over the 20–50% region reveals a substantially positive signal with a $3.47\sigma$ significance. In
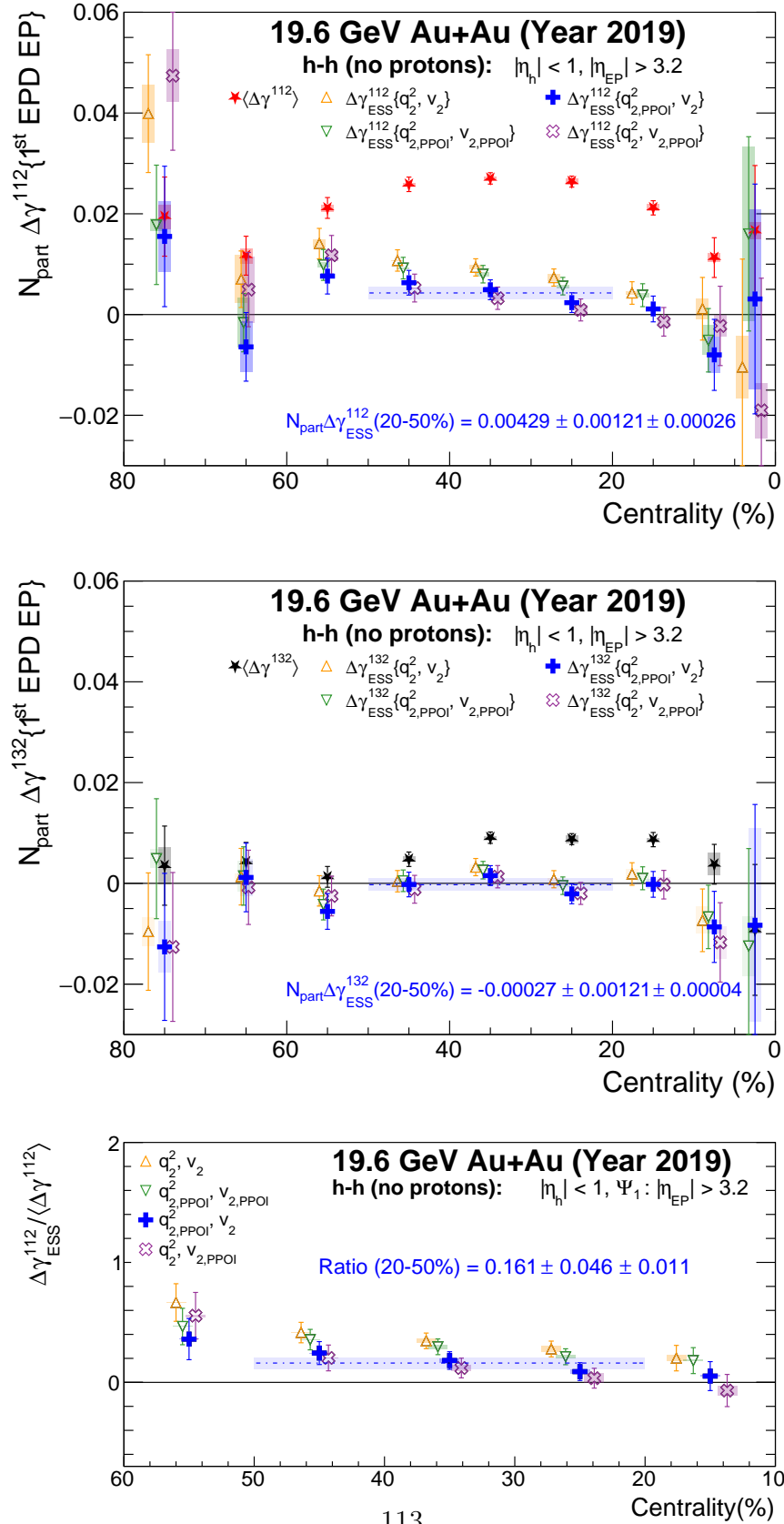
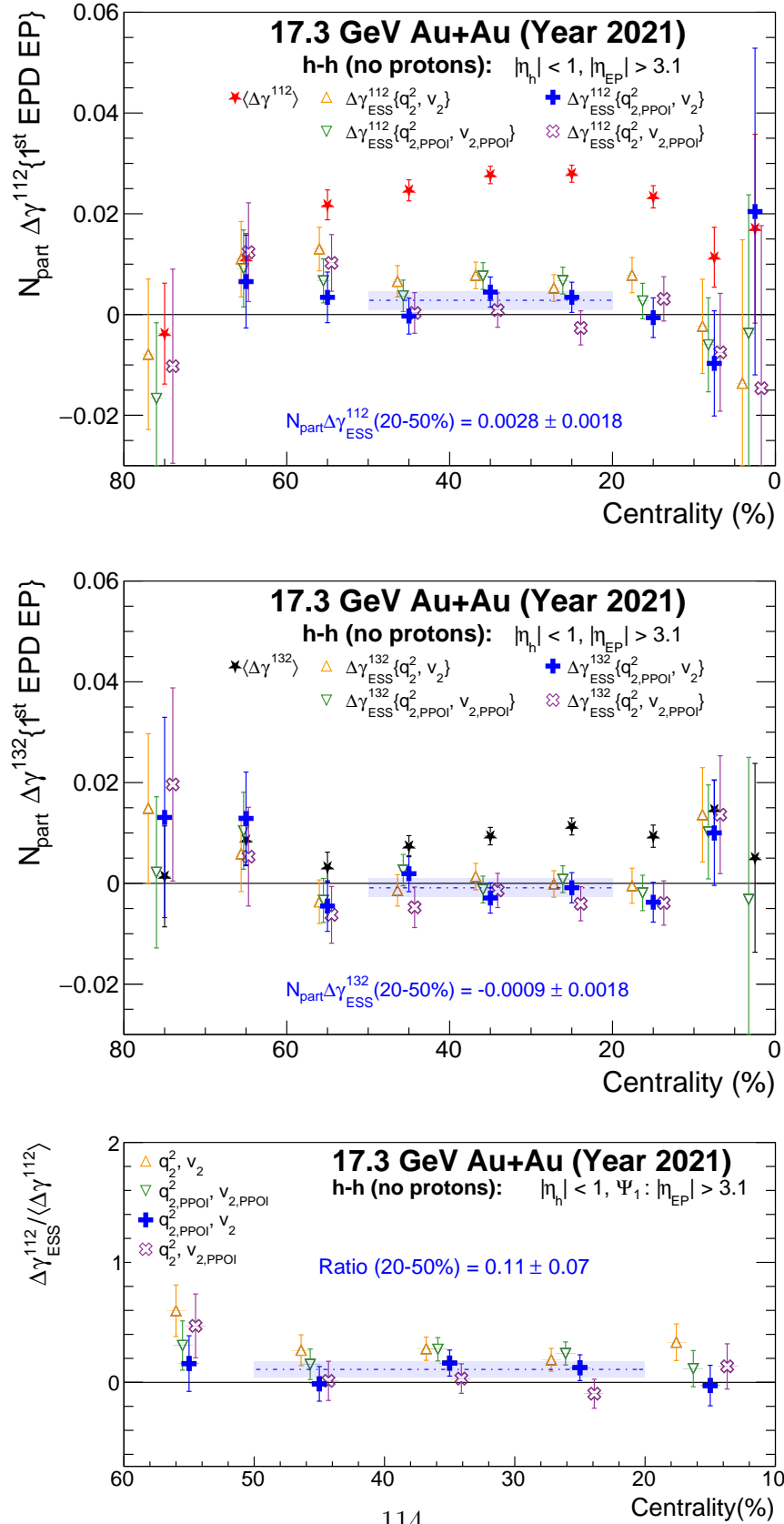Figure 5.13: ESS results in Au+Au collisions at $\sqrt{s_{NN}} = 19.6$ GeV.

Figure 5.14: ESS results in Au+Au collisions at $\sqrt{s_{NN}} = 17.3$ GeV.

contrast, the fitting of $N_{\mathrm{part}}\Delta\gamma_{\mathrm{ESS}}^{132}$ over the same range is consistent with zero. This suggests that a non-trivial charge separation was found at 19.6 GeV, in the aftermath of suppression of flow and nonflow backgrounds.

The ratio in the 20–50% centrality region indicates that the remaining charge separation is about 16% with a $3.5\sigma$ significance in Au+Au at 19.6 GeV.

The results at 17.3 GeV are displayed in Fig. 5.14. In the first panel, there is an observable finite remaining charge separation, while results from peripheral and central collisions align with zero. A fitting of $N_{\mathrm{part}}\Delta\gamma_{\mathrm{ESS}}^{112}$ from the optimal ESS (c) across the 20–50% region shows a positive signal with only a $1.5\sigma$ significance. A similar fitting of $N_{\mathrm{part}}\Delta\gamma_{\mathrm{ESS}}^{132}$ in the same range is consistent with zero. The ratio in the 20–50% range indicates that the remaining charge separation is $11 \pm 7(stat.)\%$, which is statistically consistent with zero in Au+Au collisions at 17.3 GeV. The large statistical uncertainties at this energy are primarily due to the limited total event numbers, which are half of those at 19.6 GeV.

The results at 14.6 GeV are displayed in Fig. 5.15. In the first panel, we observe a finite remaining charge separation in the mid-central regions. A fitting of $N_{\mathrm{part}}\Delta\gamma_{\mathrm{ESS}}^{112}$ from the optimal ESS (c) across the 20–50% range shows a finite signal with a $3.12\sigma$ significance. Conversely, a similar fitting of $N_{\mathrm{part}}\Delta\gamma_{\mathrm{ESS}}^{132}$ in the same range is consistent with zero. The ratio at 14.6 GeV in the 20–50% range indicates that the remaining charge separation is around 16% with a $3.1\sigma$ significance, similar to the 19.6 GeV results.

The results at 11.5 GeV are displayed in Fig. 5.16. In the first panel, we observe a finite remaining charge separation in the mid-central regions. A fitting of $N_{\mathrm{part}}\Delta\gamma_{\mathrm{ESS}}^{112}$ from the optimal ESS (c) across the 20–50% range shows a finite signal with a $3.29\sigma$ significance. Conversely, a similar fitting of $N_{\mathrm{part}}\Delta\gamma_{\mathrm{ESS}}^{132}$ in the same range is consistent with zero. The ratio at 11.5 GeV in the 20–50% range indicates that the remaining charge separation is around 16% with a $3.5\sigma$ significance, similar to the 19.6 GeV results.

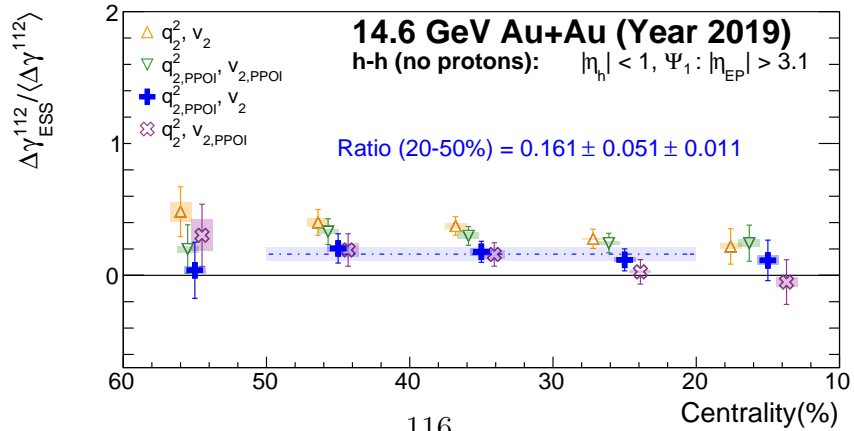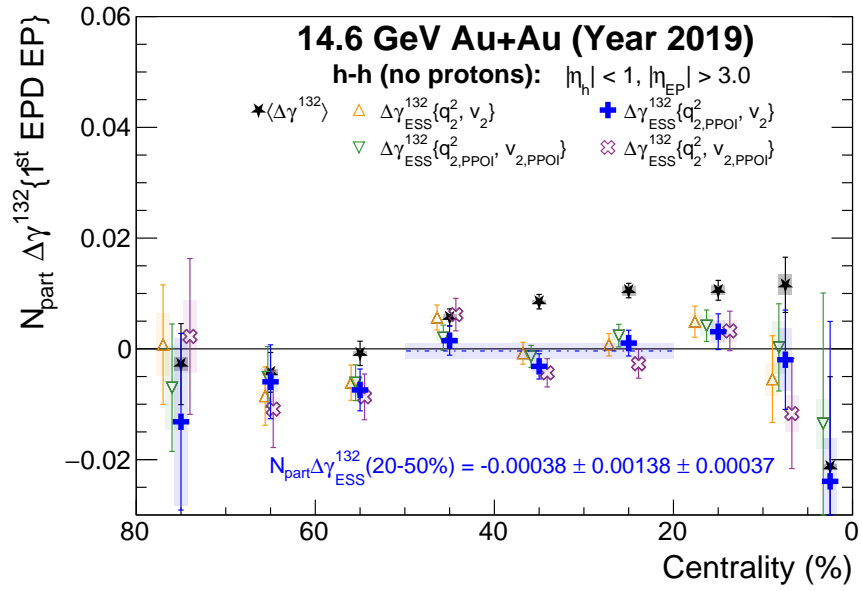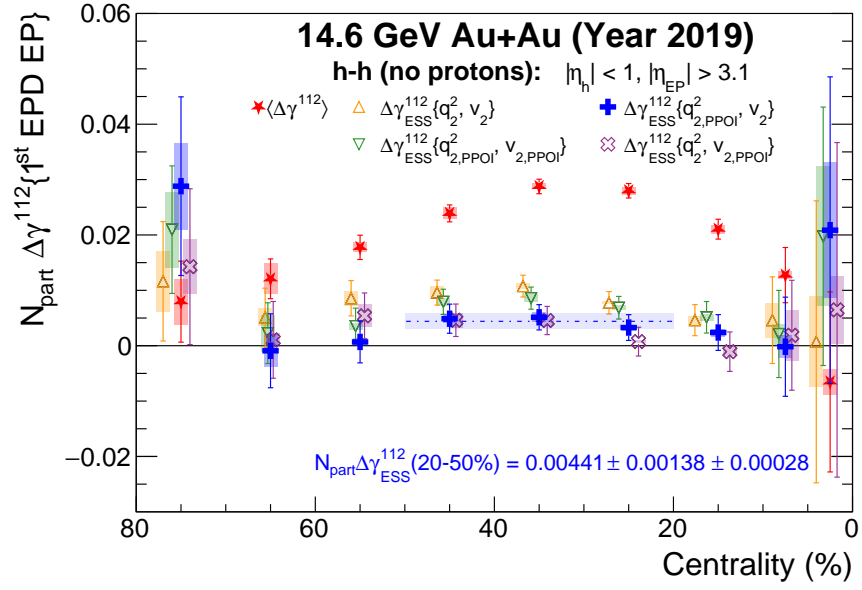The results at 9.2 GeV are shown in Fig. 5.17. In the first panel, the remaining charge

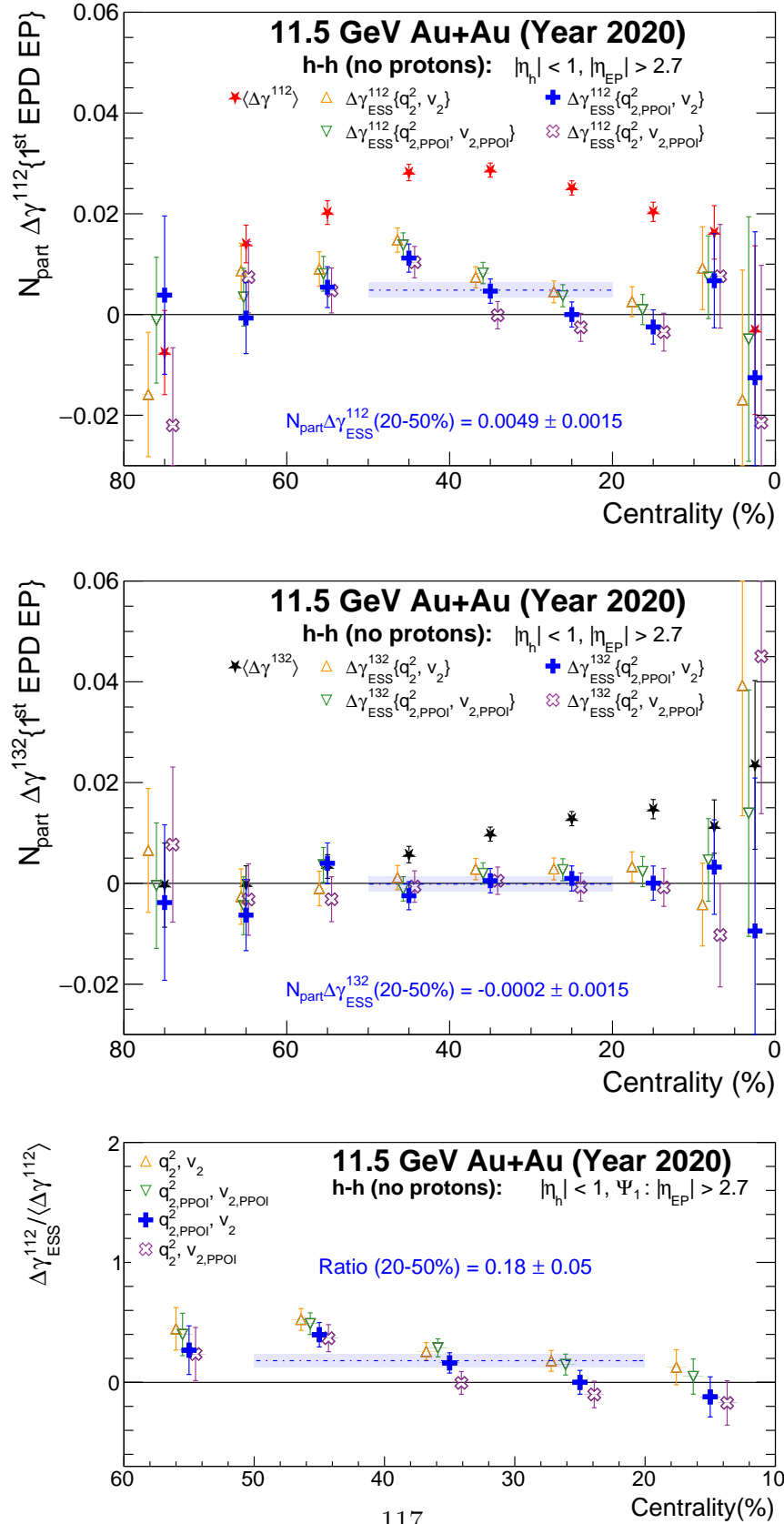Figure 5.15: ESS results in Au+Au collisions at $\sqrt{s_{NN}} = 14.6$ GeV.

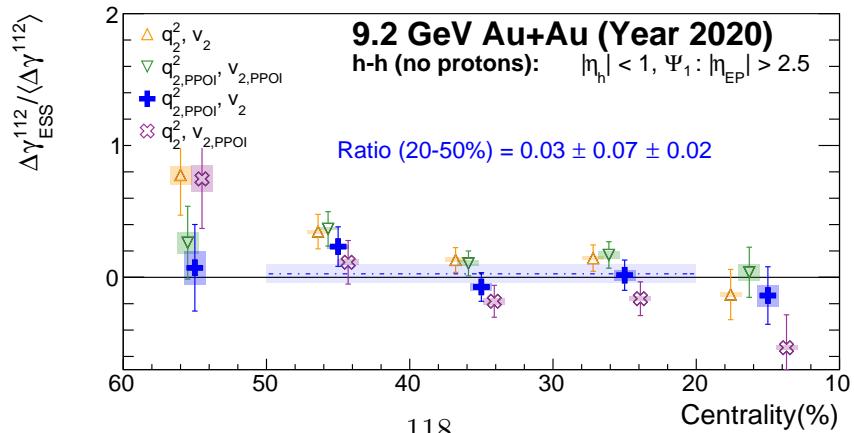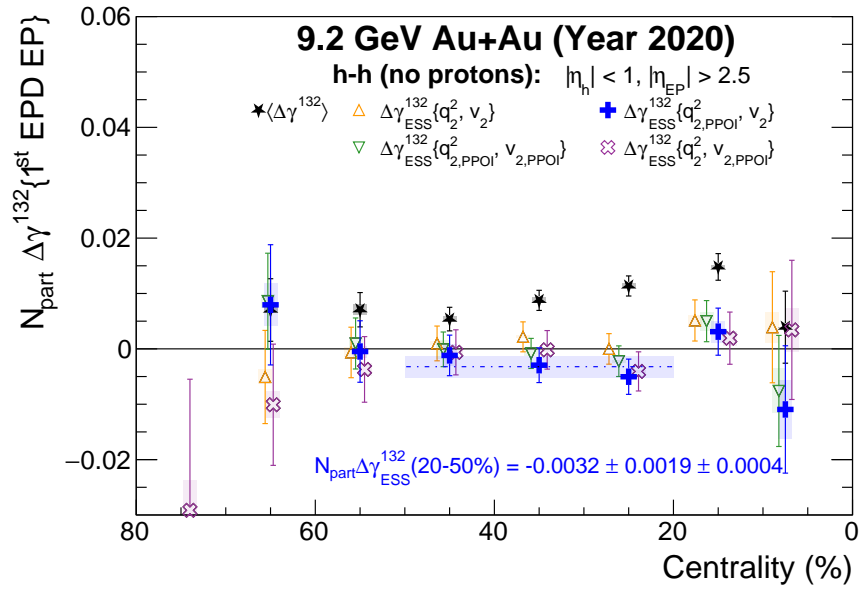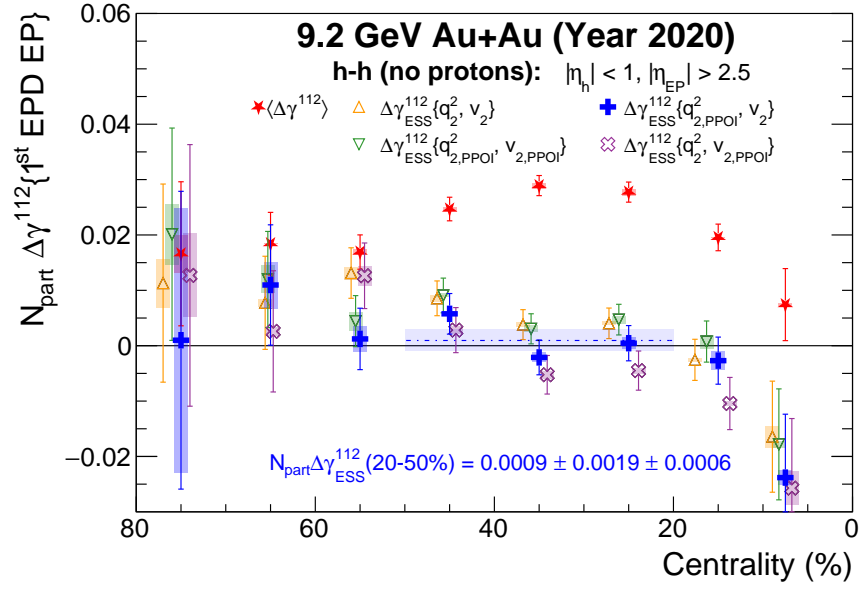Figure 5.16: ESS results in Au+Au collisions at $\sqrt{s_{NN}} = 11.5$ GeV.

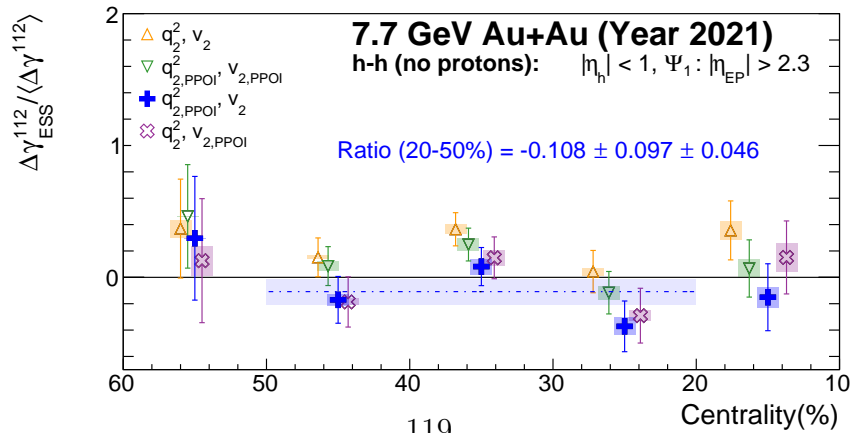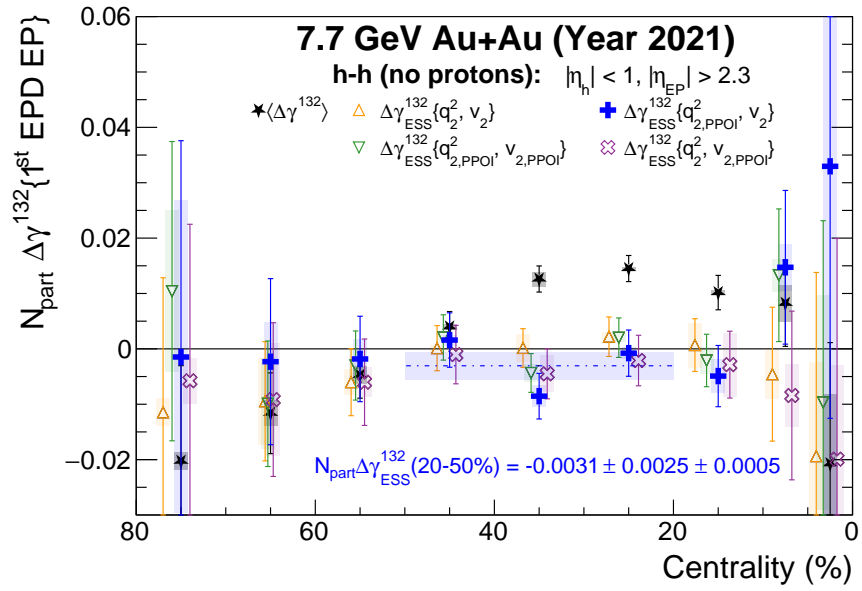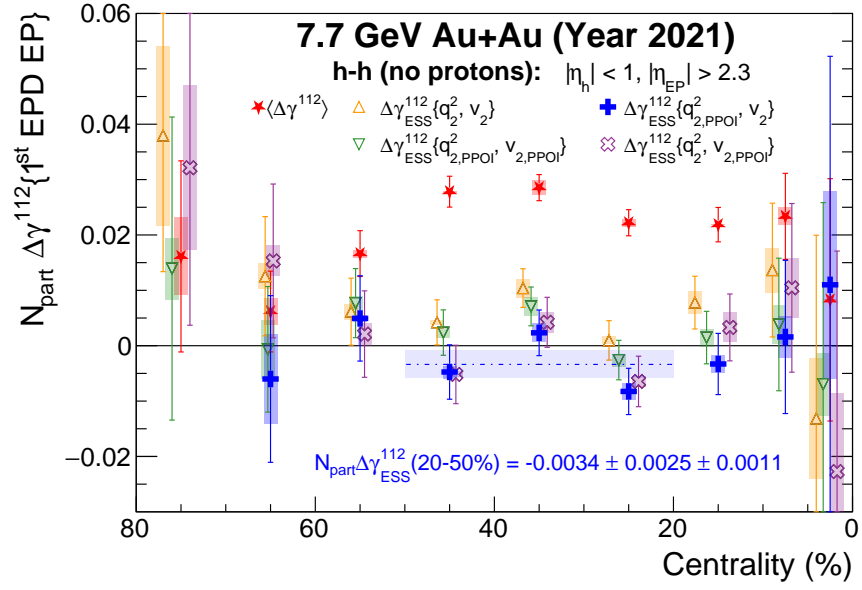Figure 5.17: ESS results in Au+Au collisions at $\sqrt{s_{NN}} = 9.2$ GeV.

Figure 5.18: ESS results in Au+Au collisions at $\sqrt{s_{NN}} = 7.7$ GeV.

separation in the mid-central 20–50% region for $N_{\text{part}}\Delta\gamma_{\text{ESS}}^{112}$ following Event Shape Selection is consistent with zero. However, the results from the most central and peripheral collisions display large statistical uncertainties. A similar fitting of $N_{\text{part}}\Delta\gamma_{\text{ESS}}^{132}$ in the same range shows a negative value with a $1.8\sigma$ significance. At 9.2 GeV, the ratio in the 20–50% range suggests that the remaining charge separation after flow background subtraction is $2 \pm 7(stat.)\%$, statistically consistent with zero.

The results at 7.7 GeV are shown in Fig. 5.18. In the first panel, the remaining charge separation in the mid-central 20–50% region for $N_{\text{part}}\Delta\gamma_{\text{ESS}}^{112}$ is consistent with zero, with large statistical uncertainties. A similar fitting for $N_{\text{part}}\Delta\gamma_{\text{ESS}}^{132}$ in the same range also yields results consistent with zero, after the flow background suppression. At 7.7 GeV, the ratio in the 20–50% region suggests that the remaining charge separation after flow background subtraction is $-10.8 \pm 9.7(stat.) \pm 4.6(syst.)\%$, statistically consistent with zero.

The substantial statistical uncertainties observed at 7.7 GeV are caused by the limited data collected at this energy level, as managing a low-energy beam at RHIC is typically quite challenging.

Based on the detailed centrality dependence above at each BES-II energy, we will next explore the beam energy dependence of the CME measurements in the following section.

## 5.4   Beam Energy Dependence of $\Delta\gamma^{112}_{\mathrm{ESS}}$
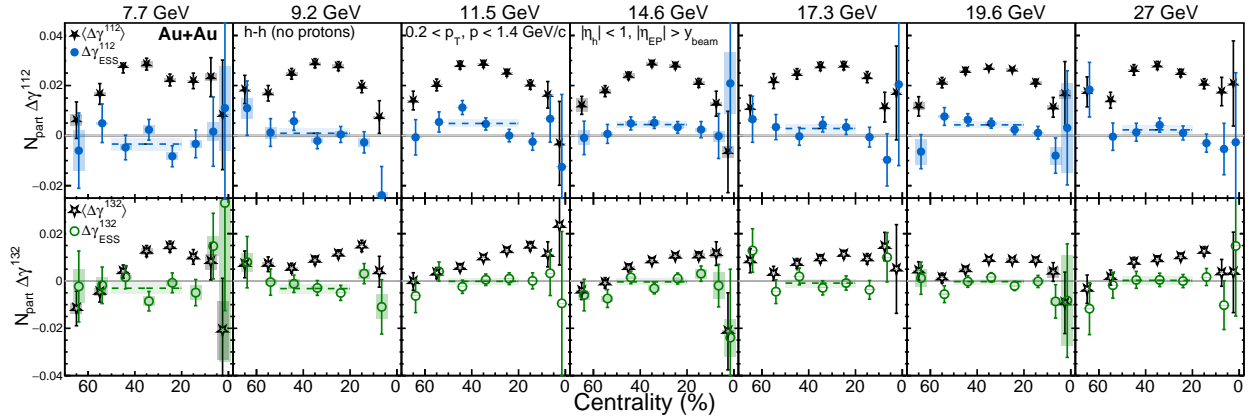


Figure 5.19: Centrality dependence of $\Delta\gamma^{112}_{\mathrm{ESS}}$ (blue) in contrast to inclusive $\Delta\gamma^{112}$ (black), and open markers shows $\Delta\gamma^{132}_{\mathrm{ESS}}$ (green) in contrast to inclusive $\Delta\gamma^{132}$ (black) in Au+Au collisions from 7.7 to 27 GeV.

The results of the background indicator ($\Delta\gamma^{132}_{\mathrm{ESS}}$) have shown that flow background contributions are mitigated using optimal ESS approaches. Additionally, by utilizing the spectator plane, we have suppressed nonflow contributions to the $\Delta\gamma$ observables. These results are summarized in Fig. 5.19 for Au+Au collisions collected in the BES-II from 7.7 to 27 GeV.

The first row of the figure contrasts the centrality dependence of the ensemble average observable $N_{\mathrm{part}}\langle\Delta\gamma^{112}\rangle$ (black solid) with the optimal ESS results of $N_{\mathrm{part}}\Delta\gamma^{112}_{\mathrm{ESS}}$ (blue). The second row compares the background indicator $N_{\mathrm{part}}\langle\Delta\gamma^{132}\rangle$ (black open) to $N_{\mathrm{part}}\Delta\gamma^{132}_{\mathrm{ESS}}$ (green).

Given the multiplicities at these lower RHIC energies, the inclusive $N_{\mathrm{part}}\langle\Delta\gamma^{112}\rangle$ displays a similar pattern and magnitude across the BES-II. In the aftermath of flow background subtraction, the ESS results ($N_{\mathrm{part}}\Delta\gamma^{112}_{\mathrm{ESS}}$) reveal an interesting beam energy dependence. While the results in the most central and peripheral collisions are consistent with zero, the mid-central events (20–50%) exhibit a positive value with a significance higher than $3\sigma$ at some energies. In contrast, the background indicator, $N_{\mathrm{part}}\Delta\gamma^{132}_{\mathrm{ESS}}$, remains consistent with zero at all energies.
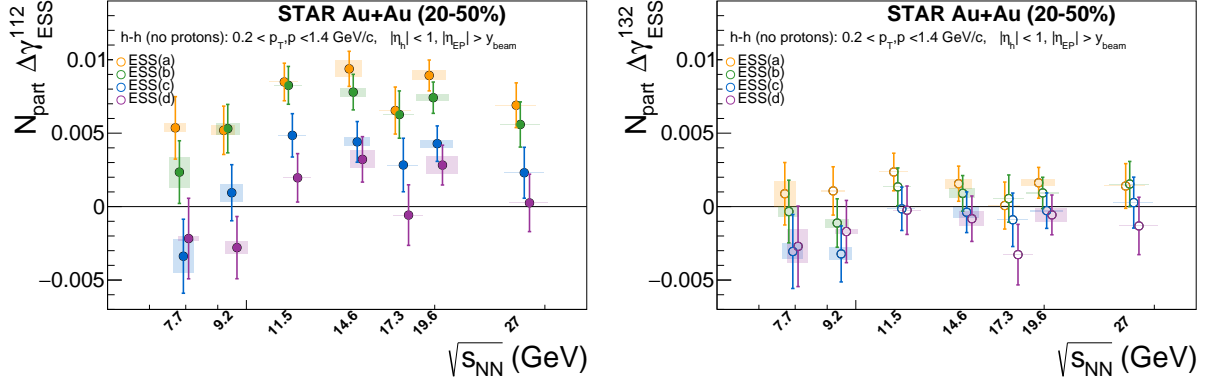
Figure 5.20: Beam Energy dependence of the four ESS recipes for (left) $\Delta\gamma_{\text{ESS}}^{112}$ and (right) $\Delta\gamma_{\text{ESS}}^{132}$ in 20–50% Au+Au collisions from 7.7 to 27 GeV.

After combining the 20–50% centrality range, the beam energy dependence of the four Event Shape Selection results are compared in Fig 5.20. A descending order for the ESS recipes is observed across the different energy levels, and for both $N_{\text{part}}\Delta\gamma_{\text{ESS}}^{112}$ and $N_{\text{part}}\Delta\gamma_{\text{ESS}}^{132}$. The right panel displays the background indicator $N_{\text{part}}\Delta\gamma_{\text{ESS}}^{132}$ following flow background subtraction and confirms that the optimal recipe, ESS (c), effectively mitigates the flow background. On the other hand, the other three ESS recipes are found to be less accurate, albeit statistical uncertainties are large.

The beam energy dependence of the CME-related observables is illustrated in Fig. 5.21 for 20–50% Au+Au collisions at the BES-II with beam energies from 7.7 to 27 GeV. In the upper panel, the inclusive $N_{\text{part}}\langle\Delta\gamma^{112}\rangle$ (black) is compared to $N_{\text{part}}\Delta\gamma^{112}$ESS (blue) and $N\text{part}\Delta\gamma_{\text{ESS}}^{132}$ (green). The background indicator, $\Delta\gamma_{\text{ESS}}^{132}$, is consistent with zero across all energies, validating the ESS method's effectiveness. While the ensemble average $N\text{part}\langle\Delta\gamma^{112}\rangle$ remains relatively constant, $\Delta\gamma_{\text{ESS}}^{112}$ shows a positively finite charge separation at 11.5, 14.6, and 19.6 GeV, with significance levels of 3.29$\sigma$, 3.12$\sigma$, and 3.47$\sigma$, respectively. $\Delta\gamma_{\text{ESS}}^{112}$ is consistent with zero at $\sqrt{s_{NN}} =$ 7.7 and 9.2 GeV. The large uncertainties at 17.3 and 27 GeV prevent definitive conclusions.

The lower panel depicts the ratio of $\Delta\gamma_{\text{ESS}}^{112}$ to inclusive $\langle\Delta\gamma^{112}\rangle$, revealing that the flow background contributes at least 80% to the latter. The observed energy dependence favors
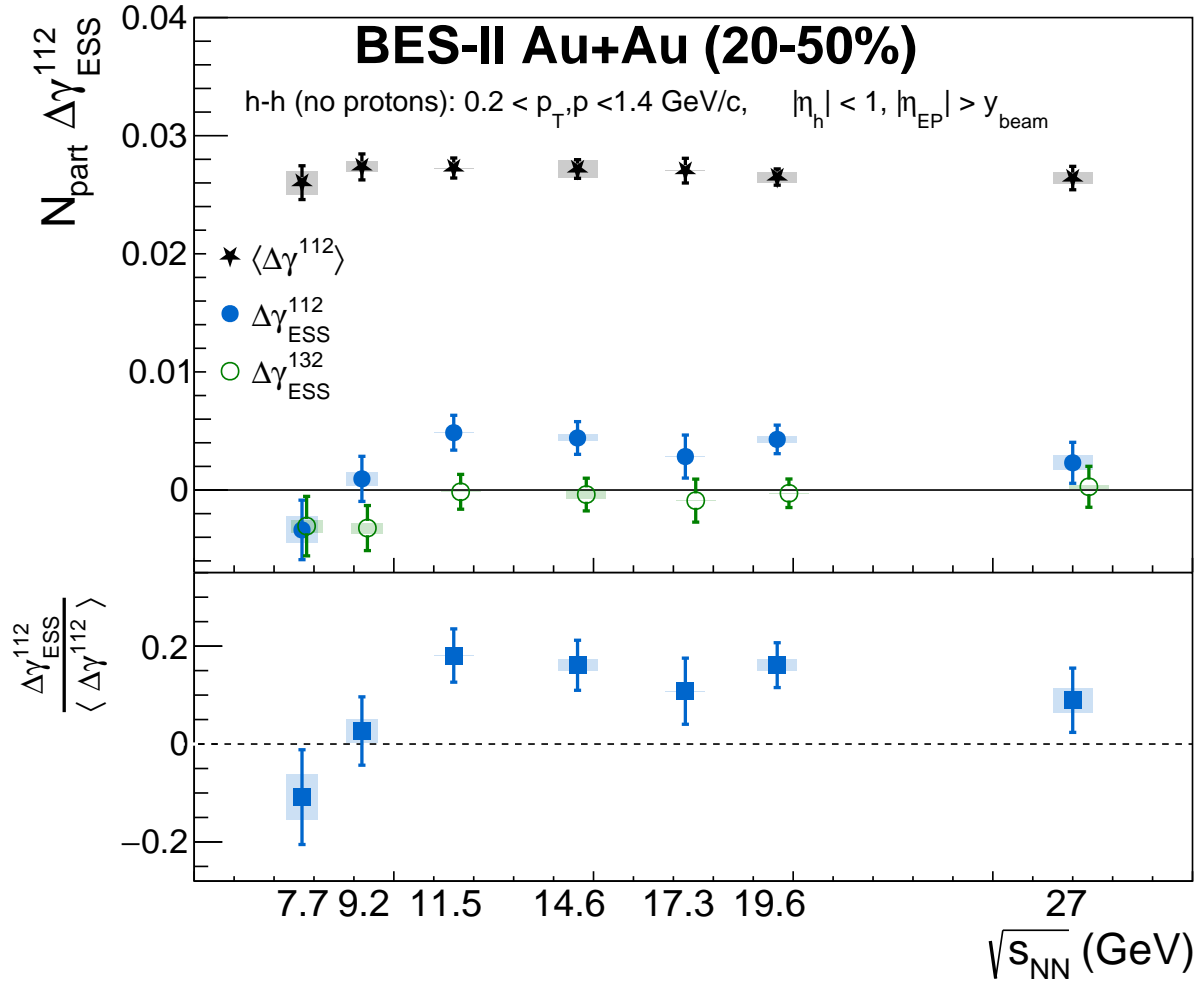
Figure 5.21: (Upper) Beam energy dependence of $\Delta\gamma^{112}_{\mathrm{ESS}}$ (blue) in contrast to inclusive $\Delta\gamma^{112}$ (black), $\Delta\gamma^{132}_{\mathrm{ESS}}$ (green) in 20–50% Au+Au collisions from 7.7 to 27 GeV. (Lower) The ratio of $\Delta\gamma^{112}_{\mathrm{ESS}}$ to inclusive $\langle\Delta\gamma^{112}\rangle$.

the scenario that at least one CME condition breaks down at the lower energies approaching 7.7 GeV, possibly due to the transient QGP matter or incomplete chiral symmetry restoration. The non-zero remaining charge separation between 10 and 20 GeV underscores the need for theoretical insights and could be connected to the CME pictures. Studies near the critical point suggest enhanced topological fluctuations in this energy region [137]. A recent STAR paper found that the magnetic imprint on the QGP matter is more prominent at lower energies than at higher energies [44].

Assuming comparable physics conditions for energies between 10 and 20 GeV, the average value of $N_{\mathrm{part}}\Delta\gamma_{\mathrm{ESS}}^{112}$ is $[4.22 \pm 0.72(stat.)] \times 10^{-3}$, corresponding to a $5.9\sigma$ significance for the observed charge separation signal. The statistical likelihood of observing such positively finite values by chance at four adjacent energies under a pure background fluctuation scenario is less than $7 \times 10^{-12}$, indicating a signal significance of $6.7\sigma$.

### 5.4.1   Beam Energy Scan Dependence of the $H$ correlator and $\kappa_{BG}^{112}$

The elliptic flow background in the CME observable $\Delta\gamma^{112}$ can be explored with a background coefficient, $\kappa_{BG}^{112}$, which couples to the $v_2$ and two-particle correlator $\Delta\delta$. Previously, without an effective probe into the true CME signal part in $\Delta\gamma^{112}$, the $\kappa^{112} = \frac{\Delta\gamma^{112}}{v_2\Delta\delta}$ is studied as a normalized observable for comparison between data and pure-background model[132]. Calculation with the AMPT model found this background coupling coefficient $\kappa^{112}$ to be around 2 to 3 in $\Delta\gamma^{112}$ for $\pi^{\pm}$ and $K^{\pm}$.

In our analysis, based on the Event Shape Selection, we are able to obtain the charge separation $\Delta\gamma_{\mathrm{ESS}}^{112}$ after all-known background suppressed. Thus, the flow background can be described by a normalized coefficient $\kappa_{BG}^{112}$ defined by:

$$\kappa_{BG}^{112} = \frac{\Delta\gamma^{112} - \Delta\gamma_{\mathrm{ESS}}^{112}}{v_2\Delta\delta}, \tag{5.2}$$

Fig. 5.22 presents the normalized observable $\kappa_{BG}^{112}$, subtracted with the Event Shape Se-
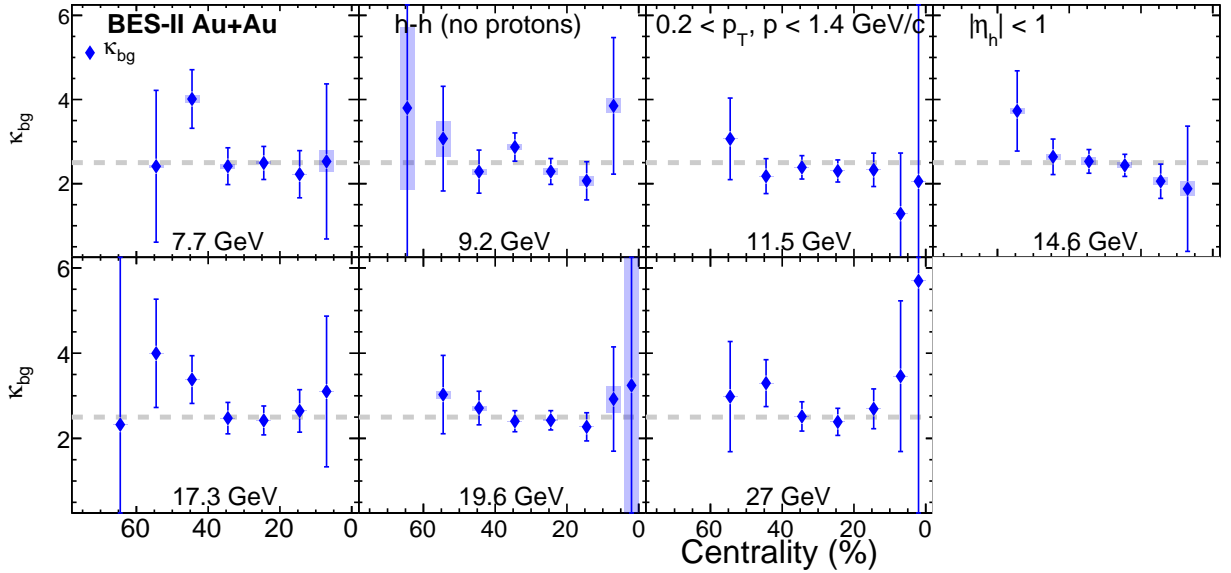
Figure 5.22: Beam energy dependence of the background coefficient $\kappa_{BG}^{112}$, where the horizontal gray line sits at $y = 2.5$ to guide eye.

lection method from $\Delta\gamma^{112}$. In near-central to mid-central collision ranges, a consistent value of $\kappa_{BG}^{112}$ around 2.5 is observed within uncertainty for charged hadrons (excluding protons) in Au+Au collisions from 7.7 to 27 GeV. However, in most peripheral and central regions, the statistical uncertainty is too great to draw definitive conclusions.

The constant $\kappa_{BG}^{112} \sim 2.5$ suggests that the flow background from charge separation mechanisms is largely independent of the beam energy condition such as the magnetic field. In contrast, the residual charge separation after all known background subtraction is observed specifically between 10 and 20 GeV, suggesting that the latter could be linked to the Chiral Magnetic Effect which requires the coexistence of intense magnetic field and chiral restoration, both inherent in a strong beam energy dependence.

Furthermore, the $H$ correlator was previously explored to search for the Chiral Magnetic Effect in Au+Au collisions using the BES-I dataset [60]. We revisit this observable for historical context, as it is designed to directly subtract the flow component from the inclusive CME observable using a predefined coefficient $\kappa$. With measurements of the inclusive $\Delta\gamma^{112}$,
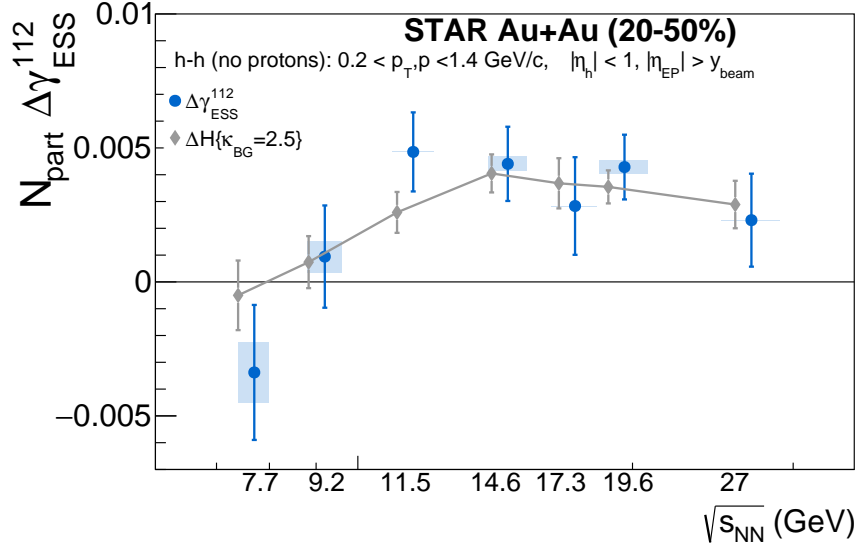
Figure 5.23: Beam energy dependence of $\Delta\gamma^{112}_{\text{ESS}}$ (blue) in contrast to inclusive $\Delta H\{\kappa_{bg} = 2.5\}$ (gray), whose points are linked to guide the eye.

$\Delta\delta$, and $v_2$, we can calculate $\Delta H\{\kappa_{bg} = 2.5\}$, which is defined as follows:

$$\Delta H = \frac{\Delta\gamma^{112} - \kappa_{bg}v_2\Delta\delta}{1 + \kappa_{bg}v_2}, \tag{5.3}$$

where $\kappa_{bg}$ was a predefined coupling coefficient chosen as 2.5.

The results for $N_{\text{part}}\Delta H\{\kappa_{bg} = 2.5\}$ are presented in Fig. 5.23, in comparison with $N_{\text{part}}\Delta\gamma^{112}_{\text{ESS}}$. The points are connected to guide the eye. The observed agreement between $N_{\text{part}}\Delta H$ and $N_{\text{part}}\Delta\gamma^{112}_{\text{ESS}}$ implies that the flow background can be characterized by a coupling constant, $\kappa_{bg} \approx 2.5$, between elliptic flow and the two-particle correlation. The two frameworks, the ESS and the $\Delta H$ correlator, appear to complement each other, but their connection demands further investigation and theoretical insights.

# CHAPTER 6

# Conclusion and Outlook

In heavy-ion collisions, the Chiral Magnetic Effect describes the charge separation of quarks with chirality imbalance under an external strong magnetic field and reflects the fundamental QCD vacuum topology, which comes from the compact nature of the non-Abelien group. The chirality imbalance of light quarks is primarily caused by the QCD vacuum topology transition at high temperatures inside the local domain of the Quark Gluon Plasma created above critical temperatures. Similar vacuum transitions in the Electroweak vacuum are crucial for the baryogenesis in the early universe. Therefore, the search for the CME in high-energy heavy-ion collisions is of great significance to our understanding of the fundamental aspects of those non-Abelian groups in the Standard Model, and to the understanding of the early universe.

The search for the CME over the past two decades faced a primary challenge in the large background contamination in the experimental observable, which prevented a definitive conclusion of the charge separation hitherto. The major background comes from the coupling of collective flow with other short-range charge separation mechanisms, such as decays of flowing resonances, local transverse momentum conservation, and local charge conservation. The nonflow backgrounds raised from jets, di-jets, and other physics uncorrelated to the reaction plane also contribute to the measurement. To control the substantial backgrounds, two experimental approaches have been developed in the mainstream. One is looking at the signal difference between two measurements assuming a similar background, exemplified by the blind analysis in isobar collisions. The difficulty in the isobaric system is the small signal

fraction in such small nuclei collisions and the fast decaying magnetic field at the top RHIC energy. The other approach is to directly control backgrounds, including mitigation of flow background through event shape methods, and suppression of nonflow background using the spectator planes. Previous methods using event shape suffer from a long extrapolation towards zero background due to the lack of control over emission pattern fluctuations. Both approaches have been investigated and discussed in this work, and we focus on the Event Shape approach, by developing a new Event Shape Selection method that targets the flow background.

We investigate the origin of the flow-related backgrounds, illustrated with the decays of flowing resonances. We realize that the elliptic flow observable for resonances is significantly enhanced by the CME signal, which is verified with the AVFD model. Besides, we propose a concept of non-interdependent collective flow to explain that the CME observable is influenced by the elliptic flow mechanism. This concept reflects the factorization between different orders of Fourier harmonics, which manifests universally in both hydrodynamic and transport models. Furthermore, we develop a novel Event Shape Selection method, utilizing particle pair information to construct the event shape from the same-rapidity region, which is sensitive to the background from both emission pattern fluctuations and eccentricity variations. Using models with pure-background, moderate, and strong CME signals, we verify that the optimal ESS solution should use the event shape variable based on particle pairs and the elliptic flow variable based on single particles to project the CME observable to the zero-flow limit. This ESS method can accurately reproduce the true input signal at different background levels and is robust against different background adjustments. Moreover, the CME observable is measurable near the zero-flow limit, significantly improving the projection quality with statistical uncertainties reduced by at least a factor of three.

We have measured the CME sensitive $\Delta\gamma^{112}$ and the background indicator $\Delta\gamma^{132}$ in Au+Au collisions at $\sqrt{s_{NN}} = 7.7 - 27$ GeV from the RHIC Beam Energy Scan II. The magnetic field in Au+Au collisions at lower energies may be stronger and last longer than

128

that in isobar collisions at 200 GeV, potentially enhancing the chance of the CME detection. With the novel Event Shape Selection method, we mitigate the flow background in $\Delta\gamma^{112}$ and $\Delta\gamma^{132}$. Furthermore, the Event Plane Detector at STAR allows the reconstruction of high-resolution spectator planes at all BES-II energies, which are closely correlated with the magnetic field direction, and effectively minimize the nonflow background.

After suppressing the flow background with the Event Shape Selection method, and the nonflow background with the spectator planes, we observe that the background indicator $\Delta\gamma^{132}_{\mathrm{ESS}}$ is consistent with zero at all energies, whereas $\Delta\gamma^{112}_{\mathrm{ESS}}$ reduces to at most 20% of $\langle\Delta\gamma^{112}\rangle$. A remaining charge separation of positive $\Delta\gamma^{112}_{\mathrm{ESS}}$ value with a $3.29\sigma$ ($3.12\sigma$ and $3.47\sigma$) significance is observed in the 20–50% centrality range of Au+Au at $\sqrt{s_{NN}} = 11.5$ (14.6 and 19.6) GeV. The data below 10 GeV are consistent with zero within statistical errors.

The finite $\Delta\gamma^{112}_{\mathrm{ESS}}$ values observed in Au+Au collisions at and above 10 GeV suggest an intriguing scenario where the chirality imbalance of quarks and the intense magnetic field coexist at these energies, resulting in the CME-induced charge separation. Other theory also argues that near critical regions the topological fluctuations may be enhanced so that the charge separation effect is more eminent [137]. Towards 7.7 GeV, our current measurement indicates that partonic degrees of freedom and/or chiral symmetry restoration may diminish in the collision system so that the precondition for the quark chirality effect vanishes.

We have detected a clear charge separation after all known backgrounds mitigated or suppressed in Au+Au collisions at lower energies from the BES-II, which may indicate a finite CME signal. The literal combination of charge separation at 10–20 GeV yields a $5.9\sigma$ significance, though the difference in the magnetic field and the system properties between collision energies needs to be addressed to understand this interpretation. In future heavy-ion experiments, a possible opportunity of lower-energy collisions at 10–20 GeV with higher statistics would be of great scientific interest, with the hope of confirming the observation of the CME.

# APPENDIX A

# QA of BES-II
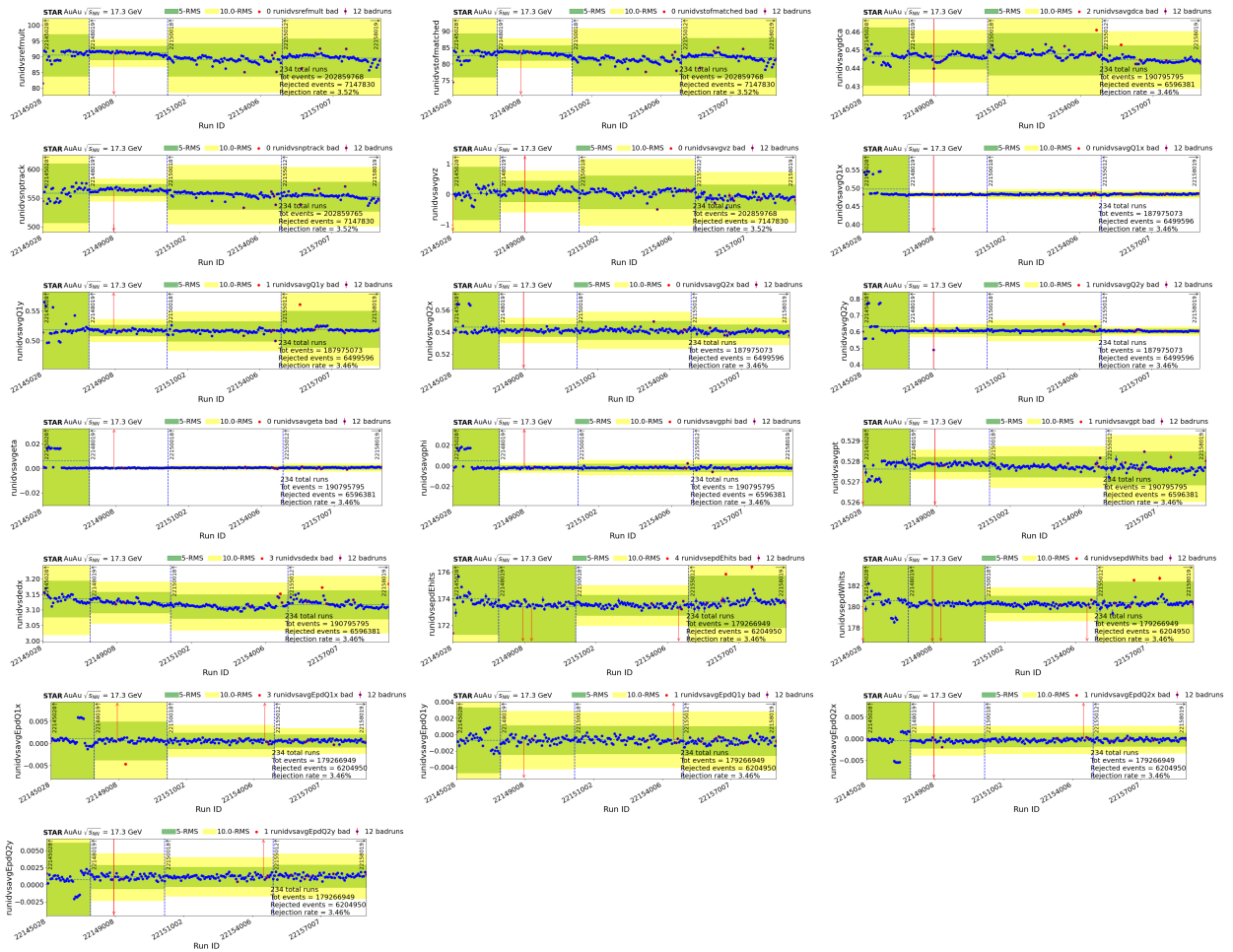
## A.0.1 Quality Assurance in Au+Au at 17.3 GeV



Figure A.1: Quality Assurance plots for Au+Au at 17.3 GeV (run 21).

The detailed plots of bad runs identified by the QA algorithm at 17.3 GeV.

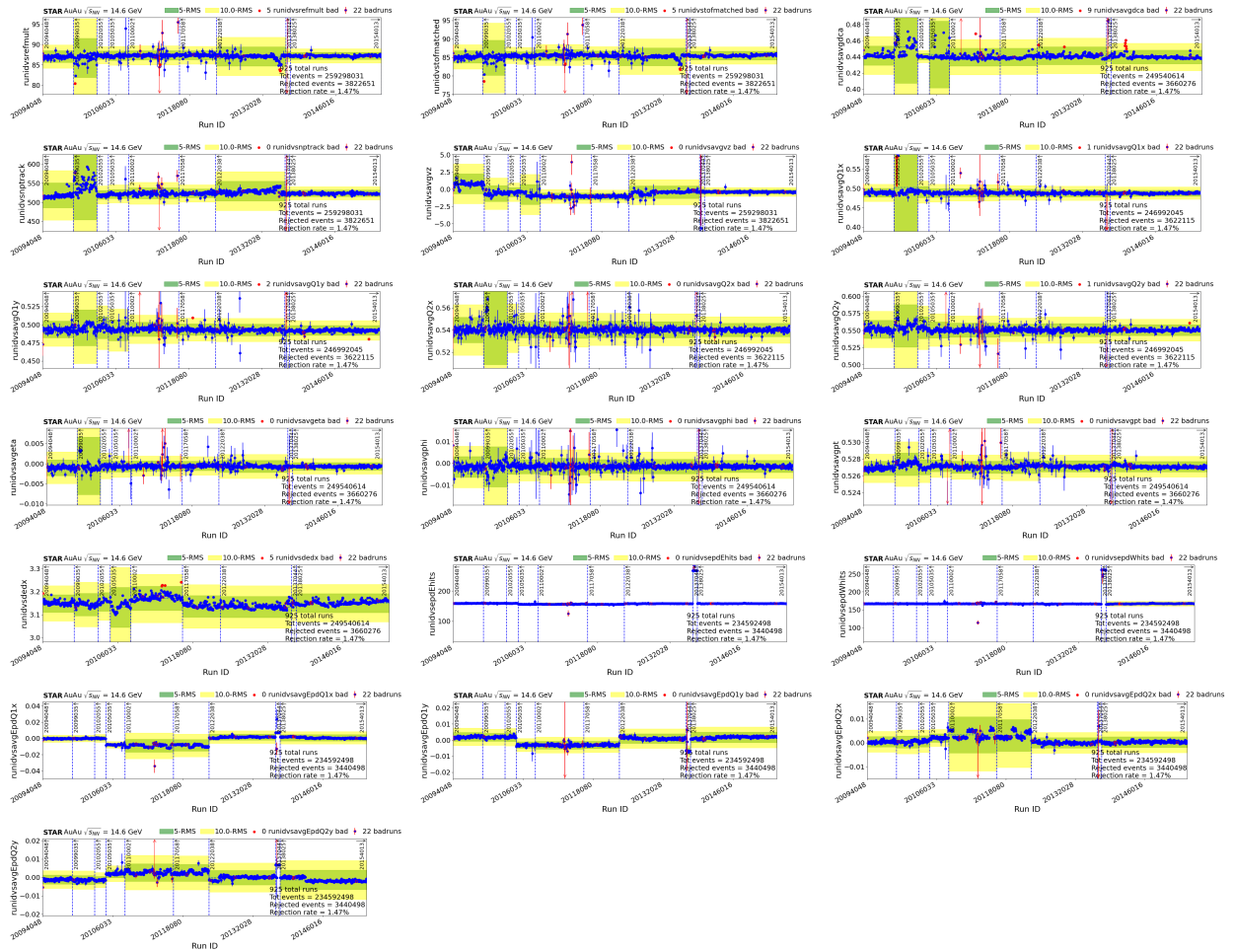## A.0.2 Quality Assurance in Au+Au at 14.6 GeV



Figure A.2: Quality Assurance plots for Au+Au at 14.6 GeV (run 19).

The detailed plots of bad runs identified by the QA algorithm at 14.6 GeV.
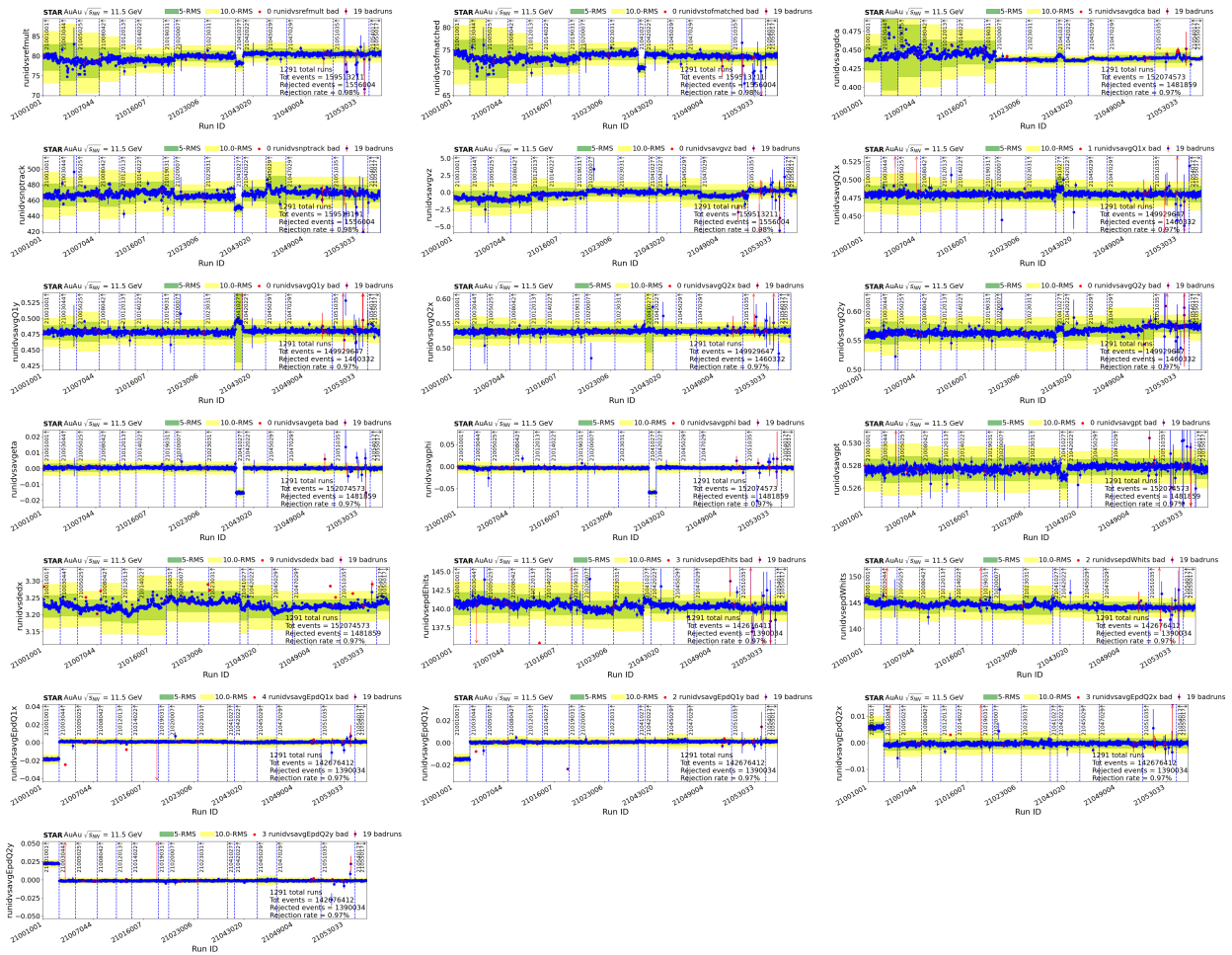
## A.0.3 Quality Assurance in Au+Au at 11.5 GeV



Figure A.3: Quality Assurance plots for Au+Au at 11.5 GeV (run 20) run 20342002 – 20365041

The detailed plots of bad runs identified by the QA algorithm at 11.5 GeV.

Figure A.4: Quality Assurance plots for Au+Au at 11.5 GeV (run 20) run 21001001 – 21055017

133

## A.0.4 Quality Assurance in Au+Au at 9.2 GeV

The detailed plots of bad runs identified by the QA algorithm at 9.2 GeV.
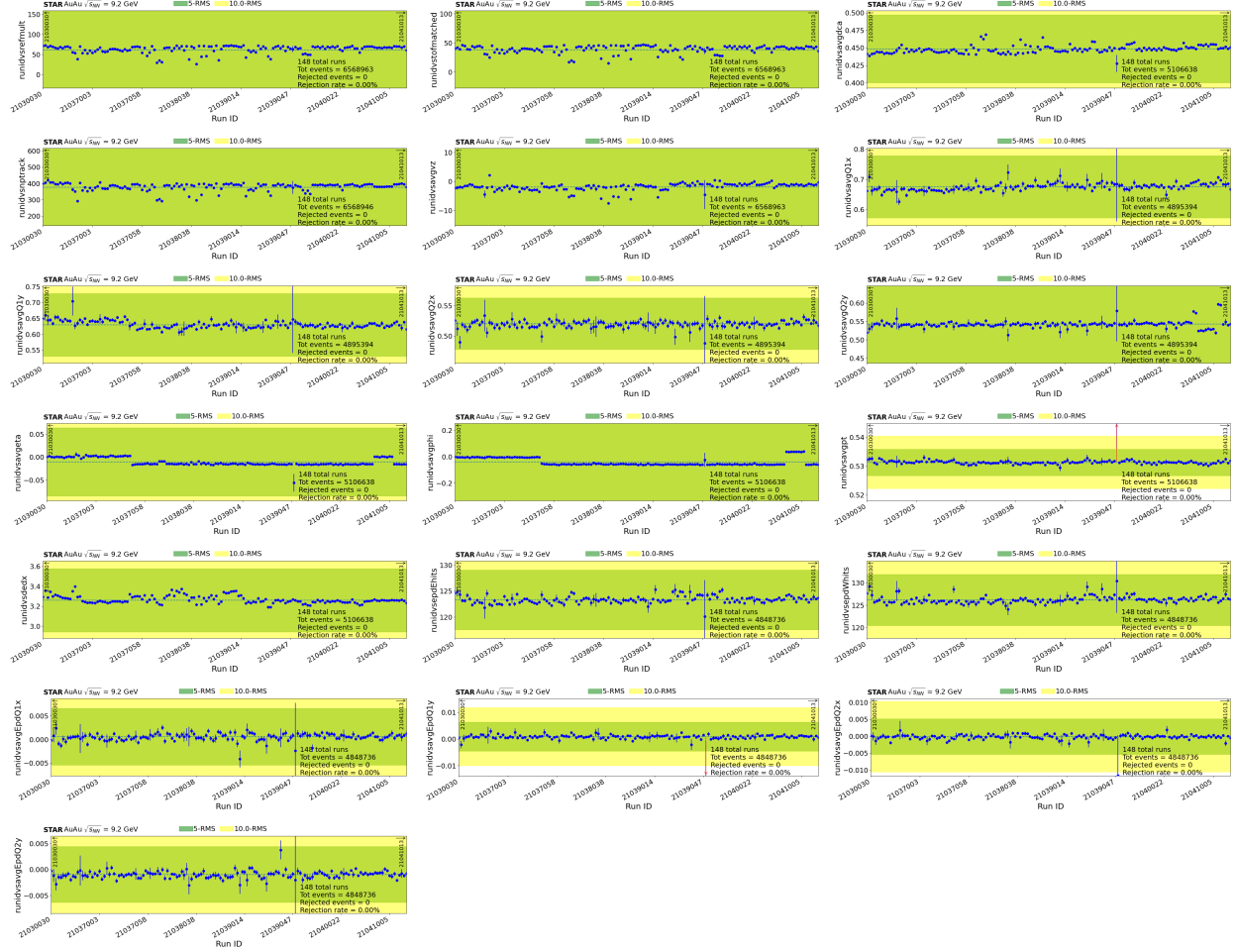


Figure A.5: Quality Assurance plots for Au+Au at 9.2 GeV (run 20) run 21030030 – 21041013.
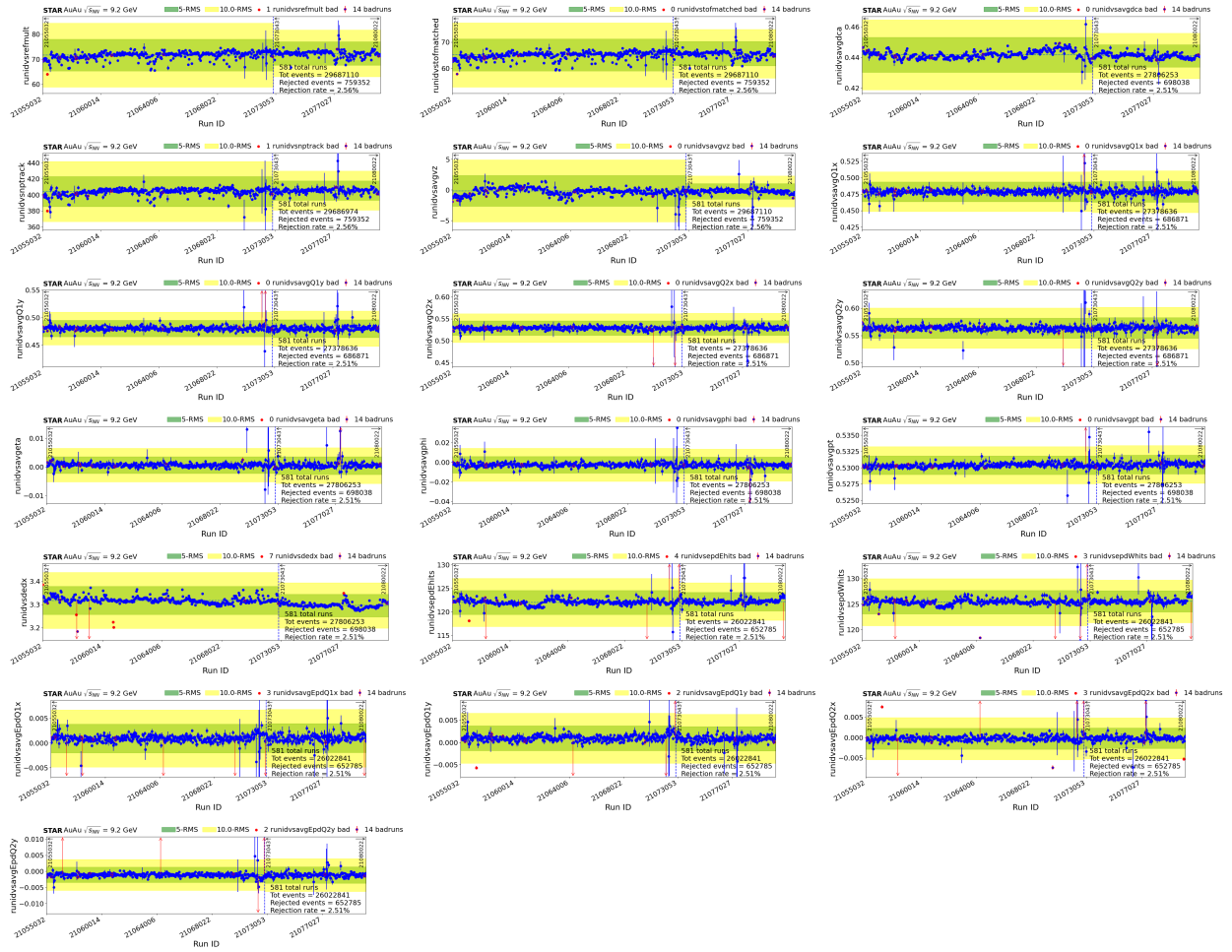
Figure A.6: Quality Assurance plots for Au+Au at 9.2 GeV (run 20) run 21055032 - 21080027.
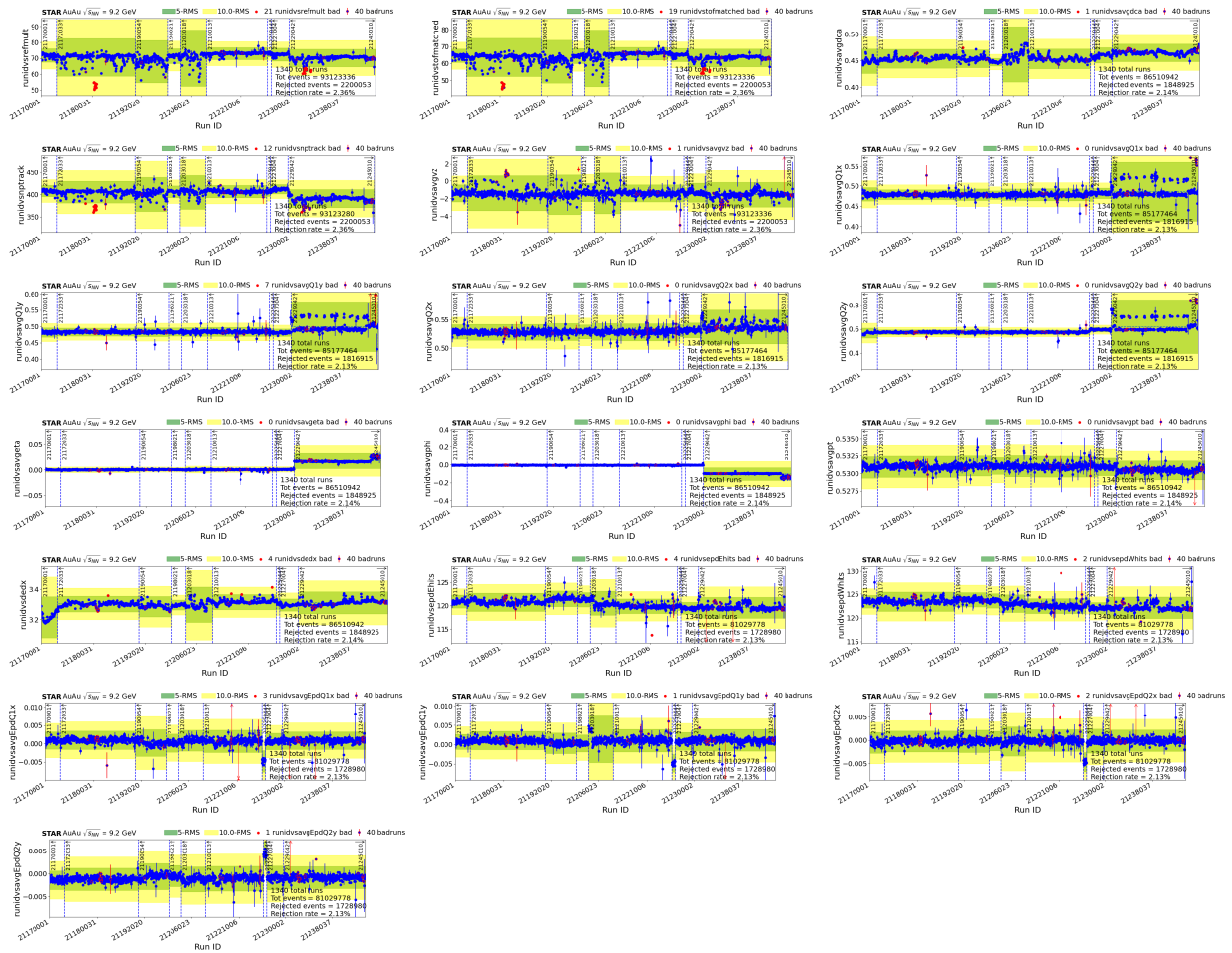
Figure A.7: Quality Assurance plots for Au+Au at 9.2 GeV (run 20) run 21169035 - 21245010.

## A.0.5 Quality Assurance in Au+Au at 7.7 GeV

The detailed plots of bad runs identified by the QA algorithm at 7.7 GeV.
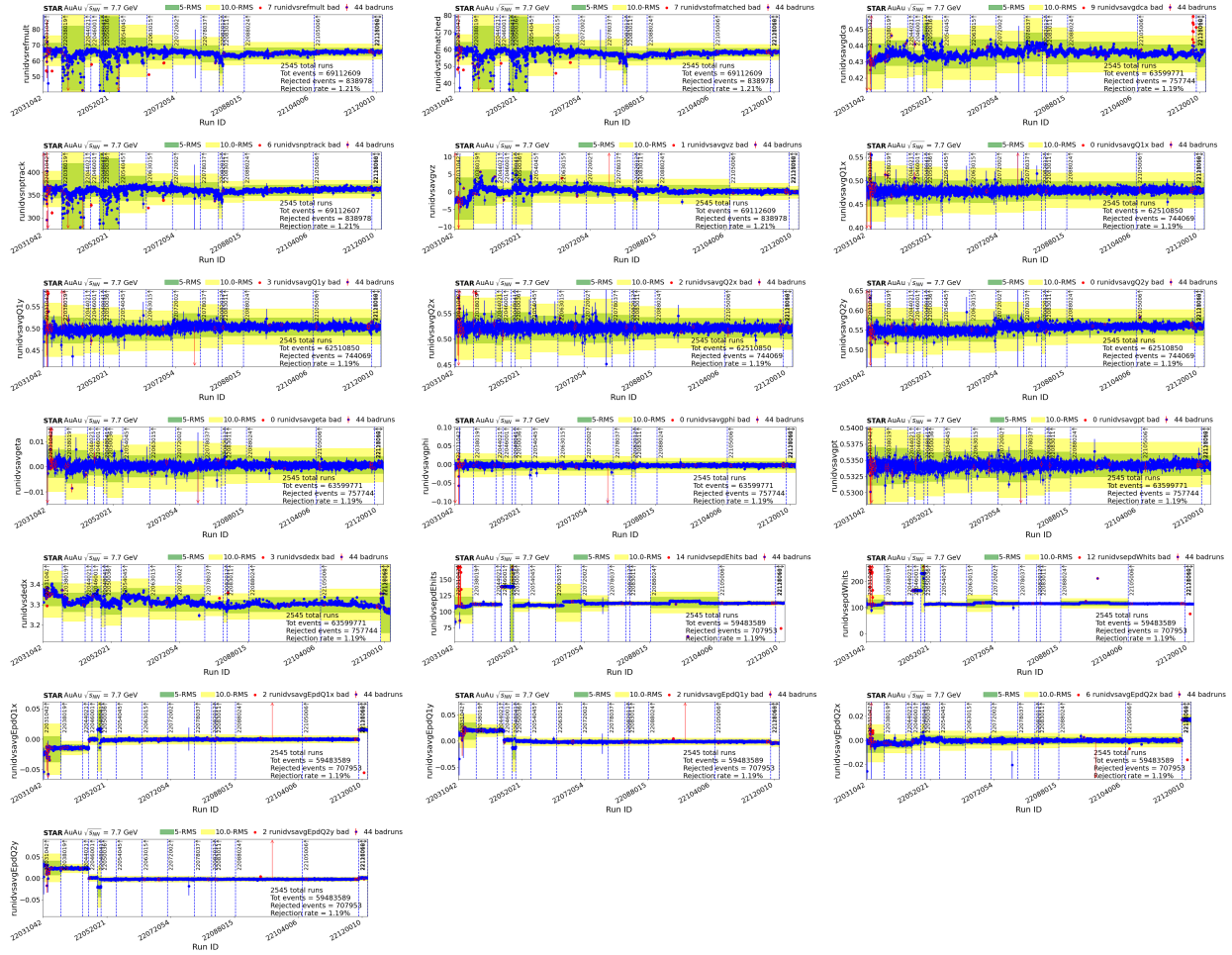


Figure A.8: Quality Assurance plots for Au+Au at 7.7 GeV (run 21).

137

# Bibliography

[1] H. Fritzsch, M. Gell-Mann, and H. Leutwyler, "Advantages of the color octet gluon picture," *Physics Letters B*, vol. 47, no. 4, pp. 365–368, 1973. DOI: https://doi.org/10.1016/0370-2693(73)90625-4.

[2] M. Y. Han and Y. Nambu, "Three-triplet model with double SU(3) symmetry," *Phys. Rev.*, vol. 139, B1006–B1010, 4B Aug. 1965. DOI: 10.1103/PhysRev.139.B1006.

[3] O. W. Greenberg, "Spin and unitary-spin independence in a paraquark model of baryons and mesons," *Phys. Rev. Lett.*, vol. 13, pp. 598–602, 20 Nov. 1964. DOI: 10.1103/PhysRevLett.13.598.

[4] S. L. Glashow, "The renormalizability of vector meson interactions," *Nuclear Physics*, vol. 10, pp. 107–117, 1959. DOI: https://doi.org/10.1016/0029-5582(59)90196-8.

[5] S. L. Glashow, "Partial-symmetries of weak interactions," *Nuclear Physics*, vol. 22, no. 4, pp. 579–588, 1961. DOI: https://doi.org/10.1016/0029-5582(61)90469-2.

[6] A. Salam, "Weak and electromagnetic interactions," *Il Nuovo Cimento (1955-1965)*, vol. 11, pp. 568–577, 1959. DOI: https://doi.org/10.1007/BF02726525.

[7] S. Weinberg, "A model of leptons," *Phys. Rev. Lett.*, vol. 19, pp. 1264–1266, 21 Nov. 1967. DOI: 10.1103/PhysRevLett.19.1264.

[8] M. E. Peskin and D. V. Schroeder, *An Introduction to quantum field theory*. Reading, USA: Addison-Wesley, 1995.

[9] M. Gell-Mann, "Symmetries of baryons and mesons," *Phys. Rev.*, vol. 125, pp. 1067–1084, 3 Feb. 1962. DOI: 10.1103/PhysRev.125.1067.

[10] M. Gell-Mann, "A schematic model of baryons and mesons," *Physics Letters*, vol. 8, no. 3, pp. 214–215, 1964. DOI: https://doi.org/10.1016/S0031-9163(64)92001-3.

[11] G. Zweig, "An su(3) model for strong interaction symmetry and its breaking," *CERN Document Server.*, 1964.

[12] D. J. Gross and F. Wilczek, "Ultraviolet behavior of non-abelian gauge theories," *Phys. Rev. Lett.*, vol. 30, pp. 1343–1346, 26 Jun. 1973. DOI: 10.1103/PhysRevLett.30.1343.

[13] H. D. Politzer, "Reliable perturbative results for strong interactions?" *Phys. Rev. Lett.*, vol. 30, pp. 1346–1349, 26 Jun. 1973. DOI: 10.1103/PhysRevLett.30.1346.

[14] E. V. Shuryak, "Quantum chromodynamics and the theory of superdense matter," *Physics Reports*, vol. 61, no. 2, pp. 71–158, 1980. DOI: https://doi.org/10.1016/0370-1573(80)90105-2.

[15] A. Aprahamian, S. Lapi, P. Mantica, *et al.*, "Reaching for the horizon: The 2015 long range plan for nuclear science," *Reaching for the Horizon: The*, 2015.

[16] A. Bazavov, H.-T. Ding, P. Hegde, *et al.*, "Chiral crossover in qcd at zero and non-zero chemical potentials," *Physics Letters B*, vol. 795, pp. 15–21, 2019. DOI: https://doi.org/10.1016/j.physletb.2019.05.013.

[17] J. W. Harris and B. Müller, *"qgp signatures" revisited*, 2024. arXiv: 2308.05743 (hep-ph).

[18] J. R. Morones-Ibarra, A. Enriquez-Perez-Gavilan, A. I. H. Rodriguez, F. V. Flores-Baez, N. B. Mata-Carrizalez, and E. V. Ordoñez, *Open Physics*, vol. 15, no. 1, pp. 1039–1044, 2017. DOI: doi:10.1515/phys-2017-0130.

[19] D. A. e. a. T. Nishi K. Itahashi, "Chiral symmetry restoration at high matter density observed in pionic atoms," *Nat. Phys.*, vol. 19, pp. 788–793, 2023. DOI: https://doi.org/10.1038/s41567-023-02001-x.

[20] H. Song, S. A. Bass, U. Heinz, T. Hirano, and C. Shen, "200 $A$ gev Au + Au collisions serve a nearly perfect quark-gluon liquid," *Phys. Rev. Lett.*, vol. 106, p. 192 301, 19 May 2011. DOI: 10.1103/PhysRevLett.106.192301.

[21] M. Bernhard and Bass, "Bayesian estimation of the specific shear and bulk viscosity of quark–gluon plasma," *Nat. Phys.*, vol. 15, pp. 1113–1117, 2019. DOI: https://doi.org/10.1038/s41567-019-0611-8.

[22] STAR Collaboration, *Phys. Rev. Lett.*, vol. 92, p. 052 302, 5 Feb. 2004. DOI: 10.1103/PhysRevLett.92.052302.

[23] L. Rezzolla and O. Zanotti, *Relativistic Hydrodynamics*. 2013.

[24] A. Belavin, A. Polyakov, A. Schwartz, and Y. Tyupkin, "Pseudoparticle solutions of the yang-mills equations," *Physics Letters B*, vol. 59, no. 1, pp. 85–87, 1975. DOI: https://doi.org/10.1016/0370-2693(75)90163-X.

[25] C. Abel, S. Afach, N. J. Ayres, *et al.*, "Measurement of the permanent electric dipole moment of the neutron," *Phys. Rev. Lett.*, vol. 124, p. 081 803, 8 Feb. 2020. DOI: 10.1103/PhysRevLett.124.081803.

[26] D. E. Kharzeev, "Topologically induced local pandcp violation in qcd×qed," *Annals of Physics*, vol. 325, no. 1, pp. 205–218, 2010, January 2010 Special Issue. DOI: https://doi.org/10.1016/j.aop.2009.11.002.

[27] D. Kharzeev, "Parity violation in hot qcd: Why it can happen, and how to look for it," *Physics Letters B*, vol. 633, no. 2, pp. 260–264, 2006. DOI: https://doi.org/10.1016/j.physletb.2005.11.075.

[28] G. 't Hooft, "Symmetry breaking through bell-jackiw anomalies," *Phys. Rev. Lett.*, vol. 37, pp. 8–11, 1 Jul. 1976. DOI: 10.1103/PhysRevLett.37.8.

[29] G. 't Hooft, "Computation of the quantum effects due to a four-dimensional pseudoparticle," *Phys. Rev. D*, vol. 14, pp. 3432–3450, 12 Dec. 1976. DOI: 10.1103/PhysRevD.14.3432.

[30] W. Bernreuther, *Cp violation and baryogenesis*, 2002. arXiv: hep-ph/0205279 (hep-ph).

[31] V. Kuzmin, V. Rubakov, and M. Shaposhnikov, "On anomalous electroweak baryon-number non-conservation in the early universe," *Physics Letters B*, vol. 155, no. 1, pp. 36–42, 1985. DOI: https://doi.org/10.1016/0370-2693(85)91028-7.

[32] K. Fukushima, D. E. Kharzeev, and H. J. Warringa, "Chiral magnetic effect," *Phys. Rev. D*, vol. 78, p. 074 033, 7 Oct. 2008. DOI: 10.1103/PhysRevD.78.074033.

[33] D. Kharzeev, A. Krasnitz, and R. Venugopalan, "Anomalous chirality fluctuations in the initial stage of heavy ion collisions and parity odd bubbles," *Physics Letters B*, vol. 545, no. 3, pp. 298–306, 2002. DOI: https://doi.org/10.1016/S0370-2693(02)02630-8.

[34] P. Romatschke and R. Venugopalan, "Collective non-abelian instabilities in a melting color glass condensate," *Phys. Rev. Lett.*, vol. 96, p. 062 302, 6 Feb. 2006. DOI: 10.1103/PhysRevLett.96.062302.

[35] D. E. Kharzeev, L. D. McLerran, and H. J. Warringa, "The effects of topological charge change in heavy ion collisions: "event by event p and cp violation"," *Nuclear Physics A*, vol. 803, no. 3, pp. 227–253, 2008. DOI: https://doi.org/10.1016/j.nuclphysa.2008.02.298.

[36] D. E. Kharzeev and J. Liao, "Chiral magnetic effect reveals the topology of gauge fields in heavy-ion collisions," *Nature Reviews Physics*, vol. 3, no. 1, pp. 55–63, Jan. 2021. DOI: 10.1038/s42254-020-00254-6.

[37] Q. Li, D. E. Kharzeev, C. Zhang, *et al.*, "Chiral magnetic effect in zrte5," *Nature Physics*, vol. 12, no. 6, pp. 550–554, Jun. 2016. DOI: 10.1038/nphys3648.

[38] J. Xiong, S. K. Kushwaha, T. Liang, *et al.*, "Evidence for the chiral anomaly in the dirac semimetal na¡sub¿3¡/sub¿bi," *Science*, vol. 350, no. 6259, pp. 413–416, 2015. DOI: 10.1126/science.aac6089.

[39] X. Huang, L. Zhao, Y. Long, *et al.*, "Observation of the chiral-anomaly-induced negative magnetoresistance in 3d weyl semimetal taas," *Phys. Rev. X*, vol. 5, p. 031 023, 3 Aug. 2015. DOI: 10.1103/PhysRevX.5.031023.

[40] D. E. Kharzeev and D. T. Son, "Testing the chiral magnetic and chiral vortical effects in heavy ion collisions," *Phys. Rev. Lett.*, vol. 106, p. 062 301, 6 Feb. 2011. DOI: 10.1103/PhysRevLett.106.062301.

[41] D. E. Kharzeev and H.-U. Yee, "Chiral magnetic wave," *Phys. Rev. D*, vol. 83, p. 085 007, 8 Apr. 2011. DOI: 10.1103/PhysRevD.83.085007.

[42] A. Huang, D. She, S. Shi, M. Huang, and J. Liao, "Dynamical magnetic fields in heavy-ion collisions," *Phys. Rev. C*, vol. 107, p. 034 901, 3 Mar. 2023. DOI: 10.1103/PhysRevC.107.034901.

[43] H.-T. Ding, A. Francis, O. Kaczmarek, F. Karsch, E. Laermann, and W. Soeldner, "Thermal dilepton rate and electrical conductivity: An analysis of vector current correlation functions in quenched lattice qcd," *Phys. Rev. D*, vol. 83, p. 034 504, 3 Feb. 2011. DOI: 10.1103/PhysRevD.83.034504.

[44] STAR Collaboration, "Observation of the electromagnetic field effect via charge-dependent directed flow in heavy-ion collisions at the relativistic heavy ion collider," *Phys. Rev. X*, vol. 14, p. 011 028, 1 Feb. 2024. DOI: 10.1103/PhysRevX.14.011028.

[45] A. M. Poskanzer and S. A. Voloshin, "Methods for analyzing anisotropic flow in relativistic nuclear collisions," *Phys. Rev. C*, vol. 58, pp. 1671–1678, 3 Sep. 1998. DOI: 10.1103/PhysRevC.58.1671.

[46] S. A. Voloshin, "Parity violation in hot qcd: How to detect it," *Phys. Rev. C*, vol. 70, p. 057 901, 5 Nov. 2004. DOI: 10.1103/PhysRevC.70.057901.

[47] U. Heinz and R. Snellings, "Collective flow and viscosity in relativistic heavy-ion collisions," *Annual Review of Nuclear and Particle Science*, vol. 63, no. Volume 63,

2013, pp. 123–151, 2013. DOI: https://doi.org/10.1146/annurev-nucl-102212-170540.

[48]   S. Choudhury *et al.*, "Investigation of experimental observables in search of the chiral magnetic effect in heavy-ion collisions in the STAR experiment *," *Chin. Phys. C*, vol. 46, no. 1, p. 014 101, 2022. DOI: 10.1088/1674-1137/ac2a1f.

[49]   N. Magdy, S. Shi, J. Liao, N. Ajitanand, and R. A. Lacey, "New correlator to detect and characterize the chiral magnetic effect," *Phys. Rev. C*, vol. 97, p. 061 901, 6 Jun. 2018. DOI: 10.1103/PhysRevC.97.061901.

[50]   A. H. Tang, "Probe chiral magnetic effect with signed balance function," *Chin. Phys. C*, vol. 44, no. 5, p. 054 101, 2020. DOI: 10.1088/1674-1137/44/5/054101.

[51]   STAR Collaboration, "Azimuthal charged-particle correlations and possible local strong parity violation," *Phys. Rev. Lett.*, vol. 103, p. 251 601, 25 Dec. 2009. DOI: 10.1103/PhysRevLett.103.251601.

[52]   STAR Collaboration, "Observation of charge-dependent azimuthal correlations and possible local strong parity violation in heavy-ion collisions," *Phys. Rev. C*, vol. 81, p. 054 908, 5 May 2010. DOI: 10.1103/PhysRevC.81.054908.

[53]   STAR Collaboration, "Fluctuations of charge separation perpendicular to the event plane and local parity violation in $\sqrt{s_{\text{NN}}} = 200$ gev au + au collisions at the bnl relativistic heavy ion collider," *Phys. Rev. C*, vol. 88, p. 064 911, 6 Dec. 2013. DOI: 10.1103/PhysRevC.88.064911.

[54]   ALICE Collaboration, "Charge separation relative to the reaction plane in pb-pb collisions at $\sqrt{s_{NN}}$=2.76 TeV," *Phys. Rev. Lett.*, vol. 110, p. 012 301, 1 Jan. 2013. DOI: 10.1103/PhysRevLett.110.012301.

[55]   S. Schlichting and S. Pratt, "Charge conservation at energies available at the bnl relativistic heavy ion collider and contributions to local parity violation observables," *Phys. Rev. C*, vol. 83, p. 014 913, 1 Jan. 2011. DOI: 10.1103/PhysRevC.83.014913.

[56] W.-Y. Wu, Q.-Y. Shou, P. Christakoglou, *et al.*, "Global constraint on the magnitude of anomalous chiral effects in heavy-ion collisions," *Phys. Rev. C*, vol. 107, p. L031902, 3 Mar. 2023. DOI: 10.1103/PhysRevC.107.L031902.

[57] S. Pratt, S. Schlichting, and S. Gavin, "Effects of momentum conservation and flow on angular correlations observed in experiments at the bnl relativistic heavy ion collider," *Phys. Rev. C*, vol. 84, p. 024 909, 2 Aug. 2011. DOI: 10.1103/PhysRevC.84.024909.

[58] CMS Collaboration, "Observation of charge-dependent azimuthal correlations in $p-$Pb collisions and its implication for the search for the chiral magnetic effect," *Phys. Rev. Lett.*, vol. 118, p. 122 301, 12 Mar. 2017. DOI: 10.1103/PhysRevLett.118.122301.

[59] CMS Collaboration, "Constraints on the chiral magnetic effect using charge-dependent azimuthal correlations in $p$Pb and pbpb collisions at the cern large hadron collider," *Phys. Rev. C*, vol. 97, p. 044 912, 4 Apr. 2018. DOI: 10.1103/PhysRevC.97.044912.

[60] STAR Collaboration, "Beam-energy dependence of charge separation along the magnetic field in Au + Au collisions at rhic," *Phys. Rev. Lett.*, vol. 113, p. 052 302, 5 Jul. 2014. DOI: 10.1103/PhysRevLett.113.052302.

[61] STAR Collaboration, "Charge-dependent pair correlations relative to a third particle in p+au and d+au collisions at rhic," *Physics Letters B*, vol. 798, p. 134 975, 2019. DOI: https://doi.org/10.1016/j.physletb.2019.134975.

[62] W.-T. Deng, X.-G. Huang, G.-L. Ma, and G. Wang, "Testing the chiral magnetic effect with isobaric collisions," *Phys. Rev. C*, vol. 94, p. 041 901, 4 Oct. 2016. DOI: 10.1103/PhysRevC.94.041901.

[63] V. Koch, S. Schlichting, V. Skokov, *et al.*, "Status of the chiral magnetic effect and collisions of isobars," *Chinese Physics C*, vol. 41, no. 7, p. 072 001, Jul. 2017. DOI: 10.1088/1674-1137/41/7/072001.

[64] W.-T. Deng, X.-G. Huang, G.-L. Ma, and G. Wang, "Predictions for isobaric collisions at $\sqrt{s_{NN}} = 200$ gev from a multiphase transport model," *Phys. Rev. C*, vol. 97, p. 044 901, 4 Apr. 2018. DOI: 10.1103/PhysRevC.97.044901.

[65] "STAR Collaboration," *Phys. Rev. C*, vol. 105, p. 014 901, 1 Jan. 2022. DOI: 10.1103/PhysRevC.105.014901.

[66] S. Collaboration, *Estimate of background baseline and upper limit on the chiral magnetic effect in isobar collisions at $\sqrt{s_{NN}} = 200$ gev at the relativistic heavy-ion collider*, 2023. arXiv: 2310.13096 (nucl-ex).

[67] S. A. Voloshin, "Estimate of the signal from the chiral magnetic effect in heavy-ion collisions from measurements relative to the participant and spectator flow planes," *Phys. Rev. C*, vol. 98, p. 054 911, 5 Nov. 2018. DOI: 10.1103/PhysRevC.98.054911.

[68] H.-J. Xu, J. Zhao, X.-B. Wang, *et al.*, "Varying the chiral magnetic effect relative to flow in a single nucleus-nucleus collision*," *Chinese Physics C*, vol. 42, no. 8, p. 084 103, Jul. 2018. DOI: 10.1088/1674-1137/42/8/084103.

[69] STAR Collaboration, "Search for the chiral magnetic effect via charge-dependent azimuthal correlations relative to spectator and participant planes in Au + Au collisions at $\sqrt{s_{NN}} = 200$ GeV," *Phys. Rev. Lett.*, vol. 128, p. 092 301, 9 Mar. 2022. DOI: 10.1103/PhysRevLett.128.092301.

[70] STAR Collaboration, "Search for the chiral magnetic effect in au+au collisions at snn=27 gev with the star forward event plane detectors," *Physics Letters B*, vol. 839, p. 137 779, 2023. DOI: https://doi.org/10.1016/j.physletb.2023.137779.

[71] J. Zhao, H. Li, and F. Wang, "Isolating the chiral magnetic effect from backgrounds by pair invariant mass," *The European Physical Journal C*, vol. 79, no. 2, p. 168, Feb. 2019. DOI: 10.1140/epjc/s10052-019-6671-1.

[72] STAR Collaboration, "Pair invariant mass to isolate background in the search for the chiral magnetic effect in Au + Au collisions at $\sqrt{s_{\mathrm{NN}}} = 200\text{GeV}$," *Phys. Rev. C*, vol. 106, p. 034 908, 3 Sep. 2022. DOI: 10.1103/PhysRevC.106.034908.

[73] J. Schukraft, A. Timmins, and S. A. Voloshin, "Ultra-relativistic nuclear collisions: event shape engineering," *Phys. Lett. B*, vol. 719, pp. 394–398, 2013. DOI: 10.1016/j.physletb.2013.01.045.

[74] STAR Collaboration, "Measurement of charge multiplicity asymmetry correlations in high-energy nucleus-nucleus collisions at $\sqrt{s_{NN}} = 200$ gev," *Phys. Rev. C*, vol. 89, p. 044 908, 4 Apr. 2014. DOI: 10.1103/PhysRevC.89.044908.

[75] ALICE Collaboration, "Constraining the magnitude of the chiral magnetic effect with event shape engineering in pb–pb collisions at snn=2.76 tev," *Physics Letters B*, vol. 777, pp. 151–162, 2018. DOI: https://doi.org/10.1016/j.physletb.2017.12.021.

[76] ALICE Collaboration, "Constraining the chiral magnetic effect with charge-dependent azimuthal correlations in pb-pb collisions at $$ \sqrt{s_{\mathrm{nn}}}$$ $= 2.76 and 5.02 tev$," *Journal of High Energy Physics*, vol. 2020, no. 9, p. 160, Sep. 2020. DOI: 10.1007/JHEP09(2020)160.

[77] Z. Xu, B. Chan, G. Wang, A. Tang, and H. Z. Huang, "Event shape selection method in search of the chiral magnetic effect in heavy-ion collisions," *Physics Letters B*, vol. 848, p. 138 367, 2024. DOI: https://doi.org/10.1016/j.physletb.2023.138367.

[78] Brookhaven National Laboratory, "Relativistic heavy ion collider: Configuration manual," 2006.

[79] X.-N. WANG, "Heavy ion theory: Qcd and matter in extremis," in *High Energy Physics*, pp. 64–70. DOI: 10.1142/9789812790873_0007.

[80] A. Pikin, J. G. Alessi, E. N. Beebe, *et al.*, "Rhic ebis: Basics of design and status of commissioning1," *Journal of Instrumentation*, vol. 5, no. 09, p. C09003, Sep. 2010. DOI: 10.1088/1748-0221/5/09/C09003.

[81] D. Steski, J. Alessi, J. Benjamin, *et al.*, "Upgrade and operation of the bnl tandems for rhic injection," in *PACS2001. Proceedings of the 2001 Particle Accelerator Conference (Cat. No.01CH37268)*, vol. 4, 2001, 2545–2547 vol.4. DOI: 10.1109/PAC.2001.987825.

[82] K. Zeno, "The 2020 low energy gold run in the injectors," Dec. 2020. DOI: 10.2172/1756301.

[83] W. Weng, "Operation of the brookhaven ags with the booster," in *Proceedings of International Conference on Particle Accelerators*, 1993, 3726–3730 vol.5. DOI: 10.1109/PAC.1993.309770.

[84] J. B. Adams, "The alternating gradient proton synchrotron," *Il Nuovo Cimento Series 10*, vol. 2, no. 1, pp. 355–374, Jan. 1955. DOI: 10.1007/BF02746095.

[85] W. W. e. a. MacKay, "Ags to rhic transfer line: Design and commissioning," *Conf. Proc. C*, vol. 960610, pp. 2376–2378, 1996.

[86] DOE, "Reaching for the Horizon: The 2015 Long Range Plan for Nuclear Science," Sep. 2015.

[87] Brookhaven National Laboratory, "Run overview of the rhic,"

[88] C. Adler, A. Denisov, E. Garcia, M. Murray, H. Stroebele, and S. White, "The rhic zero degree calorimeters," *Nuclear Instruments and Methods in Physics Research Section A: Accelerators, Spectrometers, Detectors and Associated Equipment*, vol. 470, no. 3, pp. 488–499, 2001. DOI: https://doi.org/10.1016/S0168-9002(01)00627-1.

[89] W. Llope, J. Zhou, T. Nussbaum, *et al.*, "The star vertex position detector," *Nuclear Instruments and Methods in Physics Research Section A: Accelerators, Spectrometers, Detectors and Associated Equipment*, vol. 759, pp. 23–28, 2014. DOI: https://doi.org/10.1016/j.nima.2014.04.080.

[90] M. Anderson, J. Berkovitz, W. Betts, *et al.*, "The star time projection chamber: A unique tool for studying high multiplicity events at rhic," *Nuclear Instruments and Methods in Physics Research Section A: Accelerators, Spectrometers, Detectors and Associated Equipment*, vol. 499, no. 2, pp. 659–678, 2003, The Relativistic Heavy Ion Collider Project: RHIC and its Detectors. DOI: https://doi.org/10.1016/S0168-9002(02)01964-2.

[91] W. Llope, "The large-area time-of-flight upgrade for star," *Nuclear Instruments and Methods in Physics Research Section B: Beam Interactions with Materials and Atoms*, vol. 241, no. 1, pp. 306–310, 2005. DOI: https://doi.org/10.1016/j.nimb.2005.07.089.

[92] J. Adams, A. Ewigleben, S. Garrett, *et al.*, "The star event plane detector," *Nuclear Instruments and Methods in Physics Research Section A: Accelerators, Spectrometers, Detectors and Associated Equipment*, vol. 968, p. 163 970, 2020. DOI: https://doi.org/10.1016/j.nima.2020.163970.

[93] E. Judd, L. Bland, H. Crawford, *et al.*, "The evolution of the star trigger system," *Nuclear Instruments and Methods in Physics Research Section A: Accelerators, Spectrometers, Detectors and Associated Equipment*, vol. 902, pp. 228–237, 2018. DOI: https://doi.org/10.1016/j.nima.2018.03.070.

[94] D. Smirnov, J. Lauret, V. Perevoztchikov, G. V. Buren, and J. Webb, "Vertex reconstruction at star: Overview and performance evaluation," *Journal of Physics: Conference Series*, vol. 898, no. 4, p. 042 058, Oct. 2017. DOI: 10.1088/1742-6596/898/4/042058.

[95]  R. Reed, J. Balewski, L. S. Barnby, A. Ogawa, J. Lauret, and M. van Leeuwen, "Vertex finding in pile-up rich events for p+p and d+au collisions at star," *Journal of Physics: Conference Series*, vol. 219, no. 3, p. 032 020, Apr. 2010. DOI: 10.1088/1742-6596/219/3/032020.

[96]  T. Sjöstrand, S. Mrenna, and P. Skands, "Pythia 6.4 physics and manual," *Journal of High Energy Physics*, vol. 2006, no. 05, p. 026, May 2006. DOI: 10.1088/1126-6708/2006/05/026.

[97]  STAR Collaboration, "Systematic measurements of identified particle spectra in $pp$, $d+$Au, and Au$+$Au collisions at the star detector," *Phys. Rev. C*, vol. 79, p. 034 909, 3 Mar. 2009. DOI: 10.1103/PhysRevC.79.034909.

[98]  STAR Collaboration, "$\rho^0$ Production and possible modification in Au$+$Au and $p+p$ collisions at $\sqrt{s_{NN}} = 200$ GeV," *Phys. Rev. Lett.*, vol. 92, p. 092 301, 9 Mar. 2004. DOI: 10.1103/PhysRevLett.92.092301.

[99]  S. Shi, Y. Jiang, E. Lilleskov, and J. Liao, "Anomalous chiral transport in heavy ion collisions from anomalous-viscous fluid dynamics," *Annals of Physics*, vol. 394, pp. 50–72, 2018. DOI: https://doi.org/10.1016/j.aop.2018.04.026.

[100]  Y. Jiang, S. Shi, Y. Yin, and J. Liao, "Quantifying the chiral magnetic effect from anomalous-viscous fluid dynamics*," *Chinese Physics C*, vol. 42, no. 1, p. 011 001, Jan. 2018. DOI: 10.1088/1674-1137/42/1/011001.

[101]  S. Shi, H. Zhang, D. Hou, and J. Liao, "Signatures of chiral magnetic effect in the collisions of isobars," *Phys. Rev. Lett.*, vol. 125, p. 242 301, 24 Dec. 2020. DOI: 10.1103/PhysRevLett.125.242301.

[102]  C. Shen, Z. Qiu, H. Song, J. Bernhard, S. Bass, and U. Heinz, "The iebe-vishnu code package for relativistic heavy-ion collisions," *Computer Physics Communications*, vol. 199, pp. 61–85, 2016. DOI: https://doi.org/10.1016/j.cpc.2015.08.039.

149

[103] M. Bleicher, E. Zabrodin, C. Spieles, *et al.*, "Relativistic hadron-hadron collisions in the ultra-relativistic quantum molecular dynamics model," *Journal of Physics G: Nuclear and Particle Physics*, vol. 25, no. 9, p. 1859, Sep. 1999. DOI: `10.1088/0954-3899/25/9/308`.

[104] H. Petersen and B. Müller, "Possibility of event shape selection in relativistic heavy ion collisions," *Phys. Rev. C*, vol. 88, p. 044 918, 4 Oct. 2013. DOI: `10.1103/PhysRevC.88.044918`.

[105] Z. Xu, G. Wang, A. Tang, and H. Z. Huang, "Fourier coefficients of noninterdependent collective motions in heavy-ion collisions," *Phys. Rev. C*, vol. 107, p. L061902, 6 Jun. 2023. DOI: `10.1103/PhysRevC.107.L061902`.

[106] P. Bo żek and I. Wyskiel, "Directed flow in ultrarelativistic heavy-ion collisions," *Phys. Rev. C*, vol. 81, p. 054 902, 5 May 2010. DOI: `10.1103/PhysRevC.81.054902`.

[107] M. Buzzegoli, D. E. Kharzeev, Y.-C. Liu, S. Shi, S. A. Voloshin, and H.-U. Yee, "Shear-induced anomalous transport and charge asymmetry of triangular flow in heavy-ion collisions," *Phys. Rev. C*, vol. 106, p. L051902, 5 Nov. 2022. DOI: `10.1103/PhysRevC.106.L051902`.

[108] B. Alver and G. Roland, "Collision-geometry fluctuations and triangular flow in heavy-ion collisions," *Phys. Rev. C*, vol. 81, p. 054 905, 5 May 2010. DOI: `10.1103/PhysRevC.81.054905`.

[109] B. Zhang, C. M. Ko, B.-A. Li, and Z. Lin, "Multiphase transport model for relativistic nuclear collisions," *Phys. Rev. C*, vol. 61, p. 067 901, 6 May 2000. DOI: `10.1103/PhysRevC.61.067901`.

[110] Z.-W. Lin, C. M. Ko, B.-A. Li, B. Zhang, and S. Pal, "Multiphase transport model for relativistic heavy ion collisions," *Phys. Rev. C*, vol. 72, p. 064 901, 6 Dec. 2005. DOI: `10.1103/PhysRevC.72.064901`.

[111] STAR Collaboration, "Directed flow in au+au collisions at $\sqrt{s_{NN}} = 62.4$ gev," *Phys. Rev. C*, vol. 73, p. 034 903, 3 Mar. 2006. DOI: 10.1103/PhysRevC.73.034903.

[112] ALICE Collaboration, "Directed flow of charged particles at midrapidity relative to the spectator plane in pb-pb collisions at $\sqrt{s_{\text{NN}}} = 2.76$ TeV," *Phys. Rev. Lett.*, vol. 111, p. 232 302, 23 Dec. 2013. DOI: 10.1103/PhysRevLett.111.232302.

[113] A. Behera, M. Nie, and J. Jia, "Longitudinal eccentricity decorrelations in heavy-ion collisions," *Phys. Rev. Res.*, vol. 2, p. 023 362, 2 Jun. 2020. DOI: 10.1103/PhysRevResearch.2.023362.

[114] P. Bo żek, W. Broniowski, and J. Moreira, "Torqued fireballs in relativistic heavy-ion collisions," *Phys. Rev. C*, vol. 83, p. 034 911, 3 Mar. 2011. DOI: 10.1103/PhysRevC.83.034911.

[115] C. Shen and B. Schenke, "Dynamical initial-state model for relativistic heavy-ion collisions," *Phys. Rev. C*, vol. 97, p. 024 907, 2 Feb. 2018. DOI: 10.1103/PhysRevC.97.024907.

[116] L.-G. Pang, G.-Y. Qin, V. Roy, X.-N. Wang, and G.-L. Ma, "Longitudinal decorrelation of anisotropic flows in heavy-ion collisions at the cern large hadron collider," *Phys. Rev. C*, vol. 91, p. 044 904, 4 Apr. 2015. DOI: 10.1103/PhysRevC.91.044904.

[117] B. Schenke and S. Schlichting, "3d glasma initial state for relativistic heavy ion collisions," *Phys. Rev. C*, vol. 94, p. 044 907, 4 Oct. 2016. DOI: 10.1103/PhysRevC.94.044907.

[118] CMS Collaboration, "Evidence for transverse-momentum- and pseudorapidity-dependent event-plane fluctuations in pbpb and $p$Pb collisions," *Phys. Rev. C*, vol. 92, p. 034 911, 3 Sep. 2015. DOI: 10.1103/PhysRevC.92.034911.

[119] ATLAS Collaboration, "Measurement of the azimuthal anisotropy of charged particles produced in $\sqrt{s_{\_\text{nn}}} = 5.02$ *tevpb+pbcollisionswiththeatlasdetector*,"

*The European Physical Journal C*, vol. 78, no. 12, p. 997, Dec. 2018. DOI: 10.1140/epjc/s10052-018-6468-7.

[120] ATLAS Collaboration, "Longitudinal flow decorrelations in Xe + Xe collisions at $\sqrt{s_{NN}} = 5.44$ TeV with the atlas detector," *Phys. Rev. Lett.*, vol. 126, p. 122301, 12 Mar. 2021. DOI: 10.1103/PhysRevLett.126.122301.

[121] M. Nie, "Energy dependence of longitudinal flow decorrelation from star," *Nuclear Physics A*, vol. 1005, p. 121783, 2021, The 28th International Conference on Ultra-relativistic Nucleus-Nucleus Collisions: Quark Matter 2019. DOI: https://doi.org/10.1016/j.nuclphysa.2020.121783.

[122] Z. Xu, X. Wu, C. Sword, G. Wang, S. A. Voloshin, and H. Z. Huang, "Flow-plane decorrelations in heavy-ion collisions with multiple-plane cumulants," *Phys. Rev. C*, vol. 105, p. 024902, 2 Feb. 2022. DOI: 10.1103/PhysRevC.105.024902.

[123] S. A. Voloshin, "Testing the chiral magnetic effect with central $U + U$ collisions," *Phys. Rev. Lett.*, vol. 105, p. 172301, 17 Oct. 2010. DOI: 10.1103/PhysRevLett.105.172301.

[124] V. V. SKOKOV, A. Y. ILLARIONOV, and V. D. TONEEV, "Estimate of the magnetic field strength in heavy-ion collisions," *International Journal of Modern Physics A*, vol. 24, no. 31, pp. 5925–5932, 2009. DOI: 10.1142/S0217751X09047570.

[125] B. Schenke, C. Shen, and P. Tribedy, "Multiparticle and charge-dependent azimuthal correlations in heavy-ion collisions at the relativistic heavy-ion collider," *Phys. Rev. C*, vol. 99, p. 044908, 4 Apr. 2019. DOI: 10.1103/PhysRevC.99.044908.

[126] Y. Feng, Y. Lin, J. Zhao, and F. Wang, "Revisit the chiral magnetic effect expectation in isobaric collisions at the relativistic heavy ion collider," *Physics Letters B*, vol. 820, p. 136549, 2021. DOI: https://doi.org/10.1016/j.physletb.2021.136549.

[127] F. Wen, J. Bryon, L. Wen, and G. Wang, "Event-shape-engineering study of charge separation in heavy-ion collisions*," *Chinese Physics C*, vol. 42, no. 1, p. 014 001, Jan. 2018. DOI: 10.1088/1674-1137/42/1/014001.

[128] M. Gyulassy and X.-N. Wang, "Hijing 1.0: A monte carlo program for parton and particle production in high energy hadronic and nuclear collisions," *Computer Physics Communications*, vol. 83, no. 2, pp. 307–331, 1994. DOI: https://doi.org/10.1016/0010-4655(94)90057-4.

[129] X.-N. Wang and M. Gyulassy, "Hijing: A monte carlo model for multiple jet production in pp, pA, and AA collisions," *Phys. Rev. D*, vol. 44, pp. 3501–3516, 11 Dec. 1991. DOI: 10.1103/PhysRevD.44.3501.

[130] R. L. Ray and R. S. Longacre, *Mevsim: A monte carlo event generator for star*, 2000. arXiv: nucl-ex/0008009 (nucl-ex).

[131] S. Bass, M. Belkacem, M. Bleicher, *et al.*, "Microscopic models for ultrarelativistic heavy ion collisions," *Progress in Particle and Nuclear Physics*, vol. 41, pp. 255–369, 1998. DOI: https://doi.org/10.1016/S0146-6410(98)00058-1.

[132] S. Choudhury, G. Wang, W. He, Y. Hu, and H. Z. Huang, "Background evaluations for the chiral magnetic effect with normalized correlators using a multiphase transport model," *The European Physical Journal C*, vol. 80, no. 5, p. 383, May 2020. DOI: 10.1140/epjc/s10052-020-7928-4.

[133] R. Milton, G. Wang, M. Sergeeva, S. Shi, J. Liao, and H. Z. Huang, "Utilization of event shape in search of the chiral magnetic effect in heavy-ion collisions," *Phys. Rev. C*, vol. 104, p. 064 906, 6 Dec. 2021. DOI: 10.1103/PhysRevC.104.064906.

[134] STAR Collaboration EPD Group, "Optimizing ep[1] resolution in au27au: From ring-dependent weights to eta-dependent weights,"

[135] J. Orear, *Notes on statistics for physicists, revised*. 1982.

[136]  R. Barlow, "Systematic errors: Facts and fictions," in *Conference on Advanced Statistical Techniques in Particle Physics*, Jul. 2002, pp. 134–144. arXiv: hep-ex/0207026.

[137]  K. Ikeda, D. E. Kharzeev, and Y. Kikuchi, "Real-time dynamics of chern-simons fluctuations near a critical point," *Phys. Rev. D*, vol. 103, p. L071502, 7 Apr. 2021. DOI: 10.1103/PhysRevD.103.L071502.